CASE STUDIES IN BIO-THERMAL MANAGEMENT

A DISSERTATION SUBMITTED TO THE FACULTY OF THE GRADUATE SCHOOL OF THE UNIVERSITY OF MINNESOTA
BY

Ryan D. Lovik

IN PARTIAL FULFILLMENT OF THE REQUIREMENTS
FOR THE DEGREE OF DOCTOR OF PHILOSOPHY

Advisor: Eph Sparrow

December 2011

Abstract:

The human body is an engineered system that utilizes an extensive range of interconnected processes to perform tasks. One category of processes relevant to mechanical engineering is thermal science, which includes both heat transfer and fluid flow. There are a great many organs and interconnecting vessels where such processes occur. Here, a selected group of thermal/fluid processes are set forth and subjected to synergistic analysis by numerical simulation and experimentation.

In this thesis, two case studies are described. One of these involves the heat transfer and fluid flow in association with the removal of plaque from partially blocked arteries. This work necessarily involves the assessment of the temperature rise created by the frictional interaction of the plaque-removal tool and the surface of the plaque material. This process takes place in the presence of flowing blood. The work involved *in vitro* and *in vivo* experiments, the latter with respect to a cadaver. The experimentation also involves means for determining the geometric configurations of arteries before and after plaque removal. The geometric configuration of the artery is of importance due to its effects on the flow of blood through the vessel.

The experimental findings were post-processed and subsequently employed as input information to appropriate numerical simulation models. In the case of heat transfer, a bioheat model was employed to evaluate local temperatures in human tissue. In turn, the local-temperature information was employed to evaluate a thermal tissue injury model. The outcome of that evaluation indicated that temperatures produced by a plaque-removal device would not create tissue necrosis.

The efficacy of plaque removal as a means for ameliorating cardiovascular insufficiency was investigated by means of numerical simulation. The geometric configurations of both a highly stenosed blood vessel and subsequently debulked vessel were determined by means of intravenous ultrasound (IVUS) imaging. These images were reconstituted to create solid models which were subsequently utilized as the basis of numerical simulation. The simulation took account of heart-induced pressure pulsations which were

employed as input information to the time-dependent, three-dimensional Navier-Stokes equations. The ratio of the volumetric rates of blood flow passing through the originally stenosed vessel and the subsequently debulked vessel enabled the formulation of a metric to describe the efficacy of the plaque removal therapy. For the posterior tibial artery, an increase of 2.5 fold in the volumetric flow rate was discovered.

The second case study investigates the thermal effects of the presence of rechargeable implants in the body. It is well established that implants may be sources of heat generation. In the situation to be considered here, the implant does not contain a long-lived internal battery to power its functional activities. Rather, the needed power is provided by means of a transformer whose primary (antenna) is situated externally. The secondary of the transformer is contained within the implant. Both the antenna and the implant generate heat. Both of these heat sources may increase the tissue temperature in the subcutaneous zone and may also increase the temperature in the deeper tissue.

To determine the magnitude of the rate of heat generation by these heat sources, a unique experimental facility was created and implemented. The facility was designed to accommodate antennas and implants of varying geometrical characteristics. A calorimetric method was employed as the means for the determination of the magnitude of the energy transferred from the heat generating devices to their respective environments. Experiments were performed for both the case in which the axes of the implant and the antenna are collinear and for the case in which the axes are misaligned. The criticality of the alignment issue stems from the fact that patients, rather than medical professionals, are required to perform the alignment task. It was found that alignment is, in fact, a major factor with regard to the rates of heat generation and the concomitant temperature elevation of the tissue neighboring these devices.

Attention was focused on neuromodulation implants and their related antennas. For the study, the leading therapeutic neuromodulation devices were employed. For each of these, independent evaluations of heat generation rates were performed. The obtained information provided critical inputs to enable a reliable numerical simulation activity to

be performed. The purpose of the simulation was to obtain temporal and spatial variations of temperatures within the relevant tissue beds. The temperature results were then utilized to assess the likelihood of tissue necrosis resulting from excessive temperatures imposed over lengthy durations.

It was found that there were substantial differences in the outcomes of the various neuromodulation devices. In particular, issues of safety were discovered for at least two of the evaluated devices. It was also found that misalignment aggravated safety issues which were of marginal concern when the implant and its antenna were perfectly aligned.

Table of Contents

List of Tables:

List of Figures:

Chapter 1:
Overview of the Research

1.0 Introduction

An important facet of human health care is the utilization of thermal management techniques. Another important tool for the management and diagnosis of significant maladies such as cardiovascular insufficiency is fluid flow analysis. In recent years, conventional knife-based surgery has been replaced in many instances by thermal-based approaches. For example, the enlarged prostate occurrence, a common event in the lives of older males, was formerly treated by conventional surgery [1.1-1.3]. However, at present, the problem is more often treated by targeted heating or cooling with the aim of creating cell necrosis [1.4, 1.5]. The necrosed cells are sloughed off and the excess size is thereby diminished. Other examples of thermal therapeutic modes are the use of convective warming or cooling devices to respectively control hypothermia and arrest the effects of trauma.

Blood is the agent that delivers oxygen and nutrients to cells dispersed throughout the human body. It also collects products of metabolism. The quality of blood flow is a major factor in the absence or presence of cardiovascular insufficiency. A major contributor to cardiovascular insufficiency is the formation of plaque in blood vessels, primarily arteries. Plaque linings of arteries constrict the cross-sectional area available for blood flow. There are a number of available approaches to deal with plaque-induced cardiovascular insufficiency. These include, among others, angioplasty, stenting, installation of bypass vessels, and atherectomy (debulking). Atherectomy is a means for removing plaque from artery walls.

The foregoing discussion sets the stage for the research to be performed in this thesis. There are three broad categories of thermal and fluid-flow management that will be explored in the forthcoming chapters. They include:

A. Thermal issues connected with the removal of plaque from blocked (stenosed) arteries
B. Enhancement of blood flow created by debulking
C. Thermal heating of implanted therapeutic devices

1.1 Description of the Research

1.1.1 Part A:

As was noted in the foregoing, there are several approaches to removing plaque from blood vessels. Although it might be supposed that angioplasty (an inflated balloon that is routinely used to open blocked arteries) would remove the blockage, in actuality it merely displaces the plaque without removing it [1.6, 1.7]. Once the blood vessel has been opened, a spring-like insert (stent) is commonly introduced to maintain the open status [1.8-1.10]. In current practice, the most effective means of plaque removal is a procedure called atherectomy [1.11-1.15]. In essence, atherectomy is accomplished either by a scraping action or a sanding action.

There is a number of atherectomy devices available for clinical use, and a representative sample of these is displayed in Figure 1.1. At present, these therapeutic devices are

(a) (b) (c)

Figure 1.1: (a) Photograph of Cardiovascular Systems Inc. Diamondback 360˚ orbital atherectomy device. (b) Photograph of Boston Scientific Rotablator rotational atherectomy device. (c) Cartoon of FoxHollow Technologies Inc. SilverHawk longitudinal atherectomy device showing scraping of plaque from the inner wall of an artery.

employed to debulk peripheral arteries, the arteries of the legs and arms; for example, the posterior tibial artery. When these arteries become clogged with plaque, the condition is referred to as peripheral arterial disease (PAD) (Figure 1.2).

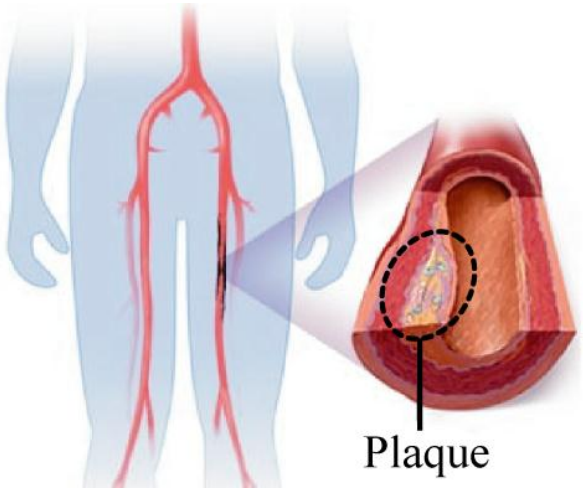

Figure 1.2: Cardiovascular circulatory system of a person with peripheral arterial disease.

The implementation of atherectomy procedures is necessarily invasive. In the case of the sanding approach, a catheter is threaded through the vasculature to the location of plaque to be removed. Although it may appear that the devices pictured in Figure 1.1(a) and (b) are more or less identical, there is a fundamental difference. In the case of the Diamondback 360° (Figure 1.1(a)), the rotation is accompanied by an orbital precession, due to the asymmetric mounting of the Diamondback 360° sanding crown. The orbital motion is not present for the Rotablator (Figure 1.1(b)).

Specific attention is to be given to the Diamondback 360° device (Figure 1.1(a)). The device has a long flexible rotating shaft which is threaded through its catheter. The distal end of the shaft extends beyond the catheter and is positioned in the specific region of the vessel with the plaque to be removed [1.16, 1.17]. This distal end is fitted with a raised crown whose external surface consists of a diamond abrasive. With the axis of the crown being eccentric to the axis of the shaft, the rotation gives rise to an orbital action which drives the sanding surface into contact with the plaque. This orbital-rotational motion is supplemented by a longitudinal traversing that is controlled by a surgeon. The

combination of these motions has proven to be an effective means of driving the sanding head against a region of plaque to be removed.

In practice, the rotational speed of the orbital atherectomy tool is very high, on the order of 100,000 rpm. At such speeds, the *frictional* interaction between the diamond abrasive and the plaque gives rise to a *heating* effect [1.18]. Such heating effects are encountered in numerous engineering applications. In the present instance, the ramifications of the heating may be severe if the heating-based temperature rises are sufficiently great as to cause *cell necrosis*. The issue of necrosis not only depends on the temperature level achieved, but also on the duration of the elevated temperature.

1.1.2 Part B:

The goal of atherectomy is to remove plaque to enlarge the open area of the cross section of a blood vessel. Increasing the open area of a blood vessel allows an increased amount of blood to flow through the vessel to the downstream tissues. Thus, it is relevant to analyze the blood flow in a vessel both before and after atherectomy. In this regard, the patient-specific geometry of a plaque-lined blood vessel was determined and a similar determination was performed for the vessel's after-atherectomy state. This information was obtained by taking two-dimensional ultrasound slices at many locations along the length of the artery of interest. These two-dimensional images were then reassembled to create the actual bore (lumen) of the blood vessel for both the pre- and post- deplaqued vessel. This provided the geometry for fluid-flow simulations to analyze the blood flow through vessels in both the pre- and post- deplaqued status.

1.1.3 Part C:

The Part C investigation was subdivided into two parts. The background for the respective parts is the same, and there is no need to make a distinction between them until it is appropriate. For now, their common background will be described.

Any magnetic field created by the primary of a transformer will create eddy currents in the secondary. It is well known that these eddy currents are capable of creating Ohmic

heating. This effect is commonly encountered whenever MRI diagnostics are performed [1.20-1.30]. It also occurs in connection with implants which are equipped with short-lived batteries [1.31]. The use of short-lived batteries, once shunned for earlier implants, such as pacemakers, has now found favor. A reason for this change of approach is that the use of long-lived batteries requires a periodic replacement with an associated surgical procedure. For example, in the case of pacemakers, the expected battery life is about 5 to 10 years, and that marks the frequency of the replacement surgery [1.32]. Additionally, the long-lived batteries are significantly larger in size. Thus, they require the implant to be of greater volume, which is very undesirable as it takes up more space and is a greater intrusion upon the patient's body. On the other hand, a short-lived battery that is able to be recharged from an external source obviates the need for battery-replacement related surgery and may be of significantly less volume allowing for a much less intrusive implant.

The mode by which the short-lived batteries in the implants of interest are recharged is the mounting of what is, in effect, the primary of a transformer on the skin surface in close proximity to the implant (Figure 1.3). The implant houses the secondary of a transformer, which is energized by the magnetic field of the primary. The secondary current not only creates Ohmic heating, but it also gives rise to a chemically based heat generation associated with battery recharging. Figure 1.3 shows the situation where the axes of the antenna and the implant are perfectly aligned.

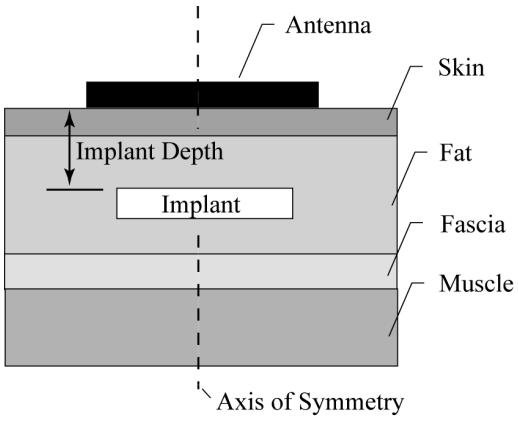

Figure 1.3: A schematic diagram of a skin-surface-mounted antenna (primary of the transformer) and the implant (secondary of the transformer). These components are shown in the context of their placement in relation to human tissue.

The heat source in the implant can, in principle, create temperature elevation in adjacent tissue. The antenna is also a source of heat generation. Therefore, with the presence of these two heat sources, there is a real possibility of elevated temperatures and tissue damage. The elevated temperatures can, in principle, give rise to tissue necrosis. There is, therefore, a significant issue of patient safety that needs to be addressed.

This issue of importance was investigated by a synergistic merging of experimentation and numerical simulation. The goal of the experimentation was to measure the heat generated by each component of the device. This experimentation was performed by means of the calorimetric method (Figure 1.4). This method is based on the absorption of thermal energy by a medium that surrounds the heat source, which in this case is either the implant or the primary of the transformer. In view of its high heat capacity, deionized water was selected as the calorimetric media. This attractive aspect of water provides it with the capability for absorbing a significant amount of heat with only a moderate temperature rise, thereby minimizing the possibility of natural convection. In addition, the output of the heat source may be almost completely absorbed by the water. This, along with the use of an insulating material for the calorimeter housing, minimizes concern about heat penetrating the vessel that contains the calorimetric fluid.

At this point, it is appropriate to describe the two subparts of Part C, and Figures 1.4(a) and 1.4(b) have been prepared and are presented in the following.

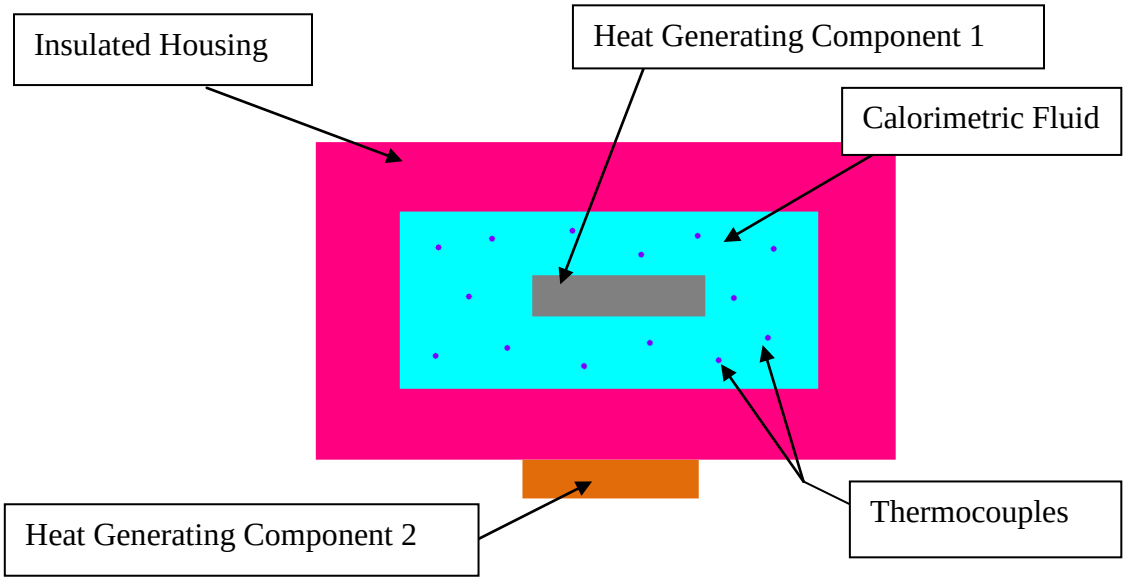

Figure 1.4(a): Schematic diagram showing the experimental setup for measuring the magnitude of the heat generated by either the implant or the primary of the transformer. The axes of the heat generating components are aligned for this case.

In clinical practice, it has been demonstrated that precise alignment of the axes is unlikely. The misaligned situation is illustrated in Figure 1.4(b).

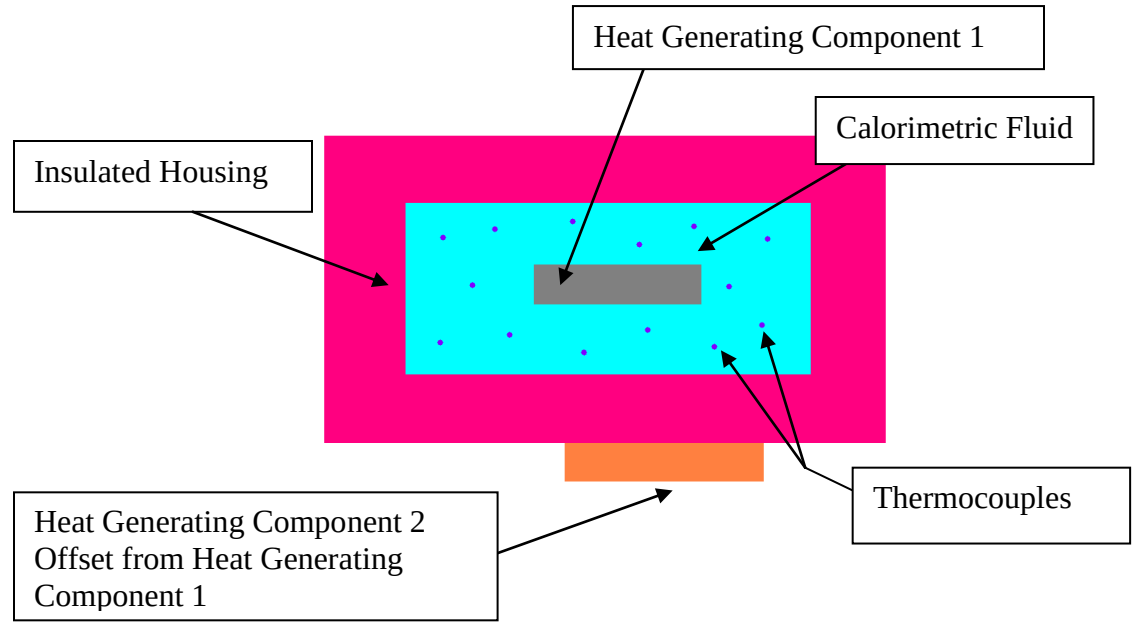

Figure 1.4(b): Schematic diagram showing the experimental setup for the case in which the axes of the heat generating components are misaligned.

By post-processing the temperature measurements, the rate of heat generation of the device components can be obtained. The next step is to create a mathematical model of the heat transfer processes in the tissue that surrounds the implant. The relevant processes are heat conduction, blood perfusion, and metabolic heat generation. In addition, cognizance has to be taken of the heat generation at the surface of the skin due to the presence of the primary of the transformer. There are numerous models in the literature that purport to describe heat transfer in human tissue [1.33-1.40]. These models are characterized by varying degrees of complexity. The first and simplest bioheat model is the Pennes model [1.33]. In subsequent years, numerous criticisms have been leveled at the Pennes model, and a number of processes, not considered by Pennes, have been incorporated into Pennes' original bioheat equation.

The assessment of tissue damage due to the presence of both the magnetic field source and the implant was a major undertaking, but it was a necessary activity to demonstrate the safety of such a therapeutic delivery configuration.

References Chapter 1:

[1.1] M. Cooperberg, J. Broering, P. Carroll, Time trends and local variation in primary treatment of localized prostate cancer, Journal of Clincal Oncology 28 (2010) 1117-1123.

[1.2] J. Wei, R. Dunn, H. Sandler, P. McLaughlin, J. Montie, M. Litwin, L. Nyquist, M. Sanda, Comprehensive Comparison of Health-Related Quality of Life After Contemporary Therapies for Localized Prostate Cancer, Journal of Clinical Oncology 20 (2002) 557-566.

[1.3] F. Burks, R. Santucci, Complicated urethroplasty: a guide for surgeons, Nature Reviews Urology 2010.

[1.4] A. Barqawi, E. Crawford, The current use and future trends of focal surgical therapy in the management of localized prostate cancer, Cancer Journal, 13 (2007) 313-317.

[1.5] R. Habash, R. Bansal, D. Krewski, H. Alhafid, Thermal therapy, Part III: Ablation techniques, Critical Reviews in Biomedical Engineering, 35 (2007) 37-121.

[1.6] S. Park, K. Kim, I. Oh, D. Shin, K. Park, M. Seo, J. Chung, K. Park, H. Lee, H. Kang, B. Koo, T. Youn, H. Kim, Comparison of plain balloon and cutting balloon angioplasty for the treatment of restenosis with drug-eluting stents vs bare metal stents, Circulation Journal 74 (2010) 1837-1845.

[1.7] L. Mauri, R. Bonan, B. Weiner, V. Legrand, J. Bassand, J. Popma, P. Niemyski, R. Kuntz, Cutting balloon angioplasty for the prevention of restenosis: Results of the Cutting Balloon Global Randomized Trial, American Journal of Cardiology, 90 (2002) 1079-1083.

[1.8] U. Baber, A. Kini, S. Sharma, Stenting of complex lesions: An overview, Nature Reviews Cardiology, 7 (2010) 485-496.

[1.9] J. Moses, M. Leon, J. Popma, P. Fitzgerald, D. Holmes, C. O'Shaughnessy, R. Caputo, R. Kuntz, Sirolimus-eluting stents versus standard stents in patients with stenosis in a native coronary artery, New England Journal of Medicine, 349 (2003) 1315-1323.

[1.10] D. Baldwin, J. Abbott, J. Trost, H. Vlachos, F. Selzer, R. Glaser, R. Wilensky, J. Slater, S. Doucet, S. Naidu, H. Aronow, D. Williams, Comparison of Drug-Eluting and Bare Metal Stents for Saphenous Vein Graft Lesions (from the National Heart, Lung, and Blood Institute Dynamic Registry), American Journal of Cardiology, 51 (2008) B23-B98.

[1.11] M. Adamian, A. Colombo, C. Briguori, T. Nishida, F. Marsico, C. Di Mario, R. Albiero, J. Moses, Cutting balloon angioplasty for the treatment of in-stent restenosis: A matched comparison with rotational atherectomy, additional stent implantation and balloon angioplasty, Journal of the American College of Cardiology, 38 (2001) 672-679.

[1.12] B. Vaquerizo, A. Serra, F. Miranda, J. Triano, G. Sierra, G. Delgado, A. Puentes, S. Mojal, J. Brugera, Aggressive plaque modification with rotational atherectomy and/or cutting balloon before drug-eluting stent implantation for the treatment of calcified coronary lesions, Journal of Interventional Cardiology 23 (2010) 240-248.

[1.13] I. Moussa, C. Di Mario, J. Moses, B. Reimers, L. Di Francesco, G. Martini, J. Tobis, A. Colombo, Coronary stenting after rotational atherectomy in calcified and complex lesions: Angiographic and clinical follow-up results, Circulation, 96 (1997) 128-136.
[1.14] R. Regine, O. Catalano, M. De Siero, G. Di Costanzo, A. Ragozzino, Endovascular treatment of femoropopliteal stenoses/occlusions with a SilverHawk directional atherectomy device: immediate results and 12-month follow-up, Radiologia Medica (in press).
[1.15] G. Shrikhande, J. McKinsey, Use and Abuse of Atherectomy: Where Should it be Used?, Seminars in Vascular Surgery, 21 (2008) 204-209.
[1.16] Y. Fu, H. Liu, W. Huang, S. Wang, Z. Liang, Steerable catheters in minimally invasive vascular surgery, International Journal of Medical Robotics and Computer Assisted Surgery, 5 (2009) 381-391.
[1.17] S. Greenberg, G. Murphy, J. Vender, Current use of the pulmonary artery catheter, Current Opinion in Critical Care, 15 (2009) 249-253.
[1.18] A. Gehani, M. Rees, Can rotational atherectomy cause thermal tissue damage? A study of the potential heating and thermal tissue effects of a rotational atherectomy device, CardioVascular and Interventional Radiology, 21 (1998) 481-486.
[1.19] R. Heuser, Treatment of lower extremity vascular disease: The Diamondback 360°™ Orbital Atherectomy System, Expert Review of Medical Devices 5 (2008) 279-286.
[1.20] S. Oh, A. Webb, T. Neuberger, B. Park, C. Collins, Experimental and numerical assessment of MRI-induced temperature change and SAR distributions in phantoms and in vivo, Magnetic Resonance in Medicine 63 (2010) 218-223.
[1.21] G. Calcagnini, M. Triventi, F. Censi, E. Mattei, P. Bartolini, W. Kainz, H. Bassen, In vitro investigation of pacemaker lead heating induced by magnetic resonance imaging: Role of implant geometry, Journal of Magnetic Resonance Imaging 28 (2008) 879-886.
[1.22] S. Mohsin, N. Sheikh, U. Saeed, MRI induced heating of deep brain stimulation leads: effect of the air-tissue interface, Progress in Electromagnetics Research, 83 (2008) 81-91.
[1.23] S. Park, R. Kamondetdacha, J. Nyenhuis, Calculation of MRI-induced heating of an implanted medical lead wire with an electric field transfer function, Journal of Magnetic Resonance Imaging 26 (2007) 1278-1285.
[1.24] K. Yassi, F. Ziane, E. Bardinet, M. Moinard, B. Veyret, J. Chateil, Evaluation of the risk of overheating and displacement of orthodontic devices in magnetic resonance imaging, Journal of Radiology 88 (2007) 263-268.
[1.25] H. Bassen, W. Kainz, G. Mendoza, T. Kellom, MRI-induced heating of selected thin wire metallic implants – laboratory and computational studies – findings and new questions raised, Minimally Invasive Therapy and Allied Technologies, 15 (2006) 76-84.
[1.26] E. Mattei, G. Calcagnini, M. Triventi, F. Censi, P. Bartolini, W. Kainz, H. Bassen, MRI induced heating of pacemaker leads: effect of temperature probe positioning and pacemaker placement on lead tip heating and local SAR, Annual International

Conference of the IEEE Engineering in Medicine and Biology Society 1 (2006) 1889-1892.
[1.27] J. Nyenhuis, P. Sung-Min, R. Kamondetdacha, A. Amjad, F. Shellock, A. Rezai, MRI and implanted medical devices: basic interactions with an emphasis on heating, IEEE Transactions on Device and Materials Reliability, 5 (2005) 467-479.
[1.28] U. Nguyen, J. Brown, I. Chang, J. Krycia, M. Mirotznik, Numerical evaluation of heating of the human head due to magnetic resonance imaging, IEEE Transactions on Biomedical Engineering 51 (2004) 1301-1309.
[1.29] W. Nitz, A. Oppelt, W. Renz, C. Manke, M. Lenhart, J. Link, On the heating of linear conductive structures as guide wires and catheters in interventional MRI, Journal of Magnetic Resonance Imaging 13 (2001) 105-114.
[1.30] M. Dempsey, B. Condon, D. Hadley, Investigation of the factors responsible for burns during MRI, Journal of Magnetic Resonance Imaging 13 (2001) 627-631.
[1.31] M. Nathan, Microbattery technologies for miniaturized implantable medical devices, Current Pharmaceutical Biotechnology 11 (2010) 404-410.
[1.32] T. Saraon, N. Gill-Saraon, A. Miller, R. Sinert, Pacemakers and Implantable Cardioverter Defibrillators. http://emedicine.medscape.com/article/780825-overview (Updated: Aug 30, 2010).
[1.33] H. Pennes, Analysis of tissue and arterial blood temperatures in the resting human forearm, Journal of Applied Physiology 1 (1948) 93-122.
[1.34] H. Arkin, L. Xu, K. Holmes, Recent developments in modeling heat transfer in blood perfused tissues, IEEE Transactions on Biomedical Engineering 41 (1994) 97-107.
[1.35] S. Weinbaum, L. Xu, L. Zhu, A. Ekpene, A New Fundamental Bioheat Equation for Muscle Tissue: Part I—Blood Perfusion Term, Journal of Biomechanical Engineering 119 (1997) 278-288.
[1.36] Y. Xuan, W. Roetzel, Bioheat Equation of the Human Thermal System, Chemical Engineering and Technology 20 (1997) 268-276.
[1.37] C. Charny, Mathematical models of bioheat transfer, Advances in Heat Transfer 22 (1992) 19-155.
[1.38] J. Chato, A view of the history of heat transfer in bioengineering, Advances in Heat Transfer 22 (1992) 1-18.
[1.39] H. Eugene, Pennes' 1948 paper revisited, Journal of Applied Physiology 85 (1998) 35-41.
[1.40] M. Chen, K. Holmes, Microvascular contributions in tissue heat transfer, Annals of the New York Academy of Sciences 335 (1980) 137-150.

Chapter 2:
Thermal Damage of Tissue Due to Debulking by Orbital Atherectomy

2.0 Introduction

The partial or total blockage of arterial blood flow by plaque adhered to the lumen wall is a major factor in cardiovascular disease. The removal of plaque, an operation termed atherectomy or debulking, has been performed successfully by mechanical means in arteries situated in the extremities (e.g., lower leg). Any mechanical means of debulking necessarily involves frictional interaction between the debulking tool and the surface of the plaque. Since friction between surfaces inevitably gives rise to heat generation, it is relevant to address the possible physiological impacts of the temperature rise that normally accompanies heating. To this end, the heat generated by the Diamondback 360° Orbital Atherectomy System (Cardiovascular Systems, Inc., St. Paul, MN), has been investigated to determine if it may cause thermal injury. A photograph of the Diamondback 360° is presented in Figure 2.1.

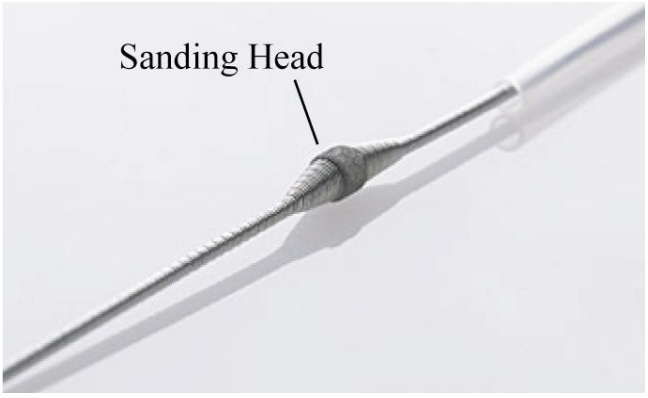

Figure 2.1: Photograph of the Diamondback 360°, an orbital atherectomy device

The issue of heat generation requires a multi-step process. The overall goal of the investigation was to gain an understanding of the sources of the heat generated by the

device as well as its impact with regard to cell death (necrosis). The first step was to make use of a surrogate model of the artery in order to determine the following information:

(a) Identification of the sources of heat generated by the device
(b) Quantify the strength of the heat sources
(c) Quantify the spatial and temporal variation of the bulk temperature of the coolant fluid

The experimental part of this work was not carried out using living human subjects. Rather, surrogates were used for the experiments. For the surrogate experiments, a well-equipped and controlled environment was used. The first surrogate consisted of thick-walled graphite tubes, while the next step was to perform experiments in cadaver subjects. In the latter experiments, the Diamondback 360° device operated on arterial plaque, and measurements of the temperature at the outer surface of the artery being operated upon were made during the debulking process. From these measurements, and from information from the graphite-tube experiments, it was possible by means of a numerical simulation model, to predict the timewise and spatial temperature variations across the thickness of the artery and within the surrounding tissue. Subsequently, these calculations were extended to a living-tissue model with the goal of predicting whether or not thermal necrosis would occur.

2.1 Experiments Involving the Graphite Tube

2.1.1 Experimental Set Up and Data Collection Procedure:

To accomplish the first task, gaining an understanding of the heat generated by the Diamondback 360° device, a well-controlled and repeatable environment, which was well equipped with thermal measurement devices, was desired. To attain this well-controlled and repeatable environment, a surrogate to the human body was necessary. For this purpose, extruded graphite tubes were used as the replacement for plaque-lined arteries that would be operated on in practice.

The graphite tubes had an inner and outer diameter of 1.5 mm and 8.3 mm respectively, and a length of 63.5 mm. Figures 2.2 and 2.3 display the experimental set up. At the inlet of the tube was flexible plastic tubing through which a simulated blood flow was delivered to the graphite tube. Also, the atherectomy device ran through the plastic tubing and into the graphite tube to perform the procedure. Additionally, the device's

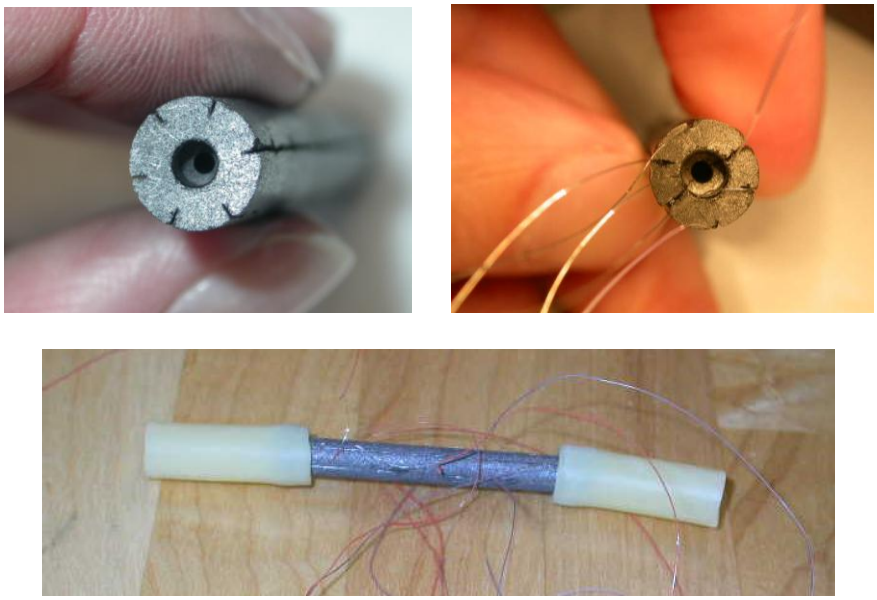

Figure 2.2: These photos show the longitudinal grooves cut into the graphite tubes as well as the placement of thermocouple wires along these grooves and the rubber end caps used for containing the fluid inflow and outflow.

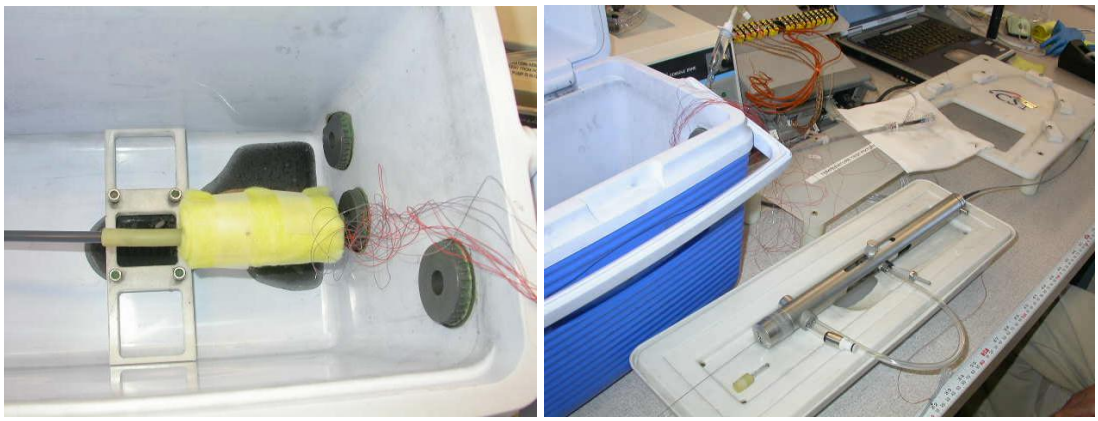

Figure 2.3: These photos present the experimental set up. The photo on the left displays how the graphite tube was wrapped in insulating fiberglass and further placed in an insulating cooler, as seen in the right-hand photo.

coolant flow ran down the device sheath and mixed with the simulated blood at the device sheath exit and entered and flowed through the graphite tube. Fluid leaving the graphite tube was fed into plastic tubing and directed back to the pump for the blood flow. Lastly, the exterior of the graphite tube was surrounded by insulation to minimize the escape of the heat generated by the device.

The experiment was executed by subjecting the graphite tube to sanding by the Diamondback 360° debulking device. The sanding was maintained at a fixed location along the axis of the tube for a time period of 90 seconds.

The temperature of the graphite tube was measured by the means of six thermocouples deployed along the axis of the tube. The thermocouples were seated in longitudinal grooves that had been machined into the outer surface of the tube. Also, thermocouples were located within the fluid at the inlet and outlet of the tube to obtain the temperature of the fluid as it enters and leaves the tube. Additionally, temperature measurements were made at three upstream locations along the wall of the device sheath, which guides and confines the shaft of the Diamondback 360° during rotation.

Many experiments were run at various operating parameters, and the temperature rise of the graphite tube and the temperatures of the fluid at specified locations were measured. In addition to the temperature results, it was desired to gain an improved understanding of the heat loads produced during operation of the Diamondback 360° device and transferred to the graphite tubes to produce the resulting measured temperature rises. To do this, a computational model of the test setup was produced. Then, various thermal loads were applied to the model to simulate the thermal loads exerted by the device during the experimental measurements. Specifically, convection was modeled by using the measured fluid temperature and a suitable value of the convective heat transfer coefficient. Additionally, an appropriate heat flux was used to model the heating due to the sanding of the device. The values used for the convective heat transfer coefficient and the heat flux at the sanding site were varied parametrically until a good match was made between the numerical-simulation temperature results as a function of time and the

experimentally measured temperature results. This approach provided information regarding the heat generated by the device and applied to the graphite tube due to both the heated fluid flow and the sanding action of the device. With regard to the aforementioned heating of the fluid flow, frictional interaction between the rotating shaft of the device and the sheath which serves to guide it creates an elevated temperature which serves to preheat the fluid prior to its arrival at the inlet of the graphite tube.

2.1.2 Results from the Graphite-Tube Experiments:

Two critical observations were made from examination of the temperature measurements. The first is that the temperature level measured in the wall of the graphite tube depended strongly on the temperature level of the flowing fluid. The second is the absence of any significantly elevated temperatures where the sanding of the bore of the tube occurred. These observations provide strong evidence that the primary source of heating is due to the fluid passing through an upstream zone where the rotating shaft and its sheath create a region of elevated temperature. This heated flow is delivered to the inlet of the graphite tube.

Figures 2.4 and 2.5 display timewise temperature variations in the graphite tubes during the operation of the Diamondback 360° device. These results support the conclusion that the preheated fluid is the primary source of heating of the graphite tube. This can be seen in Figure 2.4, which shows results of an experiment in which the device is running with its normal fluid flow. There is a consistent temperature rise of 10°C at all locations along the length of the tube. The absence of a temperature peak at the location of the sanding head indicates that the heat generated by the sanding does not contribute significantly.

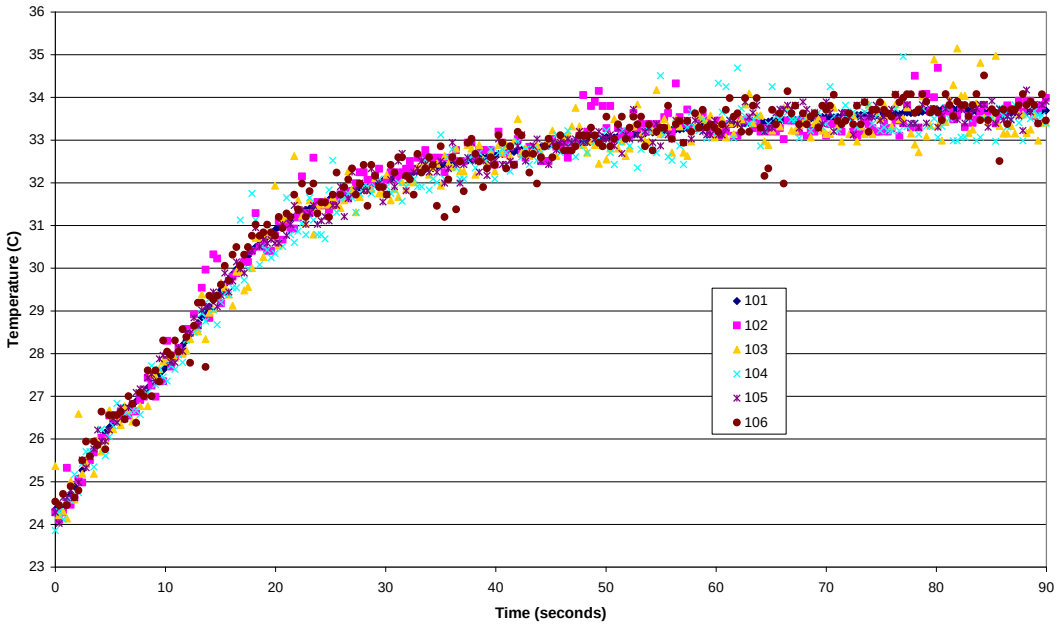

Figure 2.4: Timewise graphite-tube temperature variations in the presence of an enforced fluid flow. The sanding head was situated at a fixed location along the length of the tube, and temperature measurements were made at six axial locations. Location 101 is at the proximal end of the tube, and location 106 is at the distal end.

Figure 2.5 shows results of an experiment in which the device is run without any *enforced* fluid flow. However, it may be conjectured that an *induced* fluid flow may be present. The rotation of the sanding head creates a low-pressure zone due to centrifugal action. It is well-established that fluid will flow between a region of high pressure into a region of lower pressure. In this light, it appears reasonable that fluid will be drawn into the tube inlet from the upstream space. In the upstream space, there is frictional interaction between components of the debulking device, and this frictional interaction is believed to be responsible for preheating the *induced* flow. Consistent with this hypothesis is the fact that the highest measured temperatures are encountered adjacent to the tube inlet and, with increasing downstream distance, the measured temperatures decrease. This decrease can be attributed to heat transfer between the flowing fluid and the tube wall. It can also be noted that the temperatures near the sanding location are not the highest measured temperatures. All told, the temperature rise indicated in Figure 2.5 is less than 2°C at all locations. It is noteworthy that the aforementioned 2°C temperature rise in the absence of enforced fluid flow is considerably less than the 10°C temperature rise which occurred in the presence of enforced fluid flow.

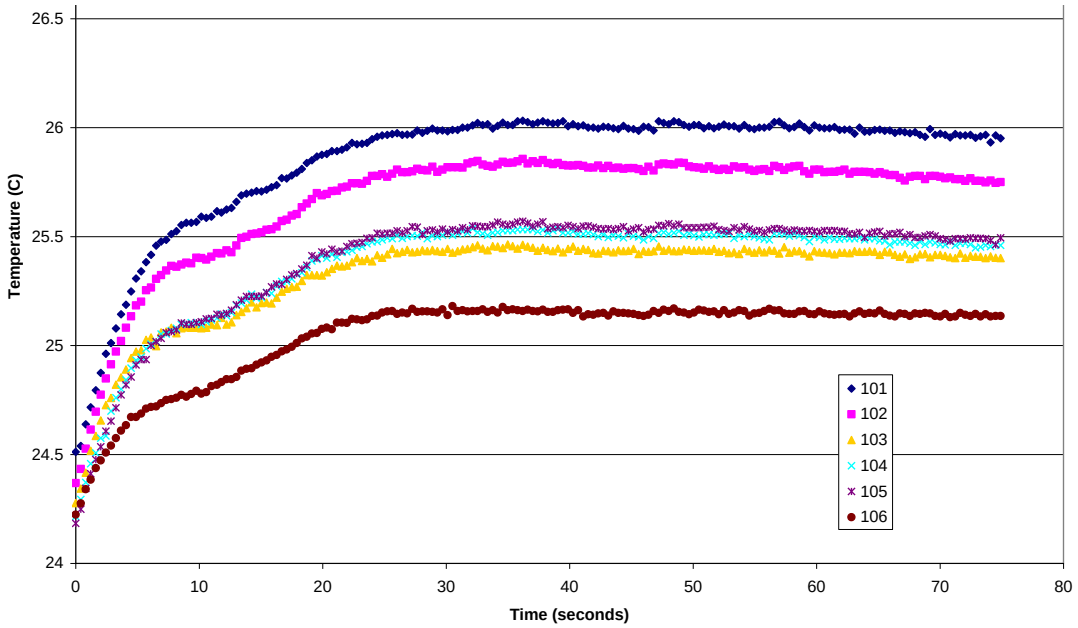

Figure 2.5: Timewise graphite-tube temperature variation in the absence of an enforced fluid flow. The sanding head was set at a fixed axial location of the tube.

The measured temperatures were utilized as input to a numerical simulation model. The goals of the simulation were to obtain quantitative information about the convective heat transfer coefficient at the bore-fluid interface and about the magnitude of heat generation due to the sanding procedure. Parametric values were assigned to both the heat transfer coefficient and the rate of heat generation. The end result of the simulation was the identification of the specific values of these parameters which led to temperatures that matched those of the experiments. Figures 2.6 and 2.7 illustrate the measured temperature rises in the graphite tube and those from the simulation.

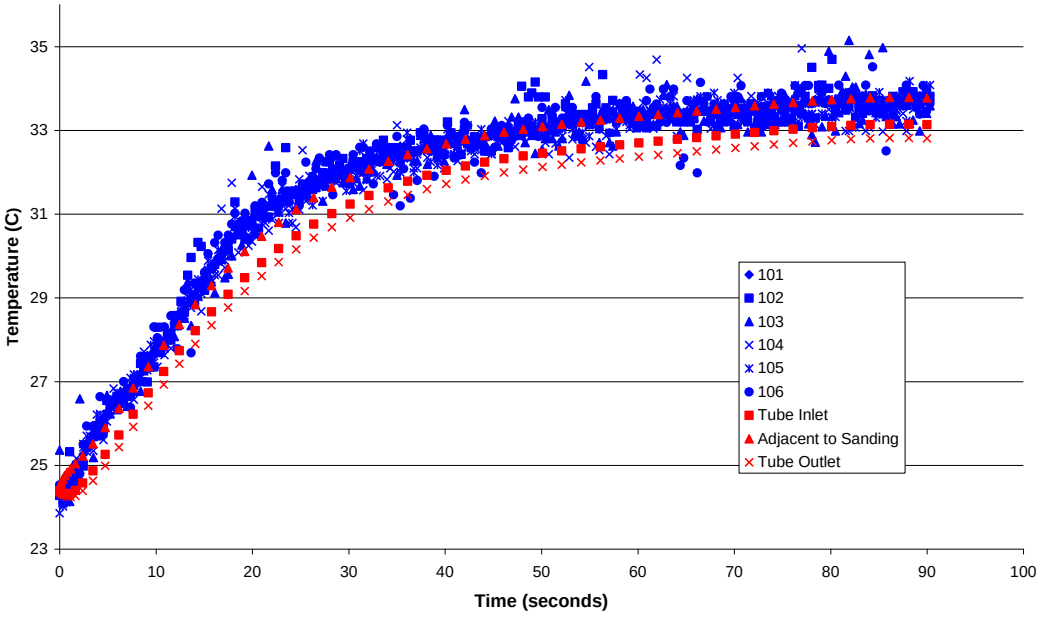

Figure 2.6: Comparison of experimental temperature results with those from the numerical simulation for the case of normal fluid flow. The data points in blue represent the experimental results, and the red points are from the numerical simulation, with a convective heat transfer coefficient of 3000 Btu/hr-ft^2-°F and a heat flux due to sanding of 200000 Btu/hr-ft^2.

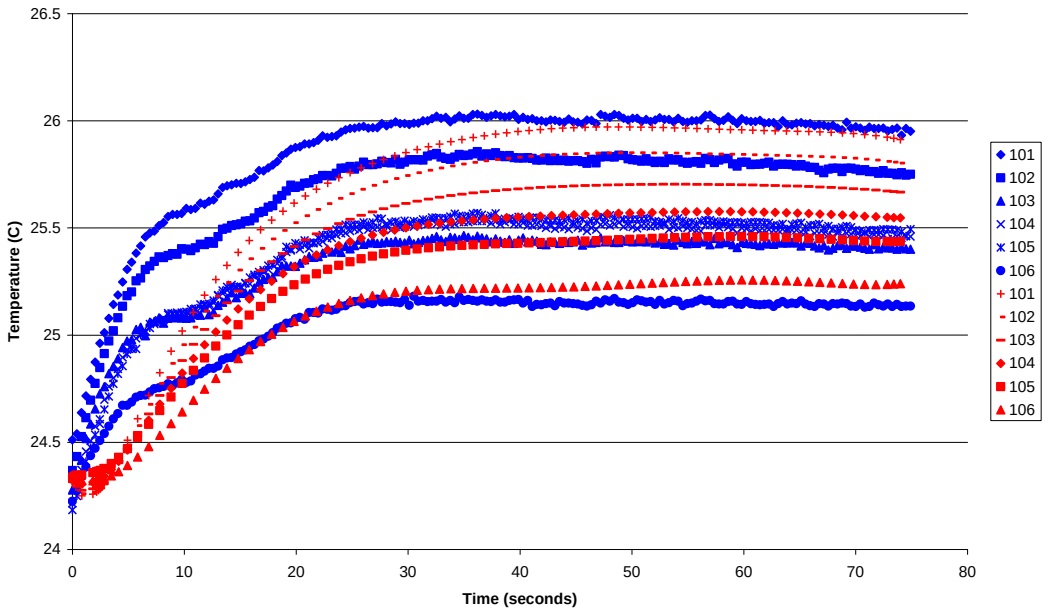

Figure 2.7: Comparison of data collected in the absence of enforced fluid flow with the predictions of a numerical simulation for the case of no enforced fluid flow. The data in blue represent experimental data, and the red points are the simulation results. The simulations were performed with a convective heat transfer coefficient of 4000 Btu/hr-ft^2-°F and a heat flux due to sanding of 30000 Btu/hr-ft^2.

The comparisons displayed in Figures 2.6 and 2.7 indicate that the backed-out values of the convective heat transfer coefficient and the sanding-site heat flux are valid.

2.2 Experiments Involving Cadavers

2.2.1 Experimental Setup and Data Collection Procedure:

To better simulate real life conditions, the device was operated on human cadaver legs with significant amounts of plaque in the arteries (see Figure 2.8). Ten thermocouples were placed along the artery around the region on which the operation was to be performed. The thermocouples were inserted between the outer wall of the artery and the surrounding connective tissue and glued in place (see Figure 2.9). Then, the debulking was initiated, and the temperature results were recorded as a function of time.

These temperatures were used as input to a numerical simulation model of the experiment with the view of the determining the rate of heat transfer produced by the debulking operation. Similar to the procedure described earlier for the graphite tube numerical simulation, the method used for determining the heat transfer rate was iterative.

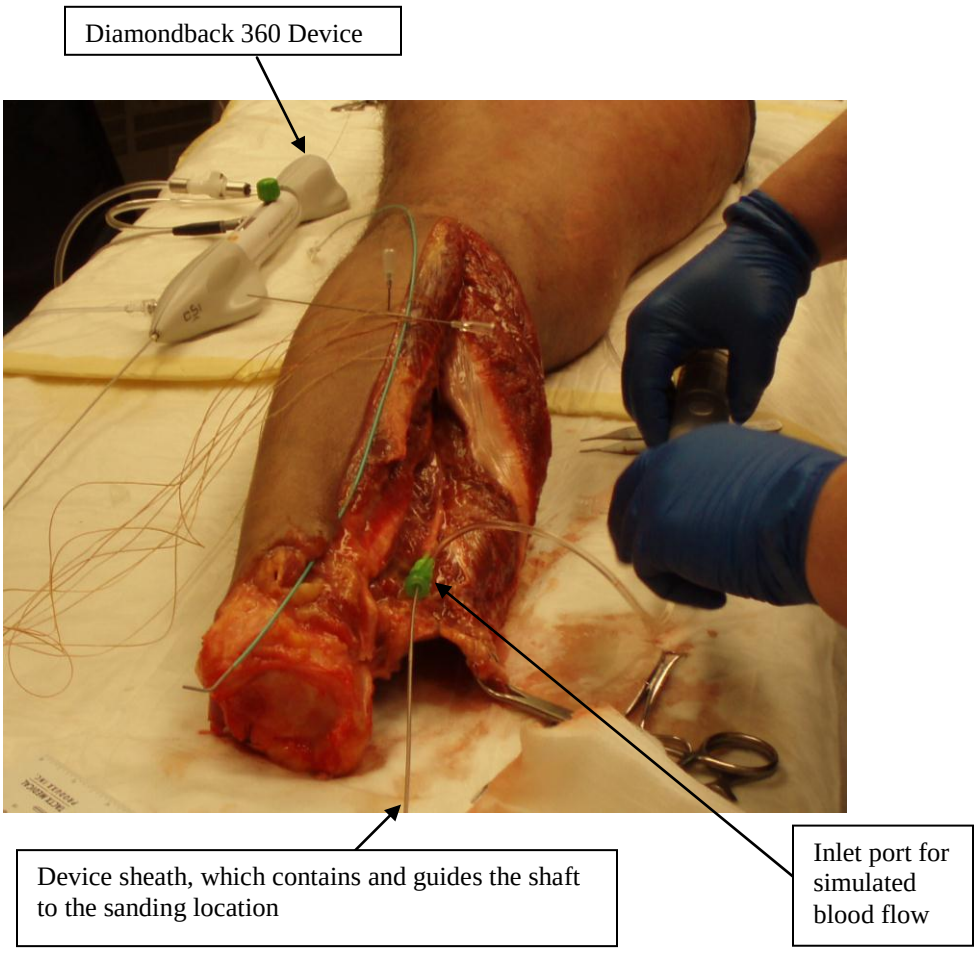

Figure 2.8: Experimental setup of the use of the Diamondback 360° device on a plaque-laden posterior tibial artery of a human cadaver.

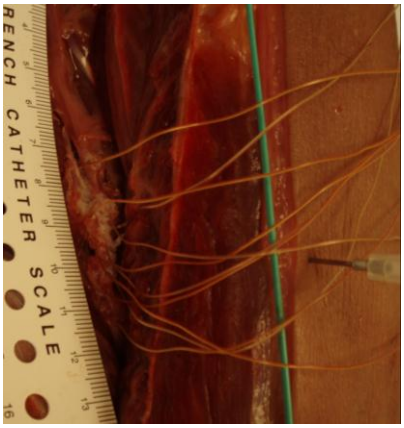

Figure 2.9: Installation of thermocouples placed between the artery outer wall and connective tissue. The thermocouples were affixed in place by gluing.

As noted earlier, operation of the Diamondback 360° heats the region in the neighborhood of the sanding head by frictional interaction between the diamond surface of the head and the plaque. However, the findings of the graphite-tube experiments indicated conclusively that that heating is a secondary matter relative to the heating of the lumen wall that results from the fluid being preheated prior to entering the lumen. In this light, it can be assumed for the purposes of analyses that the rate at which heat transfer enters the lumen wall can be attributed to the upstream heating of the fluid.

The geometric model used for the numerical simulation can be seen in Figure 2.10. The model approximates the artery as being straight and axisymmetric, despite deviations from these idealizations in an actual body. A four-layer model including plaque, artery wall, connective tissue, and surrounding muscle tissue was utilized, and the material properties needed for the thermal solution of the simulation are reported in Table 2.1.

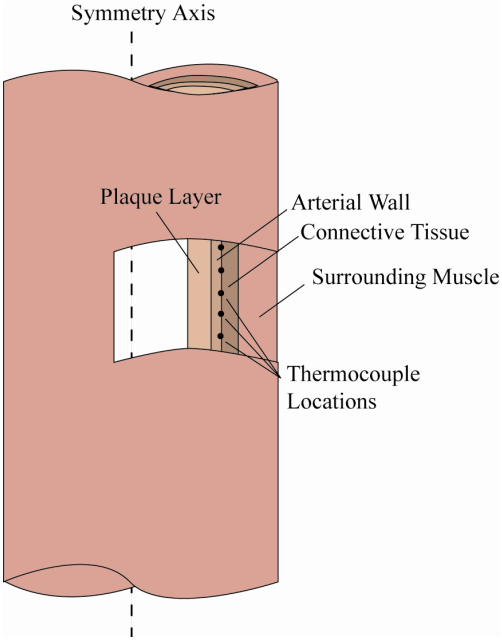

Figure 2.10: Geometric model of the cadaver around the region of device operation.

Table 2.1: Material properties of the modeled materials (source of data noted in brackets where appropriate).

Material	Thermal Conductivity W/(m-K)	Density kg/m^3	Specific Heat J/(kg-K)
Calcified Plaque	0.50 [2.1]	1000	3790
Artery Wall	0.50 [2.1]	1000	3790
Connective Tissue	0.230 [2.2]	1000	3900
Muscle	0.55	1000	3700

The artery inner wall diameter was modeled as 3.3 mm, taken from an IVUS image (intravascular ultrasound) of a cross-section of a cadaver's artery. The artery wall and connective tissue were modeled as 1 mm thick. Additionally, 10 mm of surrounding muscle tissue was modeled and found to provide a large-enough volume such that the effect of the heating on the inner boundary of the model did not produce significant temperature rises. Lastly, the plaque thickness varied along the wall of the cadavers, and this variation was taken into account in the simulation model.

As has been mentioned, all of the heating was modeled as being due to the preheated fluid flow. This left three quantities to be varied parametrically to enable the simulation temperature distributions at the artery outer wall to match the measured temperature profiles. One of these quantities is the convective heat transfer coefficient between the heated fluid flow and the plaque. Its numerical value was taken from the graphite-tube experiments to be 3000 Btu/(hr-ft^2-°F). To investigate the sensitivity of the temperature results to the value of the convective heat transfer coefficient, solutions were also obtained using convective heat transfer coefficients of 2000 and 4000 Btu/(hr-ft^2-°F). Use of these assumed values of the convective heat transfer coefficients that were higher or lower by 1000 Btu/(hr-ft^2-°F) resulted in temperatures in the artery that never differed by more than 0.1°F from the results obtained using a convective heat transfer coefficient of 3000 Btu/(hr-ft^2-°F). Therefore, it was deemed appropriate to use the value for the convective heat transfer coefficient of 3000 Btu/(hr-ft^2-°F). This outcome reduces the number of prescribable quantities to two.

The two remaining quantities are, respectively, the temperature of the preheated fluid as it flows through the region of operation and the thickness of the plaque. First, from the IVUS measurements on cadavers, it was found that the thickness of the plaque varied along the length of the artery wall. The varying plaque thickness in the cadaver is important because it provides a varying thickness of insulation between the heat load supplied by the preheated fluid and the inner surface of the artery wall. The resulting measured temperature variations along the cadaver's artery are due to the plaque's variation in thickness. In the simulation, an iterative variation of the plaque thickness was used to obtain the specific thickness variation that matched the measured temperatures. This approach was focused specifically on the maximum and minimum among the measured temperatures, thereby leading to upper and lower bounds on the plaque thickness. As a consequence, this leaves only one quantity that must be determined to match the given cadaver temperature measurements. This one quantity is the timewise variation of the preheated fluid. This timewise variation is due to the startup transient of the Diamondback 360° device.

The aforementioned timewise temperature variation of the preheated fluid was not measured during the cadaver experiments. However, the shape of the temperature versus time curve can be inferred from the graphite-tube experiments. In that case, the timewise temperature variation of the graphite material followed the timewise variation of the fluid temperature. As the fluid temperature increased during the startup, so also did the temperature of the graphite. With the passage of time, as the fluid temperature achieved a constant equilibrium value, the graphite temperatures reached a steady state.

This reasoning enables the construction of a timewise fluid temperature variation by making use of the measured timewise temperature variation at the artery--connective tissue interface and by adding a temperature offset to account for the temperature drop in the plaque and artery wall. The offset was determined to be consistent with the range of plaque thicknesses described in the penultimate paragraph. In particular, that range was determined to match the simulation results to the measured temperature results at the outer surface of the artery wall.

In the experiments involving the use of cadavers, a peristaltic pump was employed to provide a flow of water through the artery being investigated. This water flow was employed as a surrogate for the blood flow which would normally occur in a living human being. At the start of each data run, both the cadaver section and the water were at room temperature. The duration of a data run was 90 seconds, during which the temperature at the measuring sites was recorded continuously by a data acquisition system. From the collection of data runs, two were chosen as being representative. These runs will be respectively designated the July 13th cadaver and the August 29th cadaver.

Thermal measurements were taken on five separate cadavers. The Diamondback 360˚ device was operated on each cadaver multiple times, with temperature data being recorded. Of the many data runs, two were selected for further study. These are designated according to the days of their execution, July 13th cadaver and August 29th cadaver. The July 13th cadaver data run was selected for study as it is representative of a typical data run with having a maximum temperature rise of 7.6°C (13.7°F). Whereas, for the August 29th cadaver there was an abnormality in the procedure and a maximum temperature rise of 14°C (25.2°F) resulted. It was important to investigate this outlier case to ascertain that the operation of the device will not cause thermal tissue damage for any of the cases.

2.3 Cadaver Experiment Results

For the July 13th data run, the preheated fluid timewise temperature variation was taken fitted by a fourth-order polynomial curve. The fit was based on the highest measured artery outer wall temperature location of the cadaver, with the addition of two offsets (see Figure 2.11). The measured temperature variation was first increased by the addition of a constant temperature. The added temperature offset was increased until it was found that an offset of 6.5°F was enough to allow for a valid range of plaque thickness. In addition, a negative 0.001-hour offset was added to improve the starting temperature of the fluid temperature variation, as it was known that the fluid temperature was at room

temperature at the start of device operation and not at approximately 6.5°F above room temperature.

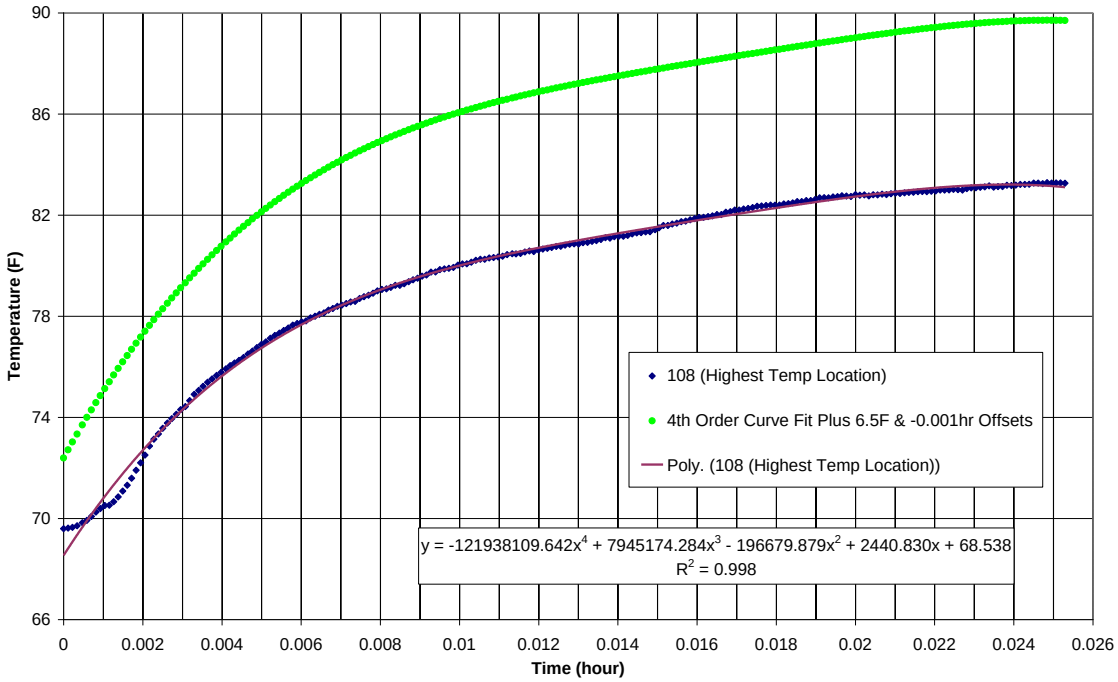

Figure 2.11: Timewise temperature variation at the site (108) of the highest measured temperature at the artery outer wall of the July 13th cadaver. A fourth-order curve was fit to this highest measured temperature location. The green curve is constructed from the fourth-order curve fit plus a 6.5°F offset and a negative 0.001-hour offset.

The green curve of Figure 2.11 was used to represent the timewise variation of the fluid temperature in the numerical simulation along with a convective heat transfer coefficient of 3000 Btu/(hr-ft^2-°F). The only unspecified quantity remainging was the plaque thickness. Thus, it was possible to simulate the July 13th cadaver with only the need to vary the plaque thickness to obtain simulation results that matched the measured temperature results. A plaque thickness ranging from 0.1 to 0.7 mm enabled correlation with the range of measured artery-wall outer temperatures (Figure 2.12).

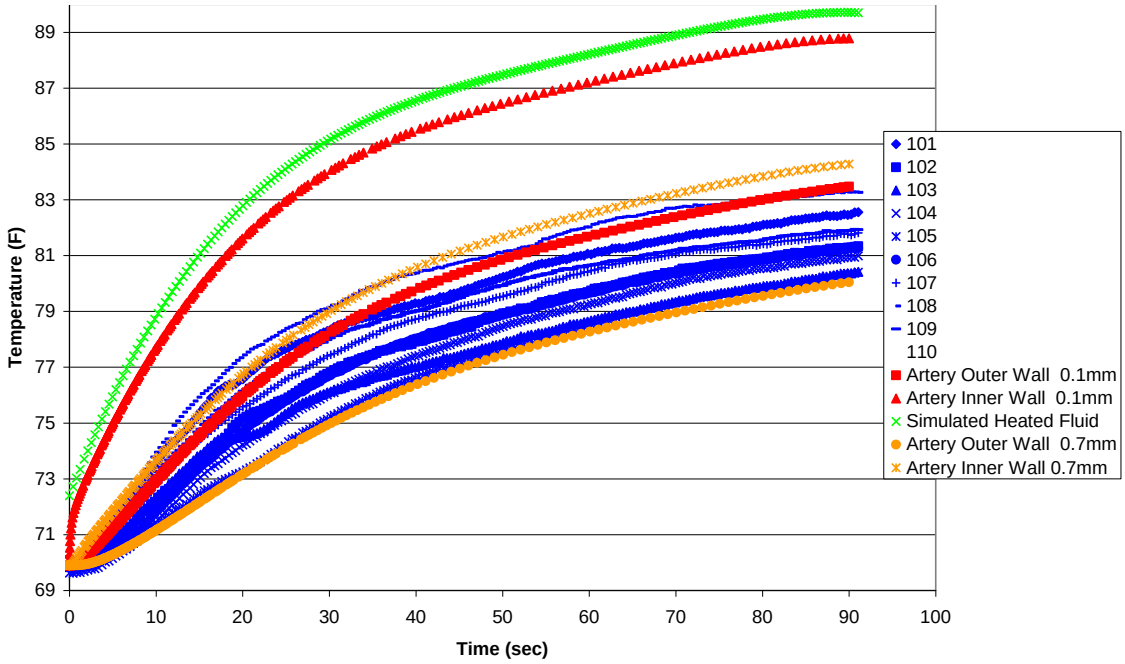

Figure 2.12: Timewise temperature results, with time equal to zero coinciding with the start of Diamondback 360˚ device operation. Data points in blue are those measured along the artery outer wall of the July 13th cadaver (note that measured data point 110 has been disregarded due to irregularities in the temperature over time profile). The green data points show the heated fluid temperature profile used in the simulations. The red data points represent the inner and outer artery wall temperature profiles from the simulation using 0.1 mm plaque thickness, and the orange data points show the inner and outer artery wall temperature profiles for the simulation using 0.7 mm plaque thickness.

Of great interest is the maximum temperature of the tissue in the simulation. This maximum temperature location occurred at the artery inner wall for the minimum plaque thickness case of 0.1 mm. In this case, the artery inner wall reached a value of 88.8°F (31.6°C), which is an 18.9°F (10.5°C) rise above the starting temperature of 69.9°F (21.1°C). Furthermore, this maximum artery inner wall temperature is 5.3°F (2.9°C) greater than the maximum outer wall temperature. This result is significant, as it reveals that even if temperatures measured at the outer wall of the artery report safe levels of temperature rise, it must be considered that the inner wall of the artery (only 1 mm closer to the heat generation) can be 5.3°F (2.9°C) higher in temperature and may not be at a safe temperature level.

Now, turning to the August 29 cadaver, a timewise temperature distribution for the preheated fluid was produced by using a sixth-order curve fit to the temperature measured at the artery outer wall. Then, an added 9°F temperature offset to this curve fit was found to be enough to allow a valid range of plaque thickness (see Figure 2.13 below).

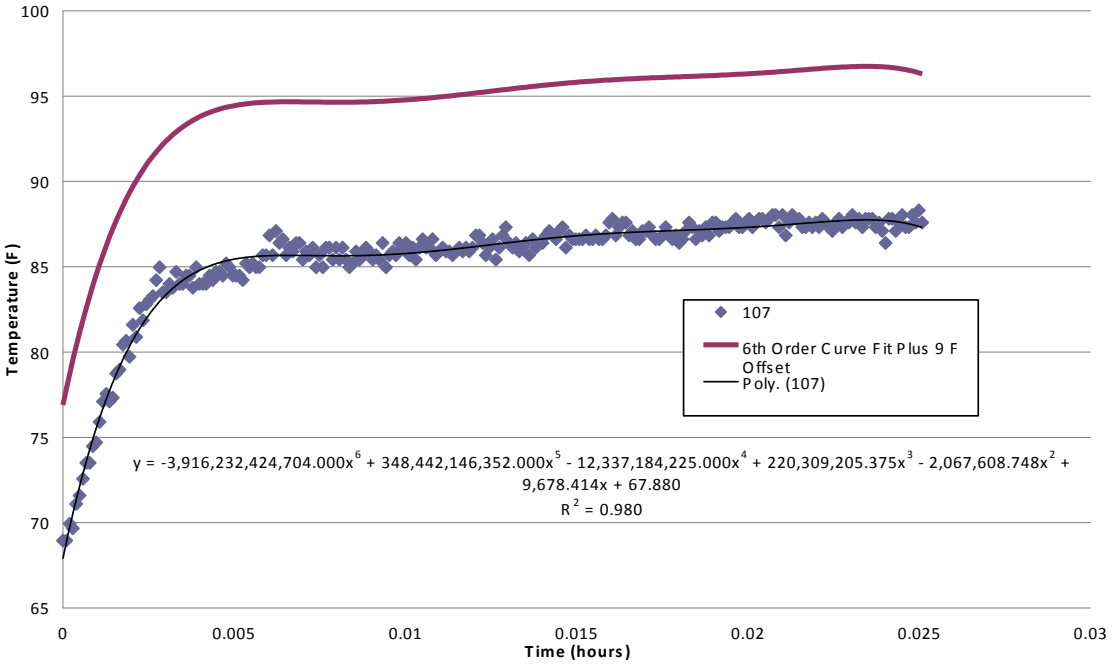

Figure 2.13: Temperature versus time variation of the temperature at location 107 at the artery outer wall of the August 29th cadaver. Also shown is the sixth-order curve fit to these data. The equation of the fit is also indicated. The maroon curve which served as input to the numerical simulation is the sixth-order equation plus a 9°F offset.

With the maroon curve of Figure 2.13 as input along with a given convective heat transfer coefficient, the only variable remaining was the plaque thickness. It was, therefore, possible to simulate the August 29th cadaver with only the need to vary the plaque thickness to obtain simulation results that correlated with the measured results of the August 29th cadaver. Use of a convective heat transfer coefficient of 3000 Btu/(hr-ft^2-°F), led to plaque thickness variations ranging from 0.1 to 0.6 mm to correlate with the range of measured artery wall outer temperatures (Figure 2.14).

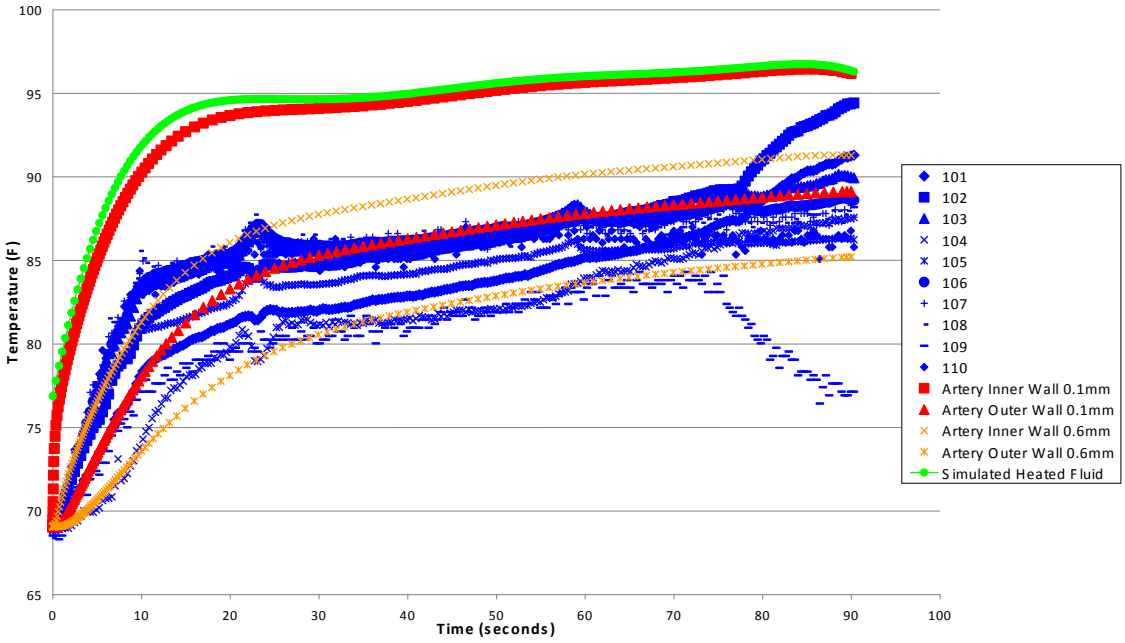

Figure 2.14: Temperature over time graph with time equal to zero coinciding with the start of Diamondback 360˚ device operation. Data points in blue are those measured along the artery outer wall of the August 29th cadaver. The green data points show the heated fluid temperature profile used in the simulations. The red data points show the inner and outer artery wall temperature profiles for the simulation using 0.1 mm plaque thickness and the orange data points show the inner and outer artery wall temperature profiles for the simulation using 0.6 mm plaque thickness.

Again, of great interest is the maximum temperature of the tissue in the simulation. This maximum temperature location occurs, as expected, at the artery inner wall for the minimum plaque thickness case of 0.1 mm. In this case, the artery inner wall reached a value of 96.4°F (35.8°C), which is a 27.4°F (15.2°C) rise above the starting temperature of 69.1°F (20.6°C). Furthermore, this maximum artery inner wall temperature is 7.3°F (4.1°C) greater than the maximum outer wall temperature. This result is of pivotal importance, as it further demonstrates that even if temperatures measured at the outer wall of the artery report safe levels of temperature rise, it must be considered that the inner wall of the artery (only 1 mm closer to the heat generation) can be 7.3°F (4.1°C) higher in temperature and may not be at a safe temperature level.

2.4 Numerical Simulations on Living Human Tissue

With the now-available knowledge of the effective heat load due to the operation of the debulking device, focus was redirected to the numerical simulation of living tissue. The goal of this work was to determine if there should be concern about thermal tissue damage. To model living tissue, the same geometry and material properties were used as in the cadaver model. However, living human bodies have the added capability of regulating the temperature of their tissue to a significant degree. In particular, the body can cool tissue that reaches elevated temperature via blood perfusion acting as a convective heat transfer means. Blood perfusion cools by convection between the approximately core body temperature blood that perfuses through the elevated temperature tissue. Thus, in the adopted model of living tissue heat transfer, a blood perfusion term was included to account for this temperature regulating ability of the human body.

Specifically, the Pennes bioheat equation was used to take account of all of the thermal transfers in tissue, including blood perfusion [2.3]. The blood perfusion term in the Pennes bioheat equation is as follows:

$$\rho_B * c_B * \omega * (T_A - T) \tag{2.1}$$

In this equation, ρ_B is the density of blood (1000 kg/m^3), c_B is the specific heat of blood (4000 J/(kg-°C)), ω describes the rate of blood perfusion, T is the temperature of the tissue at the specific location and moment in time, and T_A represents the temperature of the arterial blood for the perfusion. The value of T_A has been taken to be equal to that of core body temperature, 98.6°F (37°C). The quantity (T_A – T) shows that the magnitude of the heat transfer due to blood perfusion depends on the temperature of the specific tissue. In other words, the more the temperature of the tissue deviates from the body core temperature, the greater will be the magnitude of the heat transfer due to blood perfusion, always acting to return the tissue temperature to the body core temperature.

The parameter ω requires some further discussion. This quantity is equal to the volumetric flow rate of blood passing through a unit volume of tissue. The value of ω depends on the type and location of the given tissue. Moreover, the value of ω for a given tissue type varies from person to person, and even within a given person it varies with time. These factors, combined with the well-established difficulty in measuring ω, have produced a wide range of ω values reported in the literature for a given tissue type. To account for this uncertainty in the value of ω, multiple simulations were run with parametrically varying magnitudes of blood perfusion. The baseline values used for ω were 0.019 s^{-1} [2.4] for the artery wall tissue and 0.00045 s^{-1} [2.5] for the muscle tissue. In recognition of the lower levels of blood perfusion through connective tissue, the worst case of no blood perfusing through the connective tissue was used. Then, to account for the uncertainty of ω, additional simulations were run, one with 1.5 times the baseline blood perfusion, another with 0.5 the baseline, and the worst case of no perfusion by any of the tissue layers considered.

The Pennes bioheat equation that was used for the numerical simulations is

$$\rho c \frac{\partial T}{\partial t} = k \frac{\partial^2 T}{\partial z^2} + \frac{k}{r} \frac{\partial}{\partial r}\left(r \frac{\partial T}{\partial r} \right) + (\rho c)_b \omega (T_a - T) + S \qquad (2.2)$$

The quantities ρ, c, and k represent the density, specific heat, and thermal conductivity of the tissue. Metabolic heat generation is denoted by S. In general, S is smaller than the other terms in Eq. (2.2) and is omitted from the present numerical simulation. Note that an axisymmetric geometrical model was adopted. The independent variables t, r, and z indicate the spatial and temporal coordinates.

The next issue to be considered for living human tissue is that it is not immediately damaged upon reaching moderately elevated temperatures. Thus, the maximum temperature that the tissue attains is not necessarily indicative of thermal injury. Rather, account must be taken of the time during which the elevated temperature acts. In this regard, the operating duration of the device must be accounted for. The Diamondback 360˚ device is normally run for a period of 90 seconds, followed by a 30-second rest period in which the device is no longer rotating and generating heat. During the rest

period, the fluid continues to flow through the device into the artery through the operating region. The Diamondback 360˚ device may be run for as many as six consecutive cycles. Therefore, to consider the total accumulated impact of the heat generated by the device and exerted upon the tissue, the complete six-cycle case was simulated. During the 90 seconds of device operation, the total effective thermal heat load, as derived from the cadaver experiments, was applied to the model, whereas during the 30 seconds of rest, the effect of the flowing fluid was modeled by convective heat transfer with a convective heat transfer coefficient of 3000 Btu/(hr-ft^2-°F) and a fluid bulk temperature of 98.6°F (37.0°C).

The outcome of the numerical simulations yielded the timewise variations of the local temperature. Now, with this information, a tissue thermal injury model [2.6] was used to evaluate the cumulative thermal damage over the operating duration. The thermal injury model used is as follows

$$\text{Cumulative thermal injury} = \Omega = \Sigma \{A * \exp\left(\frac{-E}{R*(T(t)+273)}\right) * \Delta t\} \qquad (2.3)$$

With A = 5.60 * 10^{63} s^{-1}, E = 4.3 * 10^5 J/mole, R = 8.314 J/(mole-°K), t the time in seconds, and T is the temperature of the tissue in degrees Celsius at a given location at time t [2.7]. The summation is extended over the time integral of the debulking operation.

2.5 Thermal Injury Calculations for Diamondback 360˚ Device Operation on Living Humans

First, the effective total heat load derived from the experiments on the July 13th cadaver was applied to the live tissue model with varying levels of blood perfusion. The temperature versus time results for the baseline blood perfusion living tissue model can be seen in Figure 2.15. For this baseline, the maximum temperature attained within the tissue region occurred at the inner wall of the artery at the end of the last device operating period and is equal to 117.3°F (47.4°C). It can be seen from the graph of the results in

Figure 2.15 that the tissue locations nearest the inner wall of the artery have the greatest temperature rise and during the cooling periods return to temperatures below 102°F (39°C). With increasing depth into the tissue, the extent of the temperature rise decreases. Additionally, for the deeper tissue locations, it can be seen that the effect of the cooling periods is felt to a lesser extent; at a depth of 10 mm within the muscle tissue, the temperature does not ever decrease, but continues to gradually rise.

There is little difference between the temperature rise results for the baseline blood perfusion model and for the models based on +/- 50% of the baseline perfusion. Moreover, for the no-blood-perfusion model, the same pattern in the results can be observed as for the baseline. The only difference is that slightly higher temperatures are reached at all locations for the no-perfusion case. For example, the maximum temperature reached is located at the artery inner wall and is equal to 117.7°F (47.6°C), compared with 117.3°F (47.4°C) for the baseline case.

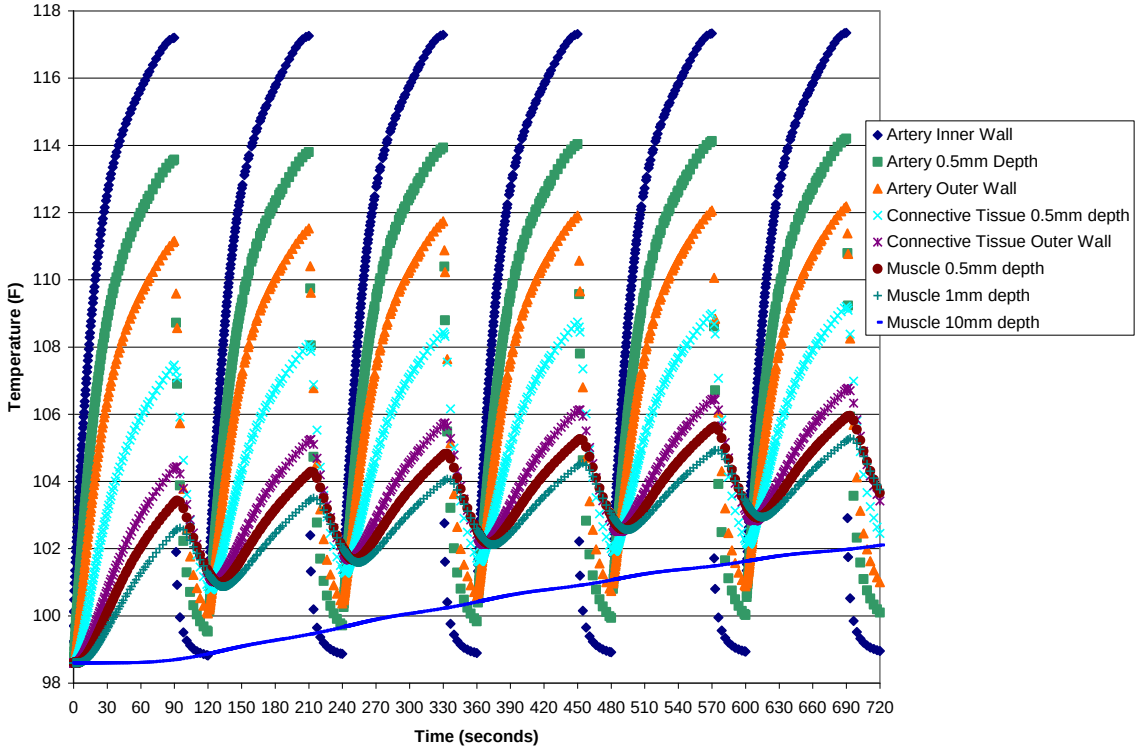

Figure 2.15: Temperature versus time results for various tissue depths for the baseline blood perfusion living tissue model. The thermal load is that of the July 13th cadaver.

The temperature versus time results for the heat load from the July 13 cadaver were used as input to the tissue thermal injury model. The commonly accepted threshold for thermal injury is $\Omega \sim 1$ [2.4, 2.8]. The computed results for Ω can be seen in Table 2.2. As expected, the maximum cumulative thermal injury was imparted to the artery inner wall and is equal to a value of 0.000114 for the baseline blood perfusion model and 0.000123 for the no-blood perfusion model. This outcome indicates that there is no concern for thermal tissue damage due to normal operation of the Diamondback 360˚ device.

Table 2.2: The maximum cumulative thermal injury values (Ω) for the baseline and for no-blood perfusion models for various tissue depths. The thermal load is from the July 13th cadaver experiments.

Location	Baseline Blood Perfusion	No Blood Perfusion
Artery Inner Wall	0.000114	0.000123
Artery Depth 0.5 mm	0.000046	0.000059
Artery Outer Wall	0.000026	0.000035
Connective Tissue Depth 0.5 mm	0.000012	0.000016
Connective Tissue Outer Wall	0.000007	0.000009
Muscle Depth 0.5 mm	0.000006	0.000008
Muscle Depth 1.0 mm	0.000005	0.000007

Next, the total effective thermal load of the Diamondback 360˚ derived from the August 29th cadaver study was applied to the living tissue model. Due to some irregularities in the operation of the device for this cadaver, noticeably higher temperature rises were measured in the cadaver tissue. However, this case is being studied to demonstrate that the increased thermal load due is not enough to cause thermal tissue damage.

The temperature versus time results for the baseline blood perfusion living tissue model for the effective thermal load from the August 29th cadaver can be seen in Figure 2.16. For this baseline blood perfusion living tissue model, the maximum temperature attained within the tissue region, as expected, occurred at the inner wall of the artery and is equal to 125.5°F (51.9°C). This is an increase in maximum temperature attained in the tissue

of 8.2°F (4.6°C) over the maximum temperature attained in the tissue using the effective thermal load from the July 13th cadaver. Like the July 13th cadaver results, the August 29th cadaver results show, as can be seen in Figure 2.16, that the tissue locations nearest the inner wall of the artery have the greatest temperature rises, as well as the greatest decreases in temperature during the device rest periods.

As was found with the previous cadaver effective heat load, there was little difference between the temperature results of the baseline blood perfusion model and the +/- 50% of the baseline blood perfusion models. Moreover, for the no-blood perfusion model, the same pattern in the results can be observed as seen in the baseline blood-perfusion model, with the only difference being that slightly higher temperatures are reached at all locations for the former. For example, the maximum temperature reached for the no blood perfusion model is likewise located at the artery inner wall and is equal to a slightly greater temperature; 125.9°F (52.2°C) versus 125.5°F (51.9°C).

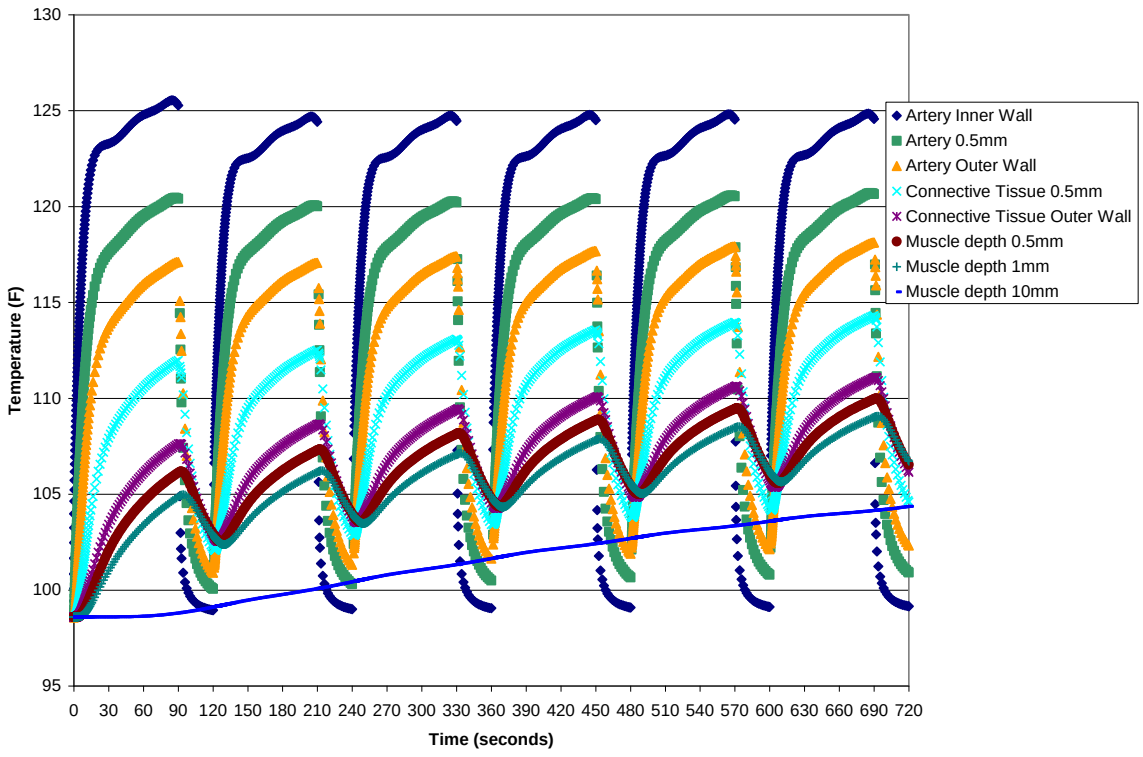

Figure 2.16: Temperature versus time results for various tissue depths for the baseline blood perfusion living tissue model with the thermal load from the August 29th cadaver.

The results for the living tissue model with the August 29th cadaver thermal load were inputted to the tissue thermal injury model. The thermal cumulative injury results (Ω) can be seen in Table 2.3. As a result of the August 29th experiments producing a greater higher effective thermal load, the temperature rises in the tissue were greater than those for the July 13th case. Correspondingly, higher values of the thermal injury metric (Ω) were attained. Again, as expected, the maximum cumulative thermal injury was imparted to the artery inner wall. This maximum cumulative thermal injury is 0.001243 for the baseline blood perfusion model and 0.001394 for the case of no-blood perfusion. This result indicates that despite the greater thermal loads obtained from the August 29th cadaver experiments, there is no concern for thermal tissue damage due to operation of the Diamondback 360˚ device.

Table 2.3: The maximum cumulative thermal injury values (Ω) for the baseline and for no-blood perfusion models for various tissue depths. The thermal load is from the August 29th cadaver experiments.

Location	Baseline Blood Perfusion	No Blood Perfusion
Artery Inner Wall	0.001243	0.001394
Artery Depth 0.5 mm	0.000344	0.000510
Artery Outer Wall	0.000154	0.000242
Connective Tissue Depth 0.5 mm	0.000049	0.000074
Connective Tissue Outer Wall	0.000021	0.000031
Muscle Depth 0.5 mm	0.000016	0.000023
Muscle Depth 1.0 mm	0.000013	0.000019

2.6 Concluding Remarks

The heat generated during operation of the Diamondback 360˚ orbital atherectomy device and subsequently impressed upon the surrounding human tissue upon a patient has been investigated. First, experiments were executed by operating the device upon a well controlled environment, graphite tubes. These experiments revealed that the primary source of heating from the operation of the device is the preheated fluid flow that enters the graphite tube. The cause of the preheating is frictional interaction between upstream parts of the device. This heating is imparted to the fluid flowing past the site of the

frictional interaction. The secondary source of heating is due to the abrading of the inner wall of the tube by the rotation of the debulking device.

Secondly, experiments were performed on cadavers; in which the debulking device device was operated upon the arterial plaque of the cadaver, and the resulting temperature rises in the cadaver's tissue were measured. From these temperature results, the effective heat load due to device operation on the arterial plaque was determined. The heat load information was subsequently used as input to a numerical simulation of living tissue. The resulting temperature rises in the tissue was obtained. The maximum temperature rise was seen to occur at the artery inner wall and to decrease with increasing depth into the tissue. These temperature results were then inputted into a tissue thermal injury model.

The tissue thermal injury results for the living tissue model were obtained for the case of maximum device operating duration (six consecutive cycles of 90 seconds of device operation followed by 30 seconds of device rest). From the use of the cadaver experiment results that yielded the greatest heat generation, the August 29th cadaver, it was found that the maximum cumulative thermal injury was located at the artery inner wall. The thermal injury metric was found to equal 0.001243 at the artery inner wall for the living tissue model including blood perfusion and 0.001394 for no blood perfusion. These values of thermal injury metric are multiple orders of magnitude below the metric that is commonly accepted as the threshold for thermal injury, approximately one. Therefore, these results indicate conclusively that there is no likelihood of thermal damage to tissue due to operation of the Diamondback 360° device for as many as six consecutive cycles of 90 seconds of device operation followed by 30 seconds of rest.

References Chapter 2:

[2.1] J. Valvano, J. Chitsabesan, Thermal Conductivity and Diffusivity of Arterial Wall and Athersclerotic Plaque, Lasers Life Sciences 1 (1987) 219-229.

[2.2] F. Duck, Physical Properties of Tissue. London: Academic Press (1990) 9-42.

[2.3] H. Pennes, Analysis of tissue and arterial blood temperatures in the resting human forearm, *J. Appl. Physiol*. 85 (1948) 5-34.

[2.4] K. Diller, J. Valvano, J. Pearce, Bioheat Transfer. CRC Handbook of Thermal Engineering, Boca Raton: CRC Press, 2000.

[2.5] C. Keele, E. Neil, Applied Physiology, 12th ed., London: Oxford Press, (1971) 62.

[2.6] F. Henriques, A. Moritz, Studies of thermal injury I: the conduction of heat to and through the skin and the temperatures attained therein. A theoretical and experimental investigation, *Am. J. Pathol*, 23 (1947) 531-549.

[2.7] A. Han, J. Pearce, Kinetic Model for Thermal Damage in the Myocardium, In: Advances in Measuring Temperatures in Biomedicine; Thermal Tomography Techniques and Bioheat Transfer Models, New York: ASME, 1990.

[2.8] K. Diller, Modeling of Bioheat Transfer Processes at High and Low Temperatures, Advances in Heat Transfer, Bioengineering Heat Transfer, Boston: Academic Press, 22 (1992) 157-348.

Chapter 3:
Unsteady, three-dimensional fluid mechanic analysis of blood flow in plaque-narrowed and plaque-freed arteries

3.0 Introduction

Fluid mechanic phenomena play a major role in the functioning of virtually all processes that occur in the human body. Most evident among these phenomena is the delivery of oxygen and nutrients to the cells by blood flow and the extraction and transport of wastes by the blood. There is an extensive literature on blood flow in the human body, for instance, [3.1] and [3.2]. The work that is reflected by these references encompasses a wide range of fluid flow models, including steady flow in circular passages in [3.3-3.7]; steady flow in non-circular passages obtained by reconstitution of medical images by [3.8-3.10]; unsteady flows driven by the pressure waveforms due to the beating heart by [3.11-3.16]; and Newtonian and non-Newtonian constitutive models by [3.3, 3.17-3.19]. Issues such as fluid-structural interactions, specifically the interactions between the blood flow and arterial walls, have only recently been considered by [3.20-3.21].

The objective of the present chapter is somewhat different from that of the aforementioned citations. Here, it is proposed to use fluid mechanic modeling to evaluate the efficacy of a critical therapeutic procedure. Atherosclerosis is a common human affliction in which blood vessels become narrowed and even blocked by the accumulation of plaque deposits on internal surfaces. Among the techniques for removal of the plaque formations, the use of mechanical means has found significant application. These means may include: cutting, sanding, or scraping. Typically, these methods remain unevaluated with regard to outcome and, at best, the evaluation of outcomes is highly qualitative.

The work set forth here is to model the blood flow through a plaque-narrowed artery and its counterpart subsequent to removal of plaque by mechanical means. The specific device used here to remove the arterial plaque (to *debulk*) is the Diamondback 360°

Orbital Atherectomy System (Cardiovascular Systems, Inc., St. Paul, MN). The outcome of the application of this device will be conveyed via reconstituted ultrasound images. Those images, when translated into a solid-model format, create realistic geometries for the application of the fluid mechanic model.

The fluid flow model will account for the pulsations created by the cardiac cycle and of the complex geometries of both the pre-treated and post-treated artery. The specific artery in question is the posterior tibial, which is situated in the lower leg. This artery is one of the most susceptible to plaque formation.

The specific results that are sought as the outcomes of the modeling effort are the comparative blood flows in the pre-debulked and debulked arteries when subjected to the same time-dependent driving pressures. Of equal relevance as an outcome to the therapeutic procedure is the shear stress exerted by the pulsating flow on the artery walls. These shear stresses play a major role in the recurrence of the plaque (*restenosis*).

3.1 Creation of the geometrical model

The preliminary work that was necessary for the implementation of this research was the collection of geometric data for the pre-debulked and debulked arteries. The data were collected in an appropriate clinical setting (Integra Solutions, Brooklyn Park, MN) by making use of a previously frozen cadaver. Prior to the debulking procedure, a precisely timed longitudinal transverse was carried out with an ultrasound probe in order to determine the geometry of the artery and its plaque content. The longitudinal traverse produced 300 images, each image being a slice of thickness 0.1 mm. Subsequently, a surgical procedure was performed at the upper thigh to enable introduction of the Diamondback debulking device. The position of the device was achieved by angiographic imaging. Once properly positioned, the device was periodically traversed through the plaqued artery in a longitudinal manner during a 90-second interval. A photograph of the exposed artery is shown in Figure 3.1. A 30-mm length of the just-debulked artery was selected to provide the geometry for comparison with that of the pre-

debulked artery. Care was taken to use the same 30-mm sample for the pre-debulked and debulked artery evaluation.

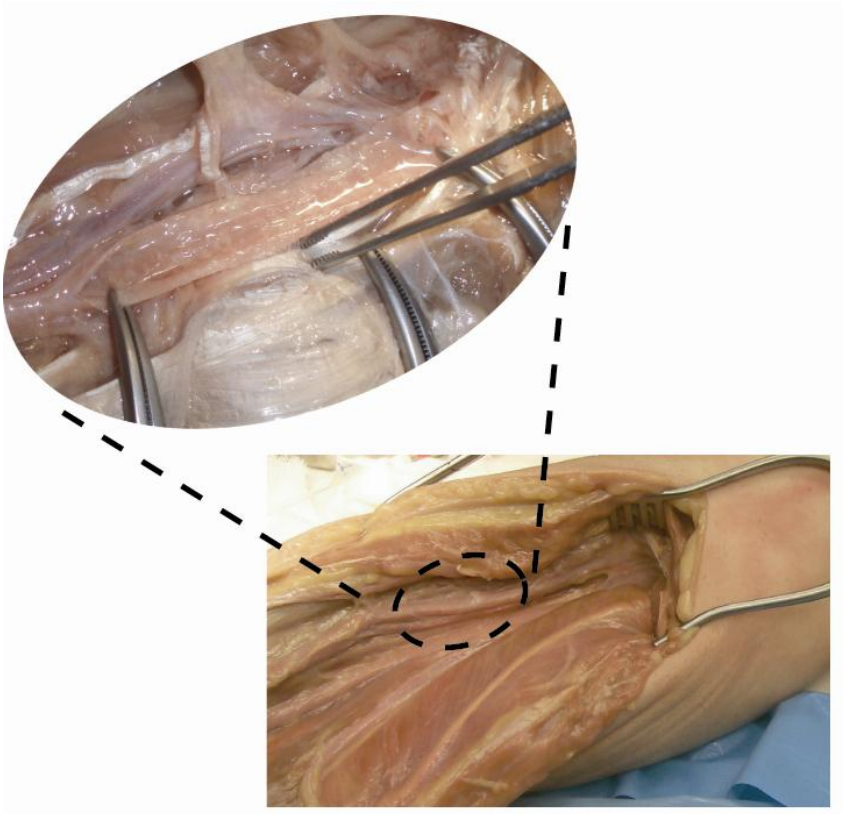

Figure 3.1: Photograph showing cadaver with exposed posterior tibial artery. Callout shows closeup view of posterior tibial artery after debulking. Excised artery shows the absence of arterial plaque.

The photographs in Figure 3.1 show a wide view of the cadaver leg displaying the opened region and the exposed artery system of the lower leg. A callout shows a closeup view of the targeted artery which was treated by the debulking process. The artery has been cut open to show that the inner wall is free of plaque, after the debulking process.

Ultrasonic evaluation of both the pre and post configurations was made. An illustrative set of images of a cross section of the artery showing features of the two states is presented in Figure 3.2. The figure shows the lumen boundary before and after the debulking process. A comparison of the boundary clearly shows an increased lumen diameter as a result of the procedure.

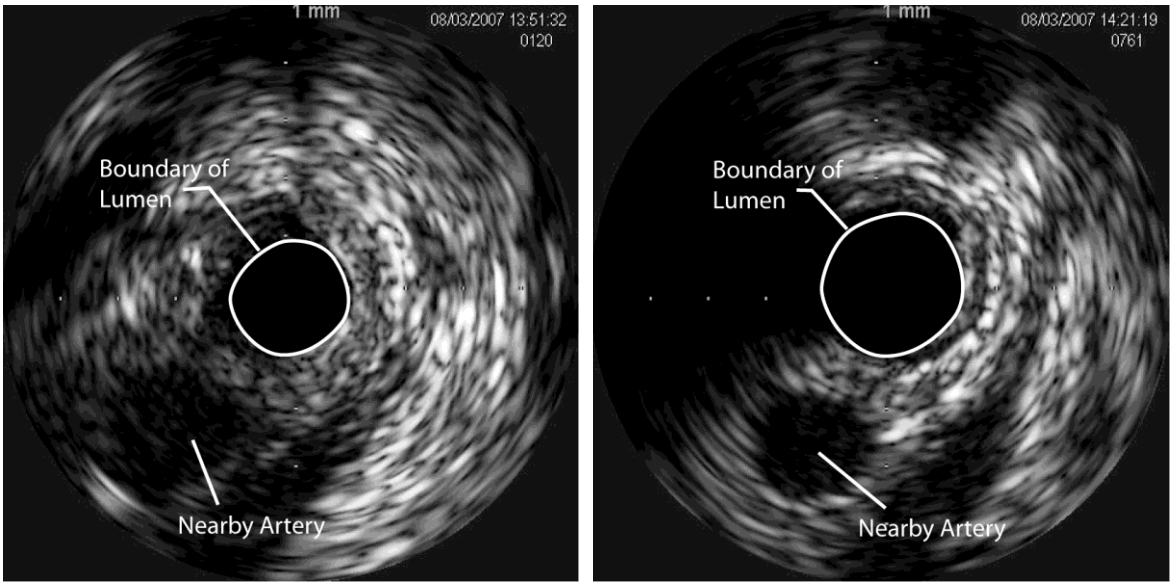

(a) (b)

Figure 3.2: Intravenous ultrasound images of the cross section of a posterior tibial artery before (a) and after (b) debulking.

The reconstitution of the geometric images was accomplished by use of Amira 4.1 and Maya 7.0 software programs. To facilitate the use of these programs, the boundary each slice was smoothed by a splining technique. The outcome of this process was solid-model files with highly precise geometric detail, as shown in Figure 3.3. These solid-

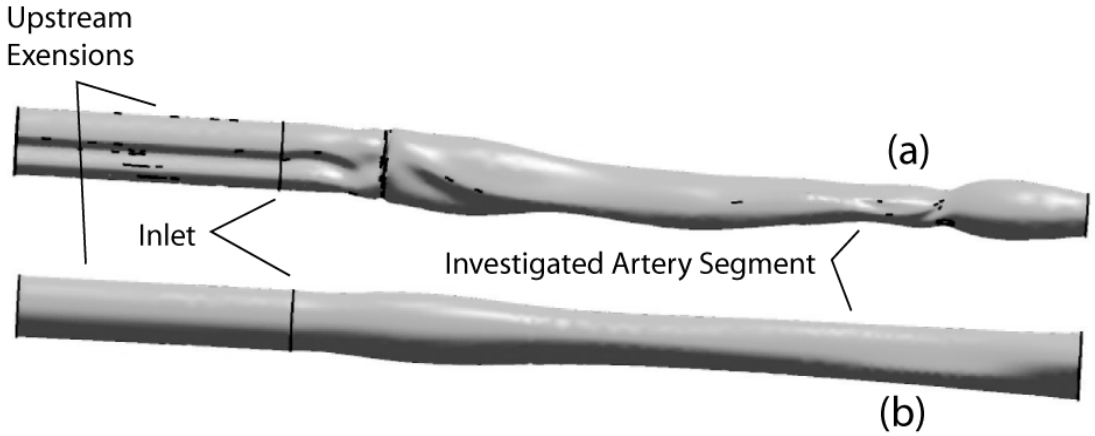

Figure 3.3: Reconstituted geometries of the bounding walls of the lumen before (a) and after (b) debulking of the artery.

model files were then employed as input to information to the numerical simulation that will now be described.

3.2 Mathematical Model

The geometries of the fluid flow passages corresponding to the pre-debulked and post-debulked arteries have been determined as described in Section 3.1. Attention will now be turned to the analysis of the three-dimensional, unsteady flow in these highly irregular tubes. For the analysis, the flow will be regarded as incompressible and the fluid properties to be constant. Two constitutive equations will be employed in the simulation. One is laminar, Newtonian flow, and the other is laminar, non-Newtonian flow. The equations governing the flow are, first, conservation of mass, and second, momentum conservation. Mass conservation is expressed as

$$\frac{\partial u}{\partial x}+\frac{\partial v}{\partial y}+\frac{\partial w}{\partial z}=0 \tag{3.1}$$

In this equation, the cross-sectional coordinates are *x* and *y* while the *z* is the axial coordinate. The corresponding velocities are *u*, *v*, and *w*.

The three momentum equations that were solved in this analysis are

$$\rho\left(\frac{\partial u}{\partial t}+\frac{\partial}{\partial x}\left(u^2\right)+\frac{\partial}{\partial y}(u\upsilon)+\frac{\partial}{\partial z}(uw)\right)=-\frac{\partial p}{\partial x}+\frac{\partial \tau_{xx}}{\partial x}+\frac{\partial \tau_{yx}}{\partial y}+\frac{\partial \tau_{zx}}{\partial z} \tag{3.2}$$

$$\rho\left(\frac{\partial \upsilon}{\partial t}+\frac{\partial}{\partial x}(u\upsilon)+\frac{\partial}{\partial y}\left(\upsilon^2\right)+\frac{\partial}{\partial z}(\upsilon w)\right)=-\frac{\partial p}{\partial y}+\frac{\partial \tau_{xy}}{\partial x}+\frac{\partial \tau_{yy}}{\partial y}+\frac{\partial \tau_{zy}}{\partial z} \tag{3.3}$$

$$\rho\left(\frac{\partial w}{\partial t}+\frac{\partial}{\partial x}(uw)+\frac{\partial}{\partial z}(\upsilon w)+\frac{\partial}{\partial z}\left(w^2\right)\right)=-\frac{\partial p}{\partial z}+\frac{\partial \tau_{xz}}{\partial x}+\frac{\partial \tau_{yz}}{\partial y}+\frac{\partial \tau_{zz}}{\partial z} \tag{3.4}$$

The shear stresses appearing in these equations were alternatively evaluated by making use of the Newtonian viscosity of blood, μ = 0.00345 kg/m-s, reported in [3.19] or the Ostwald-de Waele non-Newtonian constitutive model described in [3.22]. The latter model is represented by

$$\tau = K\gamma^n \tag{3.5}$$

in which K = 0.0147 (kg/m-s$^{1.22}$) and n = 0.78 [3.23]. This non-Newtonian model is frequently used in the analysis of blood flow. In a previous study of a physical situation which possesses some similarities to that studied here [3.24], it was found that the end results were independent of the values of K and n within the normally accepted range for blood [3.23, 3.25].

3.3 Implementation of the Simulation Model

3.3.1. Spatial and temporal boundary conditions:

Blood flow is a cyclic process so that it is only necessary to focus on a single cycle to obtain representative results. In order to obtain a realistic reproduction of the physical situation, information about the cyclic velocity in the posterior tibial artery was extracted from [3.26]. The cited cross-sectional-average velocity information is reproduced in Figure 3.4. Note that the period of the cyclic variation is 1 second. The curve shown in that figure is representative of measurements made in 78 individual arteries in a group of subjects, ages 19-32, who were selected for not having angiographically documented arterial disease.

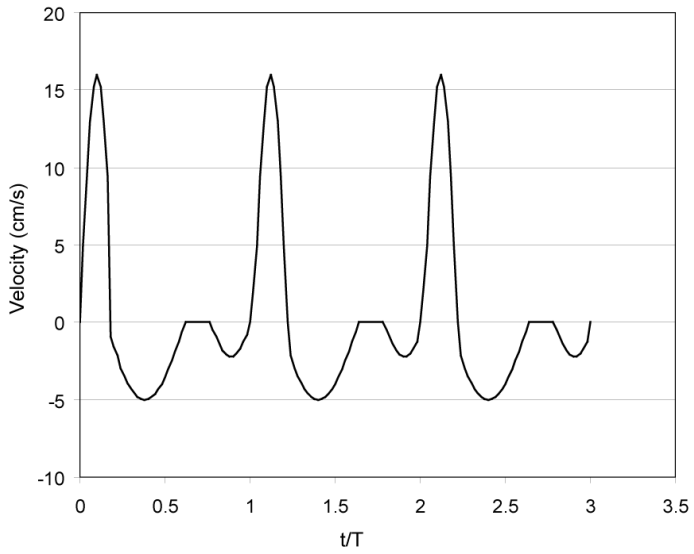

Figure 3.4: Velocity waveform applied to debulked artery segment.

This information was used as input to the simulations of the debulked artery. On the basis of the numerical results extracted from the simulation, the timewise-varying pressure difference between the respective ends of the investigated length of artery was found. This pressure difference was, in turn, applied to the simulation of the pre-debulked artery. The outcome of this procedure was the timewise variation of the flowrates passing through the debulked and undebulked arteries. The comparison between these flowrates constitutes the definitive improvement of vascular health affected by the debulking procedure.

3.3.2. Details of the numerical method:

The calculations were carried out using CFX 11.0, a commercial finite-volume-based CFD program. Continuity and momentum are conserved over each element in the mesh, and overall conservation throughout the entire domain is thereby guaranteed. Solutions were carried out for five cardiac cycles with the view of identifying the periodic steady state. In all cases, it was found that the solution attained the periodic steady state after two cycles of calculations. At each time step, a false-transient approach was employed to enable convergence. The number of iterations performed at each time step was governed by the requirement that the residuals of all transported variables were less than 10^{-5}. In

each iteration, a multigrid strategy was used in which contiguous elements are clustered into numerous larger elements, as described by [3.27].

The initial time was set at 0.01 seconds, and subsequent time steps were bounded between 0.001 and 0.1 seconds. At each moment of time, the time step was chosen so that convergence of the iterative process to the aforementioned criterion is accomplished well within 10 iterations. The transient discretization scheme is second-order backward difference.

Coupling of the velocity-pressure equations was achieved on a non-staggered, collocated grid using the techniques developed by [3.28-3.29]. The inclusion of pressure-smoothing terms in the mass conservation equation suppresses oscillations which can occur when both the velocity and pressure are evaluated at coincident locations.

The advection term in the momentum equations was evaluated by using the upwind values of the momentum flux, supplemented with an advection-correction term. The correction term reduces the occurrence of numerical diffusion and is of second-order accuracy. Details of the advection treatment can be found in [3.30].

The fact that there is both forward flow and back flow during a given cycle required special consideration which is not needed in normal unidirectional fluid flows. In particular, to deal with such flows, the standard inflow and outflow boundary conditions have to be carefully reexamined. The inflow boundary in the CFX software does permit both positive and negative velocity components. On the other hand, the outflow boundary does not permit flow reversal. Therefore, the outflow boundary condition could not be applied at the downstream end of the length of artery investigated. Instead, it was necessary to employ a special condition (*opening*) in which the software calculates the direction of the flow provided that the pressure at the opening is specified. If the flow passes outward through the opening, the applied boundary condition for all the dependent variables is that their streamwise second derivatives are zero.

At the inlet of the investigated artery, the solution domain was extended upstream to investigate the impact of a hydrodynamic starting length. For this purpose, three starting lengths were used, one at the inlet proper, a second at a distance of approximately five diameters upstream of the inlet, and a third approximately ten diameters upstream. When the simulation model results were obtained for the mass flowrate predictions for these three cases, it was found that they could not be visually distinguished from each other. In this light, all subsequent numerical simulations were performed using the model in which the upstream extension of the solution domain was positioned five diameters from the investigated artery segment.

The solution domain was initially discretized by approximately 105,000 elements. A mesh-independence study was subsequently performed with 250,000 elements. The resulting values of the time-integrated mass flowrates from these two meshes agreed to within 1%. The quality of the mesh was tailored by a process called inflation so that the elements could be concentrated in regions of high gradients adjacent to the walls of the artery, as seen in Figure 3.5.

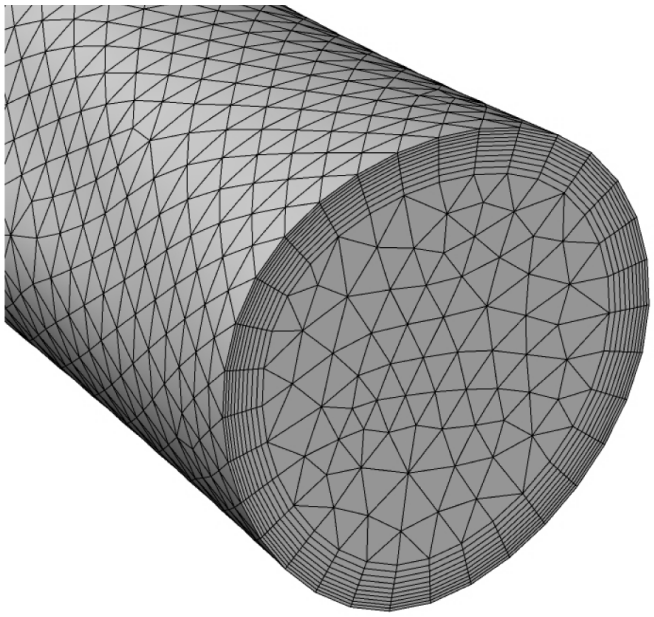

Figure 3.5: Display of the computational mesh showing boundary layer elements deployed along the lumen wall.

3.4 Results and Discussion

3.4.1. Mass flow and pressure results:

The main result of clinical importance is the increase in the rate of blood flow through the debulked artery relative to that carried prior to debulking. These results were obtained by making use of the Ostwald-de Waele non-Newtonian constitutive model. The issue of the impact of the constitutive model will be addressed shortly.

The cycle-integrated results for these quantities are presented in Table 3.1. The table separately lists the integrated flowrates through the systolic and diastolic periods, both for the pre-debulked and debulked artery configurations. In addition, the increases in these flowrates that result from debulking are highlighted in the rightmost column of the table.

Table 3.1: Mass flowrates for pre-debulked and debulked artery segments.

	Pre-Debulked	Debulked	Ratio: Post/Pre
Systole Flow (grams/cycle)	0.0353	0.0859	2.43
Diastole Flow (grams/cycle)	0.0186	0.0521	2.80
Net Flow (grams/cycle)	0.0166	0.0338	2.04

It can be seen that the debulking has a major positive impact on the rate of blood flow. The flowrates after debulking are on the order of 2.5 times those prior to debulking. The clinical importance of this finding is that the lower leg and foot will be strongly perfused such that the health of the cells in those regions will be significantly enhanced.

As was set forth in the introduction, one of the major aims of this work is to provide a quantitative metric for the assessment of the efficacy of various debulking modalities. It

can be seen from Table 3.1 that the modality evaluated here can be regarded as being very highly effective in carrying out the mission of improving blood flow by debulking.

A more detailed assessment of the effect of debulking on the mass flowrates can be obtained by examining how the instantaneous flowrates vary during the course of a cycle. This information is displayed in Figure 3.6. That figure not only compares the flowrates for the pre-debulked and debulked situations but also exhibits the variation of the end-to-end pressure drop throughout the cycle.

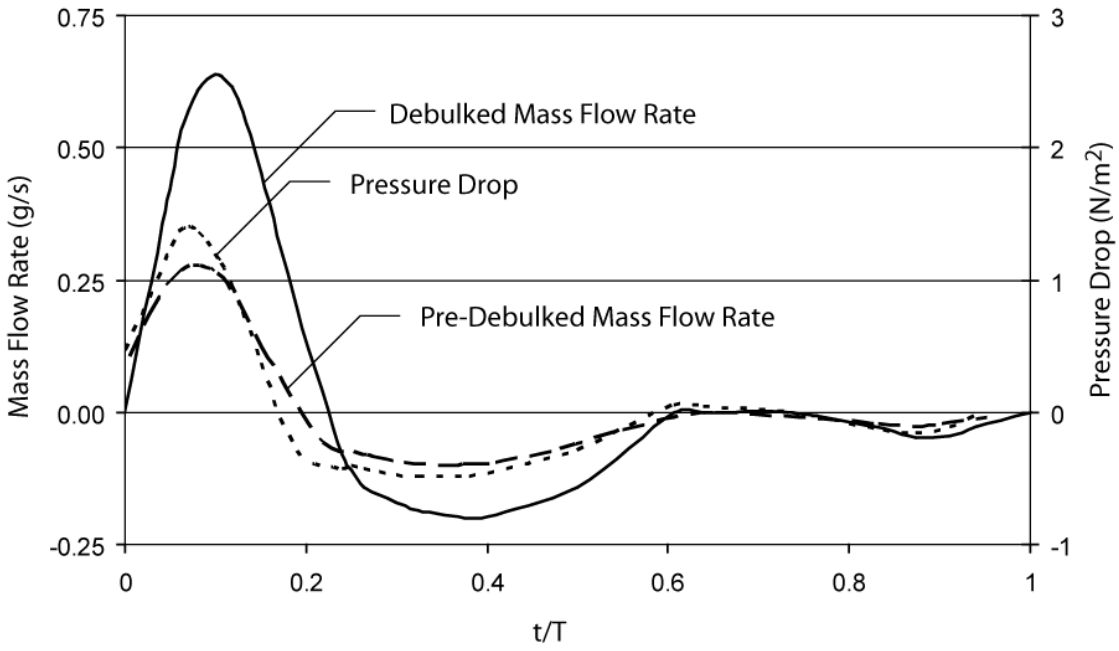

Figure 3.6: Mass flowrates for pre-debulked and debulked arteries in response to a timewise cardiac pressure variation.

Note that there is a single curve for the pressure drop without designation between the pre-debulked and debulked situations. This is because the two situations share a common end-to-end pressure drop as the driving potential for fluid flow. This use of a common pressure drop imposed on the two artery configurations was deemed the most appropriate way of comparing their fluid flow capabilities.

Of particular interest with regard to Figure 3.6 is that the timewise variations of the fluid-flow lag with those of the pressure. For example, the pressure changes sign well before the respective flows change direction. This occurrence is in evidence both when the pressure changes from positive to negative and also when the change is from negative to positive.

Attention will now be turned to results obtained using a Newtonian constitutive equation. A comparison between the mass flowrate for the debulked artery calculated with the non-Newtonian and Newtonian models is made in Figure 3.7. The figure shows that for both the systole and diastole periods, the predicted flowrates for the Newtonian model exceeded those for the non-Newtonian model. The deviations are moderate but consistent throughout the entire cycle. This finding can be made plausible on the basis of physical reasoning. The non-Newtonian model gives rise to an effective viscosity that is higher than the viscosity that appears in the Newtonian model. The relevance of the choice of the constitutive model will be dealt with shortly when the shear stress results are presented.

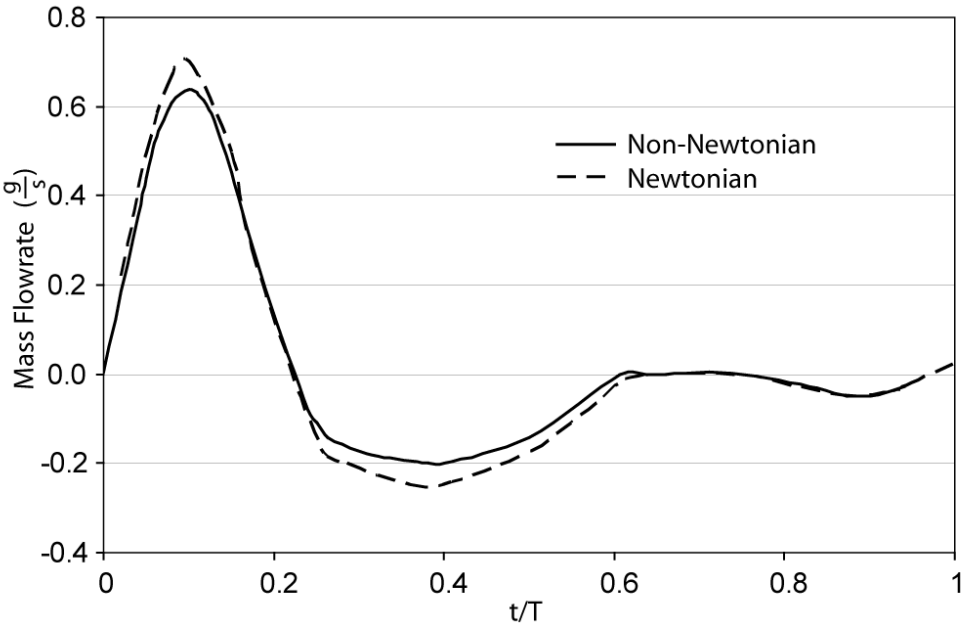

Figure 3.7: Effect of non-Newtonian and Newtonian constitutive models on the mass flowrate in a debulked artery.

3.4.2 Wall shear stress results:

It is well established by [3.1-3.2] that the thickness of the plaque layer is strongly related to the magnitude of the wall shear stress. This fact calls attention to the shear stress as an important factor in the development or the arrestment of a plaque layer. In particular, it is known that high shear stresses are protective with respect to the avoidance of plaque buildup.

The shear stress may be examined from several standpoints. In essence, it is a local and instantaneous quantity, depending on position (circumferential and longitudinal) and on time. A second portrayal of the shear stress might be made by first performing a circumferential average over lumen perimeter at various longitudinal positions, resulting in longitudinal-spatial and temporal variations. A global spatial average, over both circumferential and longitudinal variations, is another useful form of the shear. This double average, $\bar{\bar{\tau}}$, varies with time.

The first of the shear results to be presented is the timewise variation of $\bar{\bar{\tau}}$, both for the undebulked and debulked artery segments. These results, presented in Figure 3.8, correspond to the non-Newtonian model. In a subsequent figure, these results will be compared with those based on the Newtonian model.

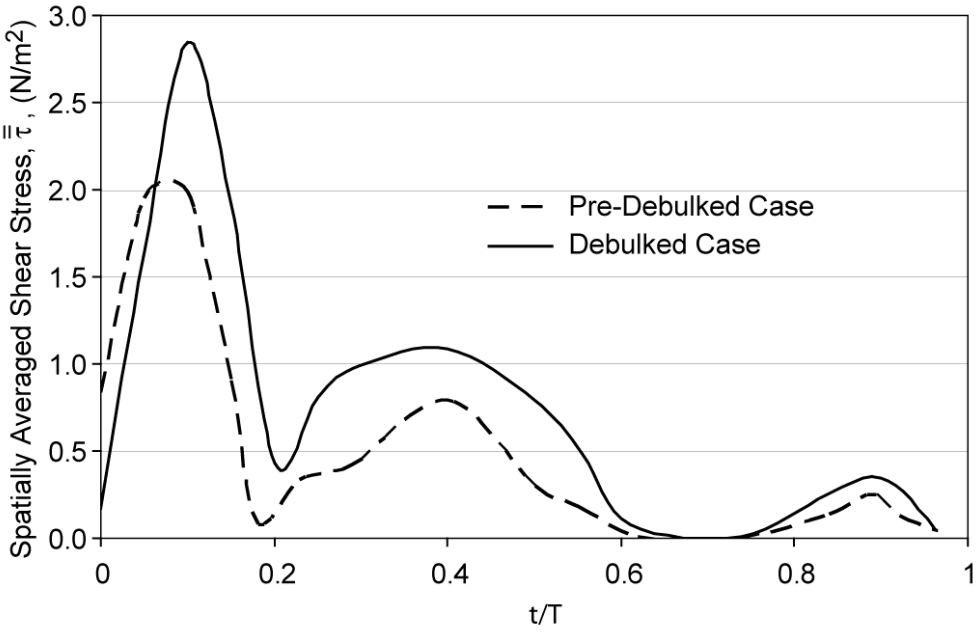

Figure 3.8: Spatially averaged (circumferential and longitudinal) wall shear stress.

An overall appraisal of this figure indicates that the magnitude of $\bar{\bar{\tau}}$ for the debulked artery segment is, for most of the cardiac cycle, larger than that for the pre-debulked segment. When considering this result, it is relevant to take account of the many factors that influence the magnitude of the wall shear. Among these are the magnitude of the velocity, the roughness of the lumen wall, and larger-scale geometric features. Also, in a time-dependent situation such as that considered here, the inertia of the fluid in responding to timewise pressure variations is significant with regard to the magnitude of the wall shear stress. This issue is of particular relevance at the beginning of the systolic period. As can be seen from Figure 3.8, during that period, the shear stress for the pre-debulked case is higher than that for the debulked artery. It is believed that this ordering of the shear results is directly related to the lower inertia of the pre-debulked flow. Aside from this relatively short period of time, it is seen that the shear stresses for the debulked case are larger than those for the pre-debulked situation. This arrangement is clearly the result of the greater magnitude of the velocities for the former.

A more local view of the shear stress results is exhibited in Figure 3.9. In that figure, the circumferential averaged shear stress, $\bar{\tau}$, is plotted as a function of position along the

investigated artery segment for selected instances within a cardiac cycle. The figure is subdivided into two levels, the upper corresponding to the pre-debulked artery and the lower to the debulked case. Each of these levels has its own ordinate scale.

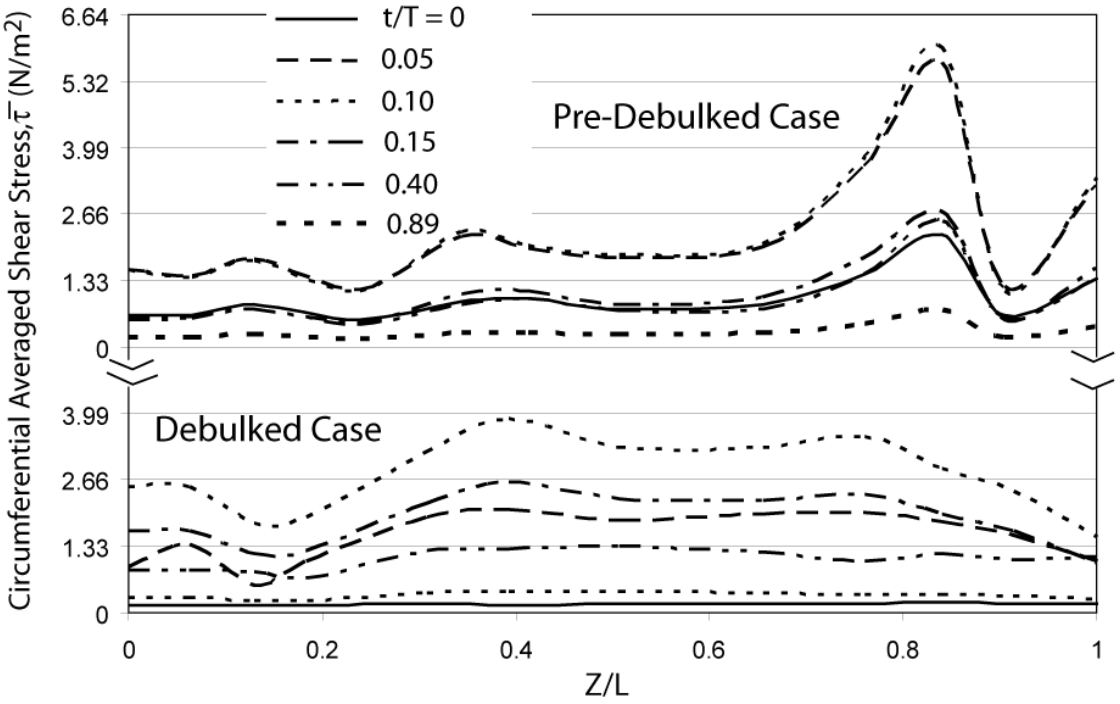

Figure 3.9: Circumferentially averaged wall shear stress variations along the length of the investigated artery as a function of time.

The main issues to be examined in Figure 3.9 are the longitudinal variations of the shear stress for the respective pre-debulked and debulked cases. For the former, if the rise in the shear stress at the downstream end of the artery section is ignored, it appears that for the remainder of the section, the longitudinal variations are smaller than those for the debulked case. The aforementioned downstream rise can be understood by referring to Figure 3.3(a). That figure shows a necking down of the artery cross section just before the downstream end of the segment, and it is the higher velocities that result from the diminished cross section that are responsible for the rise in shear stress. The subsequent drop and rise of the shear stress coincide with an enlargement and follow-on contraction of the lumen.

If attention is next turned to the debulked case, the undulation of the shear stress curves in the upstream half of the artery segment can be closely keyed to the variations in the artery cross section that are in evidence in Figure 3.3(b).

Focus will now be directed to a comparison between the spatially averaged wall shear stress for the cases of Newtonian and non-Newtonian flows through the debulked artery segment. This information is displayed in Figure 3.10 where the averaged shear stress is plotted as a function of time throughout the cardiac cycle. In general, it is seen that the temporal variations of the shear for the two cases tend to track each other. There are, however, differences in detail. In particular, in the early part of the systolic portion, there are significant differences in the shear, with that for the Newtonian case exceeding the non-Newtonian values. A plausible explanation of this finding may be made by recognizing that at high shear rates, the Newtonian viscosity significantly exceeds the effective non-Newtonian viscosity. Furthermore, high shear rates may be associated with higher velocities. The combination of these observations supports the findings conveyed in the figure.

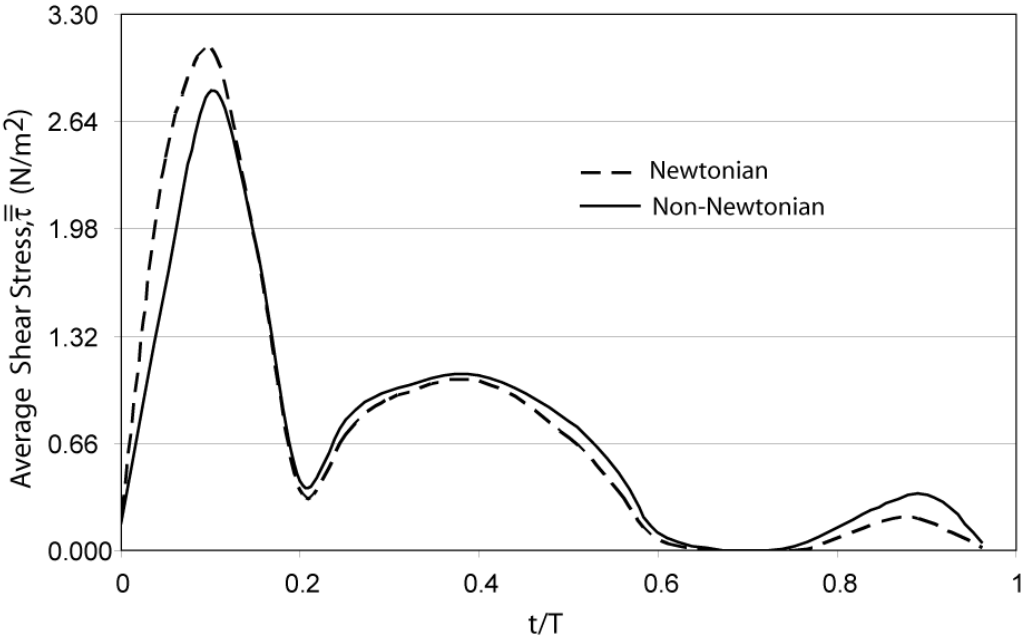

Figure 3.10: Comparison of spatially averaged wall shear for Newtonian and non-Newtonian constitutive models. The results correspond to flow simulations through the debulked artery segment.

3.4.3. Global patterns of flow and wall shear stress:

Focus will now be directed to exhibiting the patterns of fluid flow and wall shear stress which prevail throughout the selected artery segment. First, a set of diagrams setting forth velocity information is presented in Figure 3.11. The figure is subdivided into upper and lower tiers which correspond, respectively, to the debulked and pre-debulked artery segments. In each tier, there are four contour diagrams which are parameterized by the instant of time to which they correspond. This information was extracted from the three-dimensional velocity solutions by means of a cutting plane which was passed through the largest diameter of the inlet cross section of the arterial segment. The axial velocity magnitudes are conveyed by color while the lengths of the vectors correspond to the magnitude of the velocity. Note that the direction of the velocity vectors indicates the presence of forward flow (the leftmost three diagrams in each tier) and backflow (the rightmost diagram).

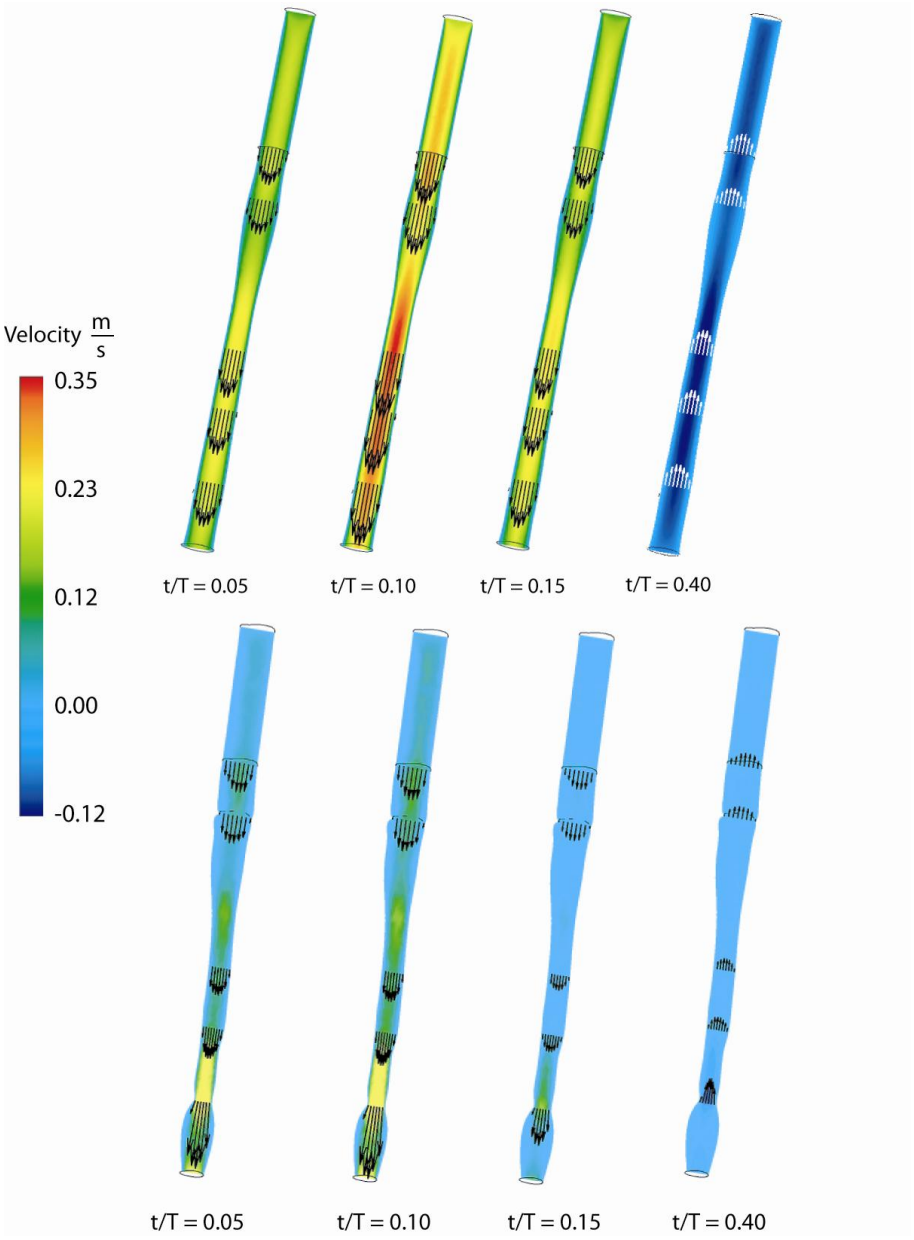

Figure 3.11: Velocity vector and contour diagrams for the debulked artery segment (upper tier) and the pre-debulked segment (lower tier). The color is indicative of the magnitude of the axial velocity, while the lengths of the vectors correspond to the velocity magnitude.

An overall view of Figure 3.11 shows that the magnitudes of the velocity are greater for the debulked case. The velocity profiles for that case are relatively symmetric and orderly. On the other hand, for the pre-debulked case, there is clear evidence of the

absence of symmetry and of a radial component at the location of the divergent area near the lower end of the artery segment.

Next, attention is turned to a display of the wall shear stress results exhibited in terms of color-contour diagrams in Figure 3.12. In this figure, there are two tiers, respectively corresponding to the debulked and pre-debulked cases. When viewed in an overall manner, it is seen that the level of the shear stresses in the debulked case exceeds those of the pre-debulked case. Only in highly localized regions, specifically at the abrupt contraction situated just upstream of the lower end of the artery, are there large shear stresses for the latter case. The presence of these high shear stress values has already been identified in connection with the discussion of Figure 3.9. In general, the shear stresses are more uniform in the debulked artery than in the pre-debulked artery.

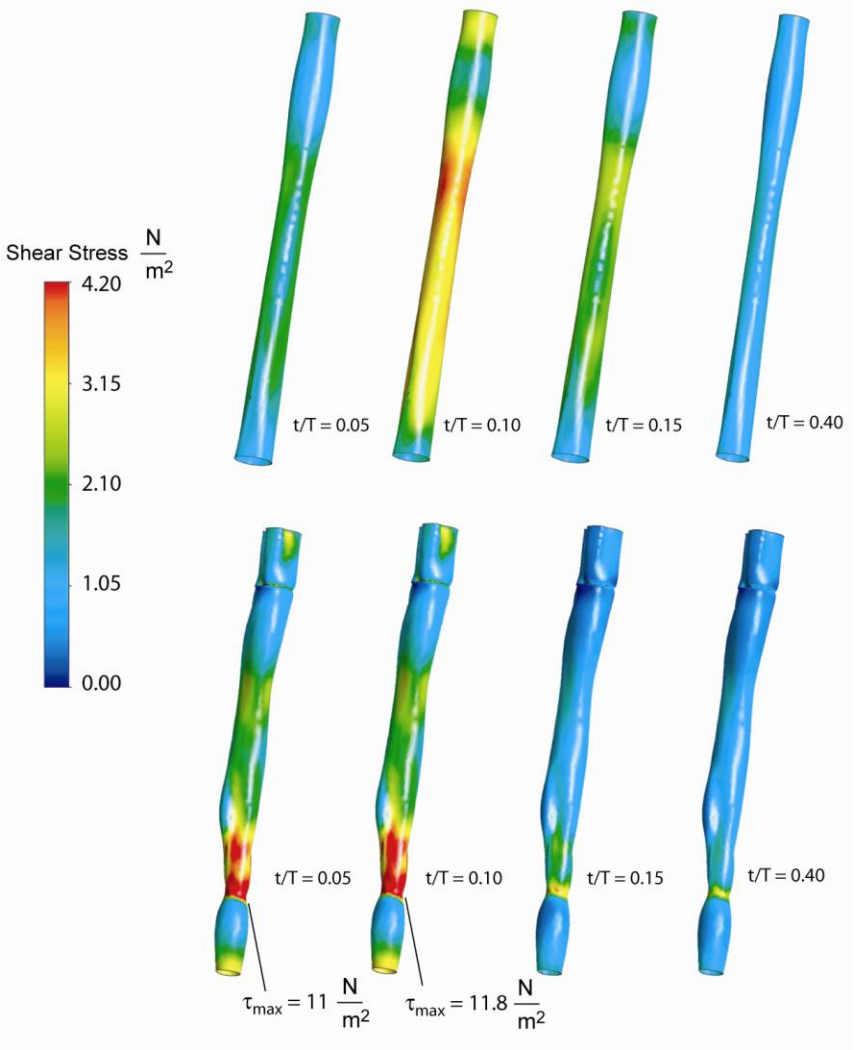

Figure 3.12: Wall shear stress patterns corresponding to the debulked (upper tier) and pre-debulked (lower tier) artery segment. The magnitude of the wall shear is color-keyed to the legend at the left. For the three leftmost diagrams in each tier, the direction of the wall shear is vertically downward whereas for the rightmost diagram, the stress direction is vertically upward.

3.5 Concluding Remarks

It has been demonstrated that fluid mechanic analysis can play a significant role in the evaluation of medical therapeutic procedures. The particular situation that has been dealt with here is the debulking (plaque removal) from small arteries. The major issue that motivated this work is the need to evaluate the end result of the procedure. By means of a three-dimensional, unsteady fluid-flow analysis in both the pre-debulked and debulked artery geometries, it was found that the debulking methodology (orbital atherectomy),

accomplished by use of the Diamondback 360° Orbital Atherectomy System (Cardiovascular Systems, Inc., St. Paul, MN) led to increases in blood flow on the order of 2.5 times for both the systole and diastole periods of the cardiac cycle based on the application of the timewise end-to-end pressure variation to both the pre-debulked and debulked cases.

It is recognized that the magnitude of the wall shear stresses exerted by the blood flow has a significant effect on plaque accumulation and intimal wall thickness. Consequently, special attention was given to the magnitudes of the wall shear for both the pre-debulked and debulked artery segments. It was found that, in general, the shear stresses in the debulked artery were both more uniform and higher than those in the pre-debulked artery. This favorable result suggests that the rate of plaque accumulation and arterial wall thickening in arteries will be diminished by the debulking.

References Chapter 3:

[3.1] D. Ku, Blood flow in arteries, Ann. Rev. Fluid Mech. 29 (1997) 399-434.

[3.2] C. Taylor, T. Hughes, Z. Zarins, Finite element modeling of three dimensional pulsatile flow in the abdominal aorta: relevance to atheroscleroris, Ann. Biomed. Eng. 27 (2000) 975-987.

[3.3] P. Neofytou, D. Drikakis, Non-Newtonian flow instability in a channel with a sudden expansion, J. Non-Newtonian Fluid Mechanics 111 (2003), 127-150.

[3.4] S. O'Callaghan, M. Walsh, T. McGoughlin, Comparison of finite volume, finite element and theoretical predictions of blood flow through an idealized femoral artery, 2003 Summer Bioengineering Conference, June 25-29, 2003. Key Biscayne, Fl.

[3.5] J. LaDisa, I. Guler, L. Olson, D. Hetterick, J. Kersten, D. Warltier, P. Pagel, Three-dimensional computational fluid dynamics modeling of alterations in coronary wall shear stress produced by stent implantation, Ann. Biomed. Eng**.** 31 (2003) 972-980.

[3.6] M. Grigoni, C. Daniele, M. Umberto, C. Del Gaudio, G. D'Avenio, A. Balducci, and V. Barbaro, A mathematical description of blood spiral flow in vessels: application to a numerical study of flow in arterial bending, J. Biomech. Eng. 38 (2005) 1375-1386.

[3.7] F. Abraham, M. Behr, and M. Heinkenschloss, Shape optimization in steady blood flow: a numerical study of non-newtonian effects, Comp. Methods Biomech. 8 (2005) 127-137.

[3.8] Z. Ding, K. Wang, J. Li, and X. Cong, Flow field and oscillatory shear stress in a tuning-fork-shaped model of the average human carotid bifurcation, J. Biomech. Eng. 34 (2001) 1555-1562.

[3.9] A. Berhier, R. Bouzerar, and C. Legallais, Blood flow patters in an anatomically realistic coronary vessel: influence of three different reconstruction methods, J. Biomech. Eng. 35 (2002) 1347-1356.

[3.10] N. Shahcheraghi, H. Dwyer, A. Cheer, A. Barakat, and T. Rutaganira, Unsteady and three-dimensional simulation of blood flow in the human aortic arch, J. Biomech. Eng. 124 (2002) 378-386.

[3.11] M. Oshima, R. Torii, T. Kobayashi, N. Taniguchi, and K. Takagi, Finite element simulation of blood flow in the cerebral artery, Comp. Methods Appl. Mech. Eng. 191 (2001) 661-671.

[3.12] Q. Long, X. Xu, K. Ramnarine, and P. Hoskins, Numerical investigation of physiologically realistic pulsatile flow through stenosed arteries, J. Biomech. Eng. 34 (2001) 1229-1242.

[3.13] U. Krueger, J. Zanor, and H. Scholz, Computational fluid dynamics and vascular access, Artificial Organs, 26 (2002) 571-575.

[3.14] P. Marques, M. Oliviera, A. Franca, and M. Pinotti, Modeling and simulation of pulsatile blood flow with a physiologic wave pattern, Artificial Organs, 27 (2003), 478-485.

[3.15] I. Marshall, S. Zhao, P. Papathanasopoulou, P. Hoskins, and X. Xu, MRI and cfd studies of pulsatile flow in healthy and stenosed carotid bifurcation models, J. Biomech. Eng., 37 (2004) 679-687.

[3.16] J. Chen and X. Lu, Numerical investigation of the non-newtonian pulsatile blood flow in a bifurcation model with a non-planar branch, J. Biomech. Eng., 39 (2006) 818-832.
[3.17] F. Gijsen, F. van de Vosse, and J. Janssen, The influence of the non-newtonian properties of blood on the flow in large arteries: steady flow in a carotid bifurcation model, J. Biomech. Eng., 32 (1999) 601-608.
[3.18] Y. Cho and K. Kensey, Effects of the non-newtonian viscosity of blood on flows in a diseased arterial vessel. part 1: steady flows, Biorheology, 28 (1991) 241-261.
[3.19] B. Johnston, P. Johnston, S. Corney, and D. Kilpatrick, Non-Newtonian blood flow in human right coronary arteries: steady state simulations, J. Biomech. Eng., 37 (2004) 709-720.
[3.20] D. Tang, C. Yang, S. Kobayashi, and D. Ku, Steady flow and wall compression in stenotic arteries: a three-dimensional thick-wall model with fluid-wall interactions. J. Biomech. Eng., 123 (2001) 548-557.
[3.21] D. Tang, C. Yang, H. Walker, S. Kobayashi, and D. Ku, Simulating cyclic artery compression using a 3d unsteady model with fluid-structural interactions,Comp. and Struct., 80 (2002) 1651-1665.
[3.22] R. Bird, W. Steward, and E. Lightfoot, Transport Phenomena, John Wiley & Sons, New York, NY, 960.
[3.23] F. Walburn and D. Schneck, A constitutive Equation for Whole Human Blood, Biorheology, 13 (1976) 201-210.
[3.24] J. Abraham and E. Sparrow, Simulation of Fluid Flow Through a Trauma Fluid-Warming Device, Laboratory for Heat Transfer and Fluid Flow Practice, Report AZ-1, December, 2006.
[3.25] D. Liepsch and S. Moravec, Pulsatile flow of non-Newtonian fluids in distensible models of human arteries, Biorheology, 20 (1983) 745-754.
[3.26] A. Fronek, M. Coel, and E. Bernstein, Quantitative ultrasonographic studies of lower extremity flow velocities in health and disease, Circulation, 53 (1976) 957-960.
[3.27] B. Hutchinson and G. Raithby, A multigrid method based on the additive correction strategy. Num. Heat Transfer B, 9 (1986) 511-537.
[3.28] C. Rhie and W. Chow, A numerical study of the turbulent flow past an isolated airfoil with trailing edge separation, AIAA Paper no. 82-0998 (1982).
[3.29] S. Majumdar, Role of underrelaxation in momentum interpolation for calculation of flow with nonstaggered grids, Num. Heat Transfer B, 13 (1988) 125-132.
[3.30] T. Barth and D. Jesperson, The design and applications of upwind schemes on unstructured meshes. AIAA Paper no. 89-0366 (1989).

Chapter 4:
Tissue damage potential of neuromodulation devices due to magnetic-field heating

4.0 Introduction

Safety considerations have evoked considerable recent interest in the interaction of external magnetic fields with implanted metallic objects in the human body. One application which has been regarded as critical with respect to the general impact of this interaction is the use of MRI as a diagnostic tool. A second situation where a similar interaction occurs is when an implant is empowered by a magnetic field dispersed by an antenna situated on the skin surface in the near proximity of the implant. The externally applied magnetic field penetrates the tissue and induces eddy currents in the metallic implant or other structures. The induced currents, in turn, produce Ohmic heating. In addition, possible chemical reactions due to the recharging process may also produce heat. The concern is that Ohmic and chemically produced heating may give rise to local elevated temperatures which may cause tissue necrosis. The current literature dealing with this heating phenomenon is well documented [4.1-4.12]. These papers run the gamut from MRI-based heating to antenna-based heating. In addition to the aforementioned thermal effect, the external magnetic field may also interfere with the primary function of the implanted device, an occurrence which has been reported in literature of which [4.13-4.16] are representative.

The investigation to be described here seeks to quantify the impact of the heating effect caused by the interaction of an externally applied magnetic field and an implant. The specific situation to be considered is a neuromodulation implant whose battery is recharged by a skin-surface-mounted antenna. The three neuromodulation devices investigated here are the Medtronic Restore, the ANS Eon, and the Boston Scientific Precision. In a previous paper [4.17], careful *in vitro* experiments were performed to obtain the rate of energy transfer from the surfaces of the implant to the adjacent tissue. These rates, taken from [4.17] are 233, 670, and 441 mW, respectively for the Medtronic

Restore, the ANS Eon, and the Boston Scientific Precision. In addition, the experiments provided the following data: 200, 343, and 931 mW, respectively for the Medtronic Restore, the ANS Eon, and the Boston Scientific Precision for the energy transfer rate from the antenna surfaces to its environment.

In the work to be described here, new and different experiments were performed to quantify the rates of energy transfer specific to each of the principal surfaces of the implant. These experiments were performed with the respective implants suspended in air. To avoid uncertainties attributable to random air currents, the suspended implant was partially shrouded. A heat-flux sensor was affixed to each of the principal surfaces of the implant. These sensors provided a direct reading of the heat flux passing from the surface to the surrounding environment. To create a situation in which heat was generated within the implant, the antenna that corresponded to each implant was suspended parallel to the implant and separated from it by a distance of one cm. Once the setup had been created, the antenna was activated to initiate and maintain the recharging of the implant. When steady state had been established, the heat fluxes passing from the respective principal surfaces to the air environment were read electronically. The outcome of these experiments yielded the percentage of the total heat transfer rate leaving the principal surfaces that is attributable to each principal surface. For the Medtronic Restore, 29 percent of the heat transfer from principal surfaces was attributable to the surface that faces the skin. The corresponding numbers for the ANS Eon and Boston Scientific Precision implants are 44 and 37 percent, respectively. The percentages passing through the surface that faces the deeper portions of the tissue bed are 71, 56, and 63.

These data, together with those of [4.17], were then used as the basis of a numerical simulation model of the energy transfers within the tissue. To achieve a high level of accuracy for the numerical predictions, the detailed internal structure of the antennas was carefully taken into account. By this detailed modeling, it was possible to precisely identify the energy transfers from the respective bounding surfaces of the antennas and the evolution of the temperature field within the tissue.

The investigation was performed for three different neuromodulation systems, the Medtronic Restore, the ANS Eon, and the Boston Scientific Precision. For each of these devices, the temperature distribution in the tissue in the neighborhood of the implant and the antenna was determined. Careful attention was given to the specification of the boundary conditions for the analysis. Specifically, clothing worn over the antenna plus heat transfer by convection and radiation to the environment formed the basis of one of the employed boundary conditions. Another boundary condition was based on the patient oriented so that the antenna was in contact with an insulating material such as that of a sofa or a mattress.

The simulation was performed for transient operation, with the transient being initiated by the activation of the antenna's magnetic field. The period of the heating was extended over a duration of two hours. This period of application of the device is believed to cover most practical utilizations.

The special focus of the work was to investigate conditions which could give rise to local tissue necrosis during the recharging of the aforementioned neuromodulation devices.

4.1 Physical and Mathematical Models

A schematic display of the physical model is conveyed in Figure 4.1. The model is, in fact, axisymmetric, and a cut along a diametril plane (a vertical plane which is cut through a diameter) is exhibited in the figure. The tissue bed is characterized as a four-layer assemblage, encompassing the skin, fat, fascia, and muscle layers. The respective thicknesses of these layers are 2, 30, 1, and 25 mm. These thicknesses were selected on the basis of a consultative discussion with a plastic surgeon [4.18]. The selected thickness of the fat layer was sufficiently great to fully encompass the implant. In view of the fact that the fat layer has the lowest thermal conductivity and the lowest blood perfusion rate among all the others, the positioning of the implant in that layer necessarily gives rise to an upper bound on the temperature at the interface of the implant and the tissue. The implant depth, which is defined in Figure 4.1, is one cm for all the

investigated implants. The thicknesses of the implants are 13.9, 15.6, and 10.5 mm for the Medtronic Restore, ANS Eon, and Boston Scientific Precision, respectively. Note that Figure 4.1 shows that the axes of the implant and the antenna are perfectly aligned.

Figure 4.1 is a representation of the volume in which the numerical solutions were performed. All of the dimensions of that space have been conveyed in the foregoing, aside from the radius which defines the outer edge and the dimensions of the antenna. The outer radius of the solution space was taken to be two and a half times the radius of the antenna. The antenna radii are 39.1, 40.3, and 35.6 mm, respectively, for the Medtronic Restore, ANS Eon, and Boston Scientific Precision devices.

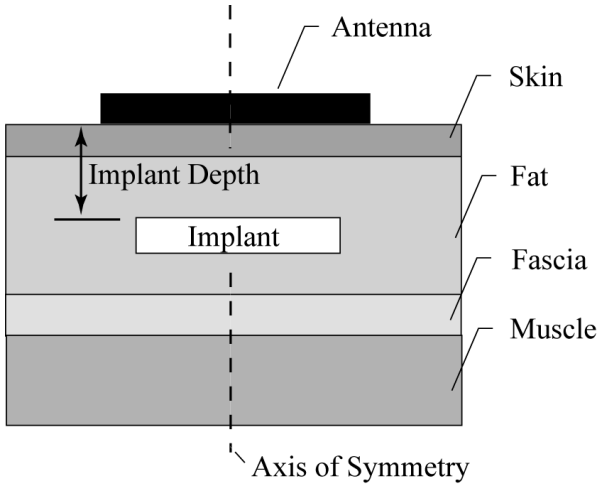

Figure 4.1: Schematic diagram of the system to be investigated, showing the four tissue layers, the skin-surface-mounted antenna, and the implant.

A complete listing of the properties of the selected tissue layers is provided by Table 4.1. The properties were chosen after an extensive review of the literature and may be regarded as representative of the non-pathological patients.

Table 4.1: Properties of the tissue layers.

Tissue	Layer thickness (mm)	Thermal conductivity (W/m-K)	Density (kg/m^3)	Specific heat (J/kg-K)	Median blood perfusion rate (1/s)	Metabolic heating rate (W/m^3)
Skin	2	0.45 [19]	1100 [21]	3500 [19]	0.0018 [23]	1300 [25]
Fat	30	0.2 [20]	960 [21]	2500 [24]	0.000425 [26]	250 [25]
Fascia	1	0.23 [21]	1000 [21]	3900 [21]	0.000425 [26]	250 [25]
Muscle	25	0.5 [22]	1040 [21]	3600 [24]	0.0005 [27]	500 [25]

The energy transfers in the tissue bed can be modeled by applying the first law of thermodynamics. That law is, in fact, a balance of the inflows and outflows of energy into a control volume. The energy flows that are considered are: (a) heat conduction, (b) perfusion-carried energy, and (c) metabolic heat generation. When these various transports are in balance, a steady state is achieved. The most commonly accepted form of the first law for biological thermal transport is the Pennes equation [4.28]. This model has provoked a considerable amount of controversy over many decades. Despite this, it has been demonstrated to be viable by comparisons between the predictions of the model and experimental data. The Pennes equation is

$$\rho c \frac{\partial T}{\partial t} = k \frac{\partial^2 T}{\partial z^2} + \frac{k}{r} \frac{\partial}{\partial r}\left(r \frac{\partial T}{\partial r} \right) + (\rho c)_b \omega (T_a - T) + S \,. \qquad (4.1)$$

This equation is written for an axisymmetric model, justifying the use of cylindrical coordinates. Also worthy of note is that it takes account of unsteady temperature variations. The solutions to be obtained will encompass not only the transient state but also will provide the steady state which occurs as the limit as time increases.

In this equation, the thermal physical properties are k, ρ, and c, which are the thermal conductivity, the density, and the specific heat of tissue, respectively and ρ_b, c_b, which are, respectively, the density and specific heat of blood. The specific rate of blood flow is represented by ω which has units of $(m^3/s)/(m^3)$. The numerator of this unit cluster is the volumetric flow rate, while the denominator represents the volume of tissue through

which the blood is perfusing. Also appearing in Eq. (4.1) is a baseline temperature T_a. According to Pennes, T_a represents the temperature of the arterial blood which perfuses through the tissue. Metabolic heat generation is denoted by S, which corresponds to a volumetric heat source. The dependent variable is the temperature T, which is a function of the axial and radial coordinates, r and z, respectively. Aside from the independent and dependent variables, numerical values of the other quantities that appear in Eq. (4.1) are listed in Table 4.1, except for blood, for which $\rho_b = 1000$ kg/m^3 and $c_b = 4000$ J/(kg-K).

The goal of this investigation is to solve Eq. (4.1) to obtain the maximum temperatures in the tissue caused by the heat generation in the implant and the antenna. The presence of those devices is not reflected in Eq. (4.1). The heat generation within the implant will enter the problem as a boundary condition. On the other hand, the antennas of all of the devices will be modeled in their own right, and the energy transfers within each of them are governed by a form of the first law that differs from Eq. (4.1). In fact, in view of the complicated geometry of the internal parts of the antenna, it was necessary to solve a separate governing equation for each part. If the subscript i is used to identify each part, then the relevant form of the first law is

$$(\rho c)_i \frac{\partial T_i}{\partial t} = k_i \frac{\partial^2 T_i}{\partial z^2} + \frac{k_i}{r} \frac{\partial}{\partial r}\left(r \frac{\partial T_i}{\partial r} \right) + S_i . \tag{4.2}$$

In those parts of the antenna where heat generation occurs due to Ohmic heating, the heat source term S_i has a constant value. On the other hand, certain parts of the antenna merely act as heat conductors, and in those parts, $S_i = 0$. To illustrate the complexity of the interior of an antenna, Figure 4.2 has been prepared. It is a vertical cut through the antenna showing a cross section. This antenna is specific to the Medtronic Restore device. In this cross-sectional view, 10 different materials are identified. Some of these materials appear in more than one location in the antenna. Of particular note is the heat-generating element as indicated in the diagram (part 1). In the particular antenna that is illustrated, there are 15 separate parts, each of which necessitates the solution of a separate differential equation such as Eq. (4.2).

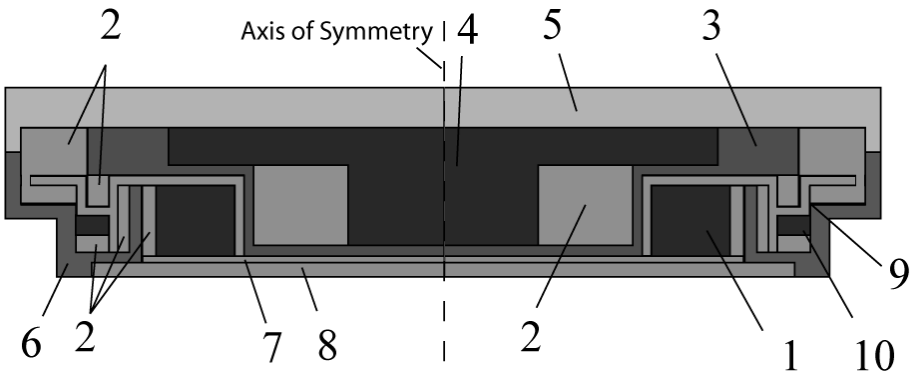

1 - Heating Coil
2 - Air Space
3 - Delrin
4 - Ferrite
5 - ABS and PC
6 - 10% Glass-Filled PC
7 - Thermal Pad
8 - Polypropylene
9 - Polyamide
10 - Passive Copper Coil

Figure 4.2: Vertical cut through an antenna illustrating the presence of numerous separate parts.

Inspection of Figure 4.2 reveals the presence of air gaps. Since the bounding surfaces of the air gaps are necessarily at different temperatures, it is appropriate to consider the possibility of natural convection occurring in these gaps. This possibility was examined by making use of the Rayleigh number criteria for the onset of flow in both horizontal and vertical enclosures. For all of the air gaps that occur in the antenna pictured in Figure 4.2, it was found that the Rayleigh number was well below that for the onset of flow. This same issue arose for the Boston Scientific Precision antenna. A calculation of the Rayleigh number for the air gap that exists in that antenna also gave rise to a value below the critical. There is no air gap in the ANS Eon antenna.

To complete the specification of the problem, it is necessary to provide boundary conditions and conditions of continuity at interfaces. With reference to Figure 4.1, the exposed surfaces of the antenna and the exposed surface of the skin were assigned continuous boundary conditions. Two boundary conditions were considered. One of

these took account of convection to the surrounding ambient in the presence of garments covering the antenna and the skin surface. The thermal resistances of the garments and the convective resistance of the air were lumped into an overall pseudo heat transfer coefficient. A second boundary condition was based on modeling a situation where the antenna and skin surface interfaced with a thick insulating material such as an upholstered chair or a bed. For that case, an adiabatic boundary condition was imposed.

At the interface between the base of the antenna and the contiguous skin surface, perfect contact was assumed. At the radial limits of the solution domain that is shown in Figure 4.1, it was assumed that the influence of the presence of both the antenna and the implant had died away. Consequently, an adiabatic boundary condition was appropriate. With regard to the bottom of the tissue bed, it was uncertain as to what would be the proper boundary condition, since the overall depth of the bed was unlikely to be thick enough to impose the core temperature. This uncertainty led to the selection of the adiabatic condition, whose adoption would give rise to temperatures that correspond to an *upper bound* on the actual temperature field. However, subsequent computation experience demonstrated that the use of this boundary condition gave rise to overtemperatures on the order of 0.2°C. At all other interfaces, continuity of temperature and heat flux was required.

As noted earlier, the implant was not included in the solution domain. Rather, on the basis of experiments reported in [4.17] and extended as part of the present research, the heat flux leaving the surfaces of the implant and entering the tissue were known quantities. These known heat fluxes were applied as boundary conditions at the interface of the implant and the contiguous tissue. The data provided by [4.17] were the *total rate of heat transfer* from all faces of the implant to its surroundings. Additional experiments performed here utilizing heat flux sensors enabled accurate determinations of the *separate heat flow rates* from the two principal surfaces. In particular, these experiments showed that for the Restore, Eon, and Precision, the percentages of the total energy leaving the implant that is transferred from the skin-facing surface are 29, 44, and 37, respectively.

The actual numerical computations were performed within the framework of ANSYS 11.0. The accuracy of the numerical solutions was validated by a mesh independence study. Meshes consisting of 75600 and 108000 elements were employed for this study. The temperature maximum was monitored for these two mesh densities, and it was found that agreement prevailed to within 0.01°C for all times during the transient process.

4.2 Results and Discussion

4.2.1 Temperature distributions and hot-spot temperatures:

The result of most immediate interest is the magnitude of the hot-spot temperature within the tissue bed and its location. This information is conveyed in Figures 4.3, 4.4, and 4.5, respectively for the Boston Scientific Precision, ANS Eon, and Medtronic Restore devices. The results displayed in these figures correspond to a time following one hour of recharging of the batteries of the respective devices. Also, the thermal boundary condition at the exposed surfaces (the outer surface of clothing covering the skin and the antenna) was natural convection and radiation to the surroundings. In interpreting the results conveyed by these figures, it is well to keep in mind that an axisymmetric model has been used for the numerical simulation. To provide a realistic portrayal, the figures display a 180° revolution of the basic two-dimensional geometry.

The figures display color contour diagrams of the temperatures both within the tissue and the antenna. The temperature levels are correlated to the color scale that is situated beneath the contour diagram. Note that a common color scale is used for all of these figures. From an overview of the figures, it is clear that the highest hot-spot temperature within the tissue (45.6°C) is attained when the Boston Scientific Precision device is employed. The hot-spot temperature associated with the ANS Eon is somewhat lower (41.1°C) than that of the Boston Scientific Precision device. The lowest of the hot-spot temperatures is that with the use of the Medtronic Restore device (39.2°C). With regard to the location of these hot-spot temperatures, it can be seen that for the Precision device, the location is at the skin surface. On the other hand, for both of the other two devices, the hotspot is located adjacent to the bottom surface of the implant.

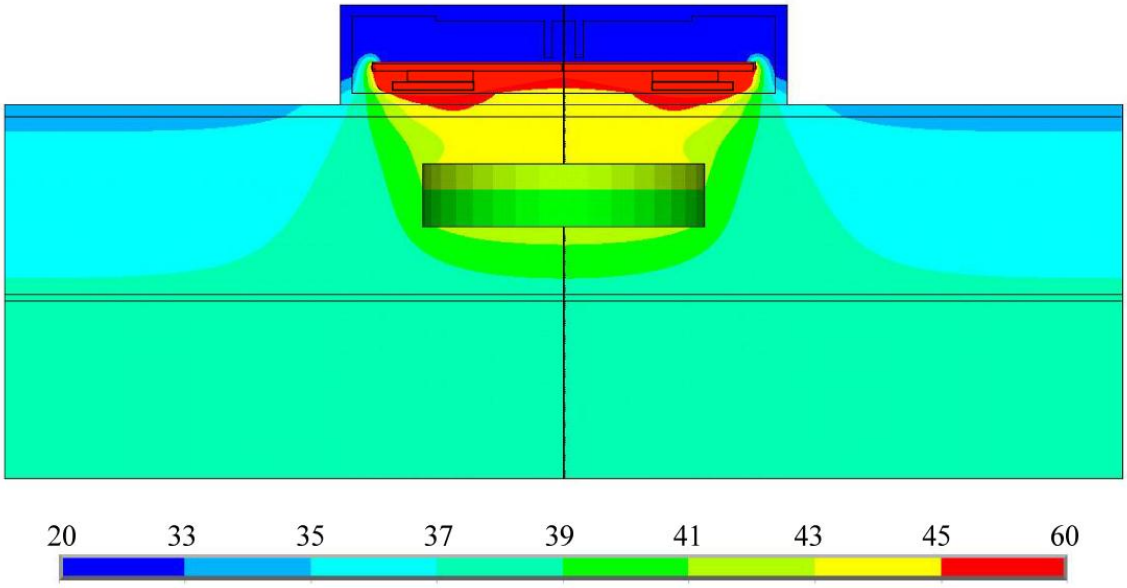

Figure 4.3: The temperature distribution (°C) associated with the Boston Scientific Precision device after one hour of recharging. Note that temperatures above 50°C are encountered in the antenna and not in the tissue. The maximum tissue temperature is 45.6°C. The apparent discontinuity between the temperatures of 33 and 45°C in the antenna is due to the very high thermal resistance of an air gap.

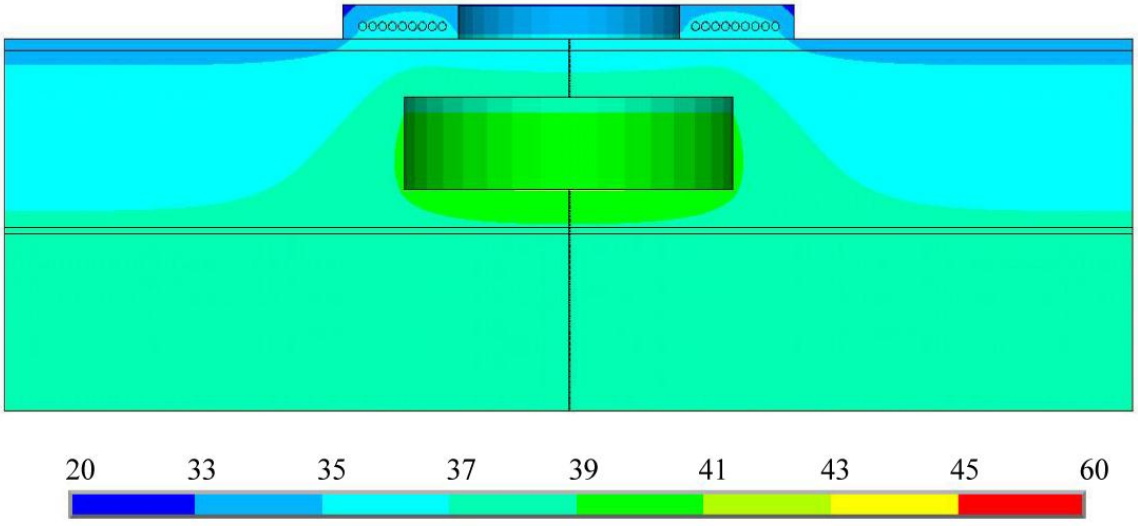

Figure 4.4: The temperature distribution (°C) associated with the ANS Eon device after one hour of recharging. The maximum temperature in the tissue is 41.1°C.

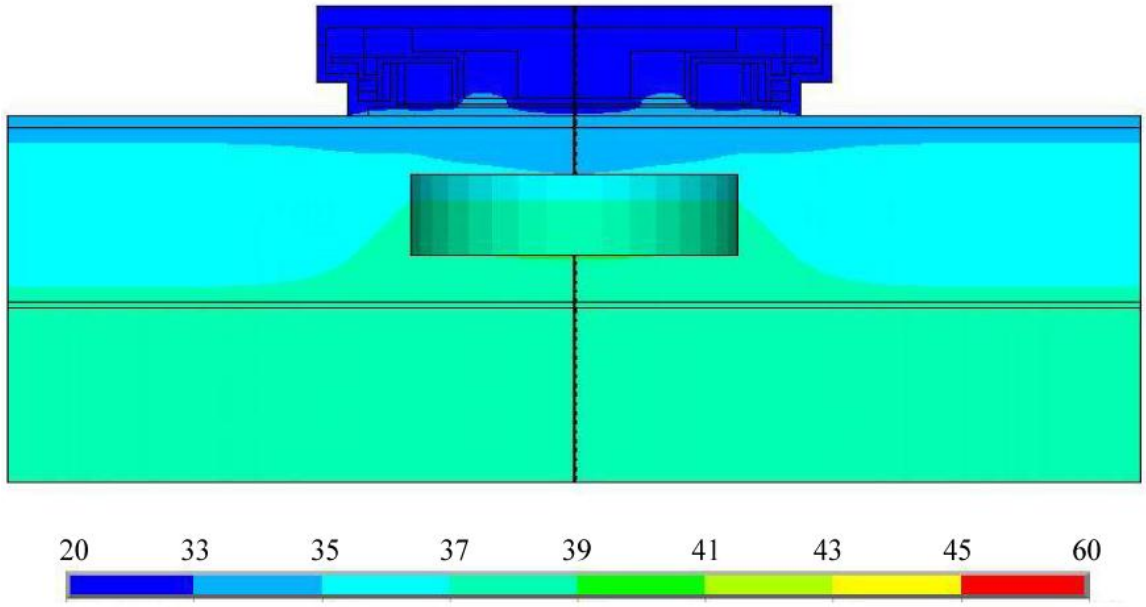

Figure 4.5: The temperature distribution (°C) associated with the Medtronic Restore device after one hour of recharging. The maximum tissue temperature is 39.2°C.

Among the three aforementioned hot-spot temperatures, only that for the Precision device might possibly suggest cell damage. It is known that cell necrosis is a function not only of temperature level, but it also depends on the time duration at which the elevated temperature exists. The issue of cell necrosis will be treated in greater depth shortly when time durations of various extents are considered.

Color contour diagrams similar in content to Figures 4.3, 4.4, and 4.5 were examined for the thermal boundary condition of no heat transfer at the exposed surfaces of the skin and the antenna. That inspection indicated only small differences from the contours that were exhibited for the case of surface convection. Therefore, the contour diagrams for the adiabatic case will not be presented here.

More detailed information about the timewise variation of the hot-spot temperatures is conveyed in Figures 4.6, 4.7, and 4.8. In each of these figures, the hot-spot temperature is plotted as a function of time for each of the devices being considered. The time span for which results are presented is 60 minutes. Figure 4.6 shows results for the three

devices in the presence of surface convection. These results are delineated by curves of different line types. The highest temperatures achieved during the one hour recharging period are those for the Boston Scientific Precision. The hot-spot location for that device shifted from the bottom surface of the implant at early times to the skin-antenna interface at later times. This change of site is responsible for the change of slope of the curve for this device. The intermediate temperatures are those for the ANS Eon, the site of which was the bottom surface of the implant. The lowest of the hot-spot temperatures are those for the Medtronic Restore. At relatively short times during the recharging period, the hot-spot temperatures of the various devices differ by approximately 3°C, while at larger times differences as large as 6.5°C are in evidence.

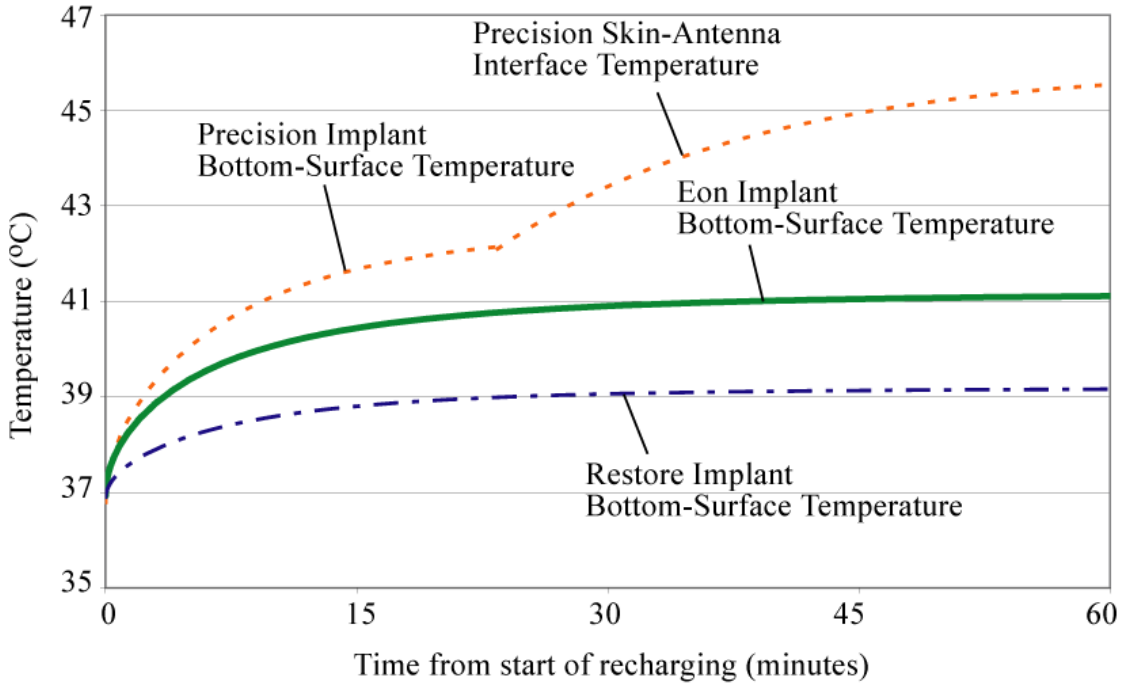

Figure 4.6: Hot-spot temperatures for all three devices corresponding to a 20°C convective environment.

The counterpart of Figure 4.6 which conveys similar results for the case of no heat transfer at the exposed surfaces is Figure 4.7. Examination of these figures indicates only minor differences in detail. Over all, the maximum deviations in the hot-spot temperatures for the two thermal boundary conditions are, at most, one degree Celsius.

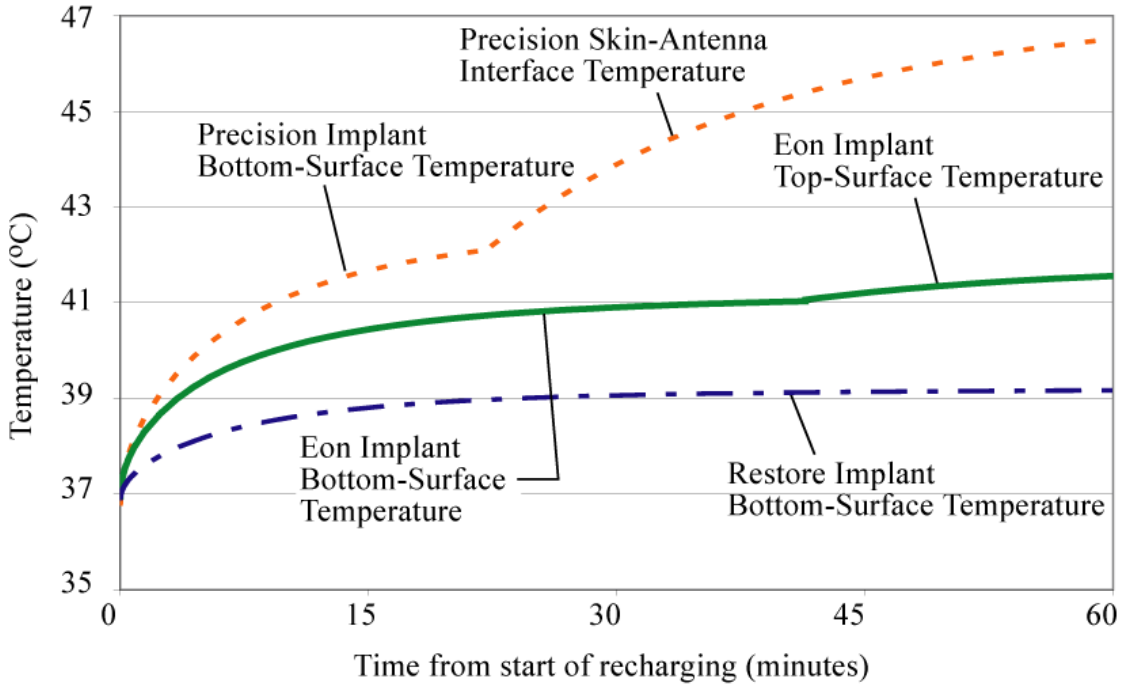

Figure 4.7: Hot-spot temperatures for all three devices corresponding to an adiabatic environment.

Next, attention is turned to a display of the outcome of a sensitivity study in which the blood perfusion rate was varied by +/- 50% around the nominal value that was listed in Table 4.1. The hot-spot temperatures corresponding to the three perfusion rates for each of the three devices are exhibited in Figure 4.8. In that figure, three clusters of curves are shown, with the uppermost cluster corresponding to the Precision device, the middle to the ANS Eon, and the lower to the Medtronic Restore. For the latter two devices, the curves are consistently ordered with respect to the blood perfusion rate, with the highest hot-spot temperatures corresponding to the lowest perfusion rate and the lowest hot-spot temperature belonging to the highest perfusion. With respect to the Precision device, the just-described ordering of the curves also describes the results for times greater than 20 minutes. At lesser values of time, the ordering is reversed. It is especially important to note that both the ANS Eon and the Medtronic Restore give rise to hot-spot temperatures that are not very sensitive to the perfusion rate. On the other hand, the Boston Scientific Precision is much more sensitive to perfusion, especially at relatively long recharging times. For example, for a recharging time of 60 minutes, the perfusion-caused spread in the hot-spot temperature is approximately 3.5°C.

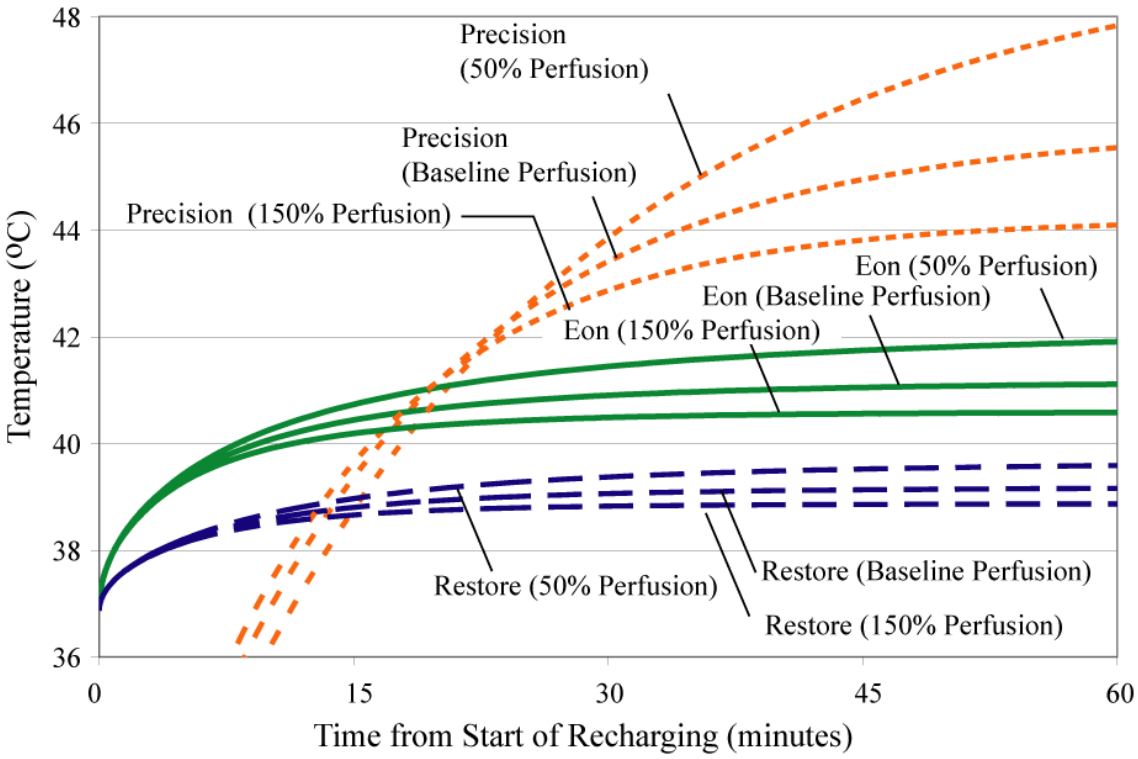

Figure 4.8: Dependence of the hot-spot temperatures on the blood perfusion rate.

It is convenient to summarize the key results of the foregoing paragraphs in tabular form. This information is provided by Table 4.2. The table lists the hot-spot temperatures for each of the investigated devices at 15, 30, 45, and 60 minutes of recharging. Also listed in the table are the results for the two boundary conditions, convective and adiabatic. The distinction between these results is made by placing the adiabatic-based temperatures in parentheses. The results exhibited in the table correspond to the properties that are listed in Table 4.1.

Inspection of the table confirms the observations that have been reported from the discussions of the figures. Among the devices, the highest temperatures are those for the Boston Scientific Precision, the intermediate temperatures correspond to the ANS Eon, while the lowest temperatures are those for the Medtronic Restore. The table also confirms the minor differences that are attributable to the differences in the thermal boundary conditions, convective versus adiabatic.

Table 4.2: Summary of the hot-spot temperature results at different durations of recharging (°C).

Device	Duration of recharging (minutes)			
	15	30	45	60
Precision	41.7 (41.7)	43.4 (43.9)	44.9 (45.7)	45.6 (46.5)
Eon	40.4 (40.4)	40.9 (40.9)	41.1 (41.2)	41.1 (41.6)
Restore	38.8 (38.8)	39.1 (39.1)	39.1 (39.1)	39.2 (39.2)

4.2.2 Tissue injury:

The impact of the temperatures displayed in Table 4.2 on possible cell necrosis will now be considered. To this end, use is made of the Henriques-Moritz [4.29] cell injury criterion, which is

$$\Omega(t) = A\int_0^t e^{-E_A/(\overline{R}T)} d\tau \ . \tag{4.3}$$

In this equation, E_A is the activation energy, $\overline{R}$ is the universal gas constant, τ is the variable of integration, and A is the so-called pre-exponential constant. The values of E_A and A are specific to each of the tissue layers. Those for skin, A = $2.20*10^{124}$ s^{-1} and E_A = $7.84*10^5$ J/mole, were used for the evaluation of the integral [4.30]. The computed timewise temperatures $T(\tau)$ were introduced into the integrand and the integration was performed numerically. The results for Ω are listed in Table 4.3. The table exhibits Ω values for device recharging times of one and two hours. Separate results are listed for the two considered thermal boundary conditions, convection to an environment at 20°C and adiabatic exposed surfaces. The results for the latter are delineated by parentheses.

Table 4.3: Cumulative thermal injury imparted to hot-spot tissue locations due to device recharging.

Device	Duration of recharging (hours)	
	1	2
Boston Scientific Precision	0.071 (0.15)	0.35 (1.0)
ANS Eon	0.0023 (0.0024)	0.0058 (0.0059)
Medtronic Restore	0.00041 (0.00041)	0.00092 (0.00093)

There is a consensus that cell necrosis occurs for values of Ω on the order of one. In this light, it appears that only for the case of the Boston Scientific Precision device is there a danger of necrosis for recharging periods on the order of two hours. For this device operating at shorter durations and for all the other devices, it appears that no cell necrosis occurs. It is noteworthy that both the Medtronic Restore and the ANS Eon yield very low values of Ω for all of the time durations considered. This observation suggests that they are absolutely safe with regard to thermal injury of tissue with regard to the investigated conditions.

4.3 Concluding Remarks

The thermal implications of biomedical implants activated by magnetic fields have been investigated here by means of numerical simulation making use of experimentally determined device heat generation measurements. The specific type of implant that motivated this investigation is neuromodulators. In essence, the implant is the secondary of a transformer, while the primary (the antenna) is situated on the skin surface. The specific implant-antenna arrangement considered here is a separation of the two components by a tissue layer of one centimeter, and the axes of the components are perfectly aligned. The original experiments obtained data for the rate at which heat is transferred from all of the surfaces of the respective implant devices to the surroundings. Further experiments performed here determined the fractions of that heat transfer rate attributable to the respective principal surfaces of each device.

The numerical simulations, based on these inputs and on thermophysical properties and perfusion rates from the literature, predicted the magnitude and location of the maximum

temperature created in the tissue as a result of the recharging process of the implant battery. These so-called hot-spot temperatures were determined for three of the most used neuromodulators: (a) Boston Scientific Precision, (b) ANS Eon, and (c) Medtronic Restore.

The critical heating period for these devices is that during which recharging of the implant's battery is taking place. For durations of the recharging between 30 and 60 minutes, the predicted hot-spot temperatures are 42.5 to 45.5°C for the Precision, 41°C for the Eon, and 39°C for the Restore. These temperatures correspond to the thermal boundary condition whereby there is convective and radiative heat transfer to a 20°C environment. For the other investigated situation, where the thermal boundary condition was specified to be adiabatic, the corresponding temperatures are 44 to 46.5°C for the Precision, 41 to 41.5°C for the Eon, and 39°C for the Restore. These temperature levels suggest that, at least for the case of the Precision device, there is a possibility of tissue damage.

To quantify the possibility of tissue damage, the Henriques-Moritz tissue damage integral was used to combine the effects of temperature level and duration of the recharging period. For a recharging period of one hour, the damage integral for all of the three devices yielded numbers much less than one that is the accepted indicator of tissue necrosis. If the heating period encompasses a two-hour duration, the damage integral for both the Eon and Restore produce values which are, once again, much smaller than one. The values of the damage integral for the Precision device for the two-hour recharging are 0.35 and 1.0, respectively, for the convective-radiative condition and the adiabatic boundary condition (a worst case) at the exposed surfaces. This outcome suggests that caution be exercised when using this device.

References Chapter 4:

[4.1] G. Calcagnini et al, In vitro investigation of pacemaker lead heating induced by magnetic resonance imaging: role of implant geometry, Journal of Magnetic Resonance Imaging, 28 (2008) 879-886.

[4.2] S. A. Mohsin, N. M. Sheikh, U. Saeed, MRI induced heating of deep brain stimulation leads: effect of the air-tissue interface, Progress in Electromagnetics Research, 83 (2008) 81-91.

[4.3] S. Park, R. Kamondetdacha, J. Nyenhuis, Calculation of MRI-induced heating of an implanted medical lead wire with an electric field transfer function, Journal of Magnetic Resonance Imaging, 26 (2007) 1278-1285.

[4.4] K. Yassi et al, Evaluation of the risk of overheating and displacement of orthodontic devices in magnetic resonance imaging, Journal of Radiology, 88 (2007) 263-268.

[4.5] H. Bassen et al, MRI-induced heating of selected thin wire metallic implants – laboratory and computational studies – findings and new questions raised, Minimally Invasive Therapy and Allied Technologies, 15 (2006) 76-84.

[4.6] E. Mattei et al, MRI induced heating of pacemaker leads: effect of temperature probe positioning and pacemaker placement on lead tip heating and local SAR, Annual International Conference of the IEEE Engineering in Medicine and Biology Society, 1 (2006) 1889-1892.

[4.7] J. Nyenhuis et al, MRI and implanted medical devices: basic interactions with an emphasis on heating, IEEE Transactions on Device and Materials Reliability, 5 (2005) 467-479.

[4.8] U. Nguyen et al, Numerical evaluation of heating of the human head due to magnetic resonance imaging, IEEE Transactions on Biomedical Engineering, 51 (2004) 1301-1309.

[4.9] W. Nitz et al, On the heating of linear conductive structures as guide wires and catheters in interventional MRI, Journal of Magnetic Resonance Imaging, 13 (2001) 105-114.

[4.10] M. Dempsey, B. Condon, D. Hadley, Investigation of the factors responsible for burns during MRI, Journal of Magnetic Resonance Imaging, 13 (2001) 627-631.

[4.11] F. Shellock, Radiofrequency energy-induced heating during MR procedures: a review, Journal of Magnetic Resonance Imaging, 12 (2000) 30-36.

[4.12] J. Nyenhuis et al, Heating near implanted medical devices by the MRI RF-magnetic field, Digests of the Intermag Conference, (1999) BQ-12.

[4.13] O. Anfinsen et al, Implantable cardioverter defibrillator dysfunction during and after magnetic resonance imaging, Pacing and Clinical Electrophysiology, 25 (2002) 1400-1402.

[4.14] S. Pinski, R. Trohman, Interference in implanted cardiac devices, part II, Pacing and Clinical Electrophysiology, 25 (2002) 1496-1509.

[4.15] M. Niehus, J. Tebbenjohanns, Electromagnetic interference in patients with implanted pacemakers or cardioverter-defibrillators, Heart, 86 (2001) 246-248.

[4.16] S. Achenbach et al, Effects of MRI on cardiac pacemakers and electrodes, American Heart Journal, 134 (1997) 467-473.

[4.17] J. Weinmann, E. Sparrow, Heat flow from neuromodulation systems into surrounding media, Neuromodulation, 12 (2009).

[4.18] January 25, 2008. Meeting with Dr. Marie Clair Buckley
[4.19] S. Jiang et al, Effects of thermal properties and geometrical dimensions on skin burn injuries, Burns, 28 (2002) 713-717.
[4.20] M. Cohen, Measurement of the thermal properties of human skin. a review, Journal of Investigative Dermatology, 69 (1977) 333-338.
[4.21] F. Duck, Physical Properties of Tissue, A Comprehensive Reference Book, London: Academic Press, 1990.
[4.22] J. Valvano, J. Allen, H. Bowman, The simultaneous measurement of thermal conductivity, thermal diffusivity, and perfusion in small volumes of tissue, ASME 81-WA/HT-21, 1981.
[4.23] J. Johnson et al, Regulation of the cutaneous circulation, Federation Proceedings, 45 (1986) 2841-2850.
[4.24] T. Kobayashi et al, Improvement of deep body thermometer for man, Annals of Biomedical Engineering, 3 (1975) 181-188.
[4.25] D. Brajkovic, M. Ducharme, Confounding factors in the use of the zero-heat-flow method for non-invasive muscle temperature measurement, European Journal of Applied Physiology, 94 (2005) 386-391.
[4.26] R. Fox, A. Solman, A new technique for monitoring the deep body temperature in man from the intact skin surface, Journal of Physiology, 212 (1971) 8P-10P.
[4.27] R. Fox et al, A new method for monitoring deep body temperatures from the skin surface, Clinical Science, 44 (1973) 81-86.
[4.28] H. Pennes, Analysis of tissue and arterial blood temperatures in the resting human forearm, Journal of Applied Physiology, 85 (1948) 5-34.
[4.29] F. Henriques, A. Moritz. Studies of thermal injury I: the conduction of heat to and through the skin and the temperatures attained therein. A theoretical and experimental investigation, American Journal of Pathology, 23 (1947) 531-549.
[4.30] J. Weaver, A. Stoll, Mathematical model of skin exposed to thermal radiation, Aerospace Medicine, (1969) 24-30.

Chapter 5:
Impact of the Use of New-Generation Neuromodulation Devices on Tissue Damage

5.0 Introduction

There are at least three critical interactions between implanted magnetically susceptible materials and externally applied magnetic fields. Two of these interactions are potentially dangerous while the third corresponds to a positive function. The first of the undesirable interactions occurs whenever an MRI device is operated in close proximity to therapeutic implants, leads, or other magnetically susceptible devices [5.1, 5.3]. The interaction between the external field and these devices creates both a force and a torque which can displace the device from its original position. A second deleterious effect is the eddy currents generated in the device that give rise to Ohmic heating and potentially elevated temperatures [5.1, 5.2, 5.4, 5.5]. The interaction that performs a positive function is when the external field recharges a short-lived battery encased in an implant [5.6-5.10]. Although the latter interaction performs a positive function it, too, generates heat in both the implant and the antenna and may, consequently, lead to unsafe elevated temperatures.

The focus of this investigation is to provide definitive information on applications in which the external magnetic field recharges batteries in implants. In particular, the implants in question provide neuromodulation therapies. This issue has been addressed in the past [5.6-5.8]; however, since those earlier publications, all of the major neuromodulation systems have been redesigned and have different characteristics from their predecessors [5.9-5.10]. Since the issue of safety is of first importance in connection with implants that are sources of heat, it is imperative that all of the newly available neuromodulation system components be reappraised with regard to the temperature elevations they may cause in the body.

The major neuromodulation systems are those developed by Boston Scientific Corp. (Natick, MA); Medtronic, Inc. (Minneapolis, MN); and St. Jude Medical (Little Canada, MN). These systems are superficially similar, but differ in major details. In particular, the external source of the magnetic field (normally termed the antenna) are very different in their internal deployments of circuitry. Photographs of the components of all the neuromodulation systems in question are presented in Figure 5.1 (a) and (b), respectively for the implants and the antennae of the products. As is evident in the (a) part of the figure, each of the implants consists of a main body housing the appropriate circuitry and a polymeric adjunct which serves the purpose of a connector block. The thicknesses of the three units are approximately the same.

Restore Ultra (Medtronic) | Eon Mini (St. Jude Medical) | Precision Plus Boston Scientific

(a)

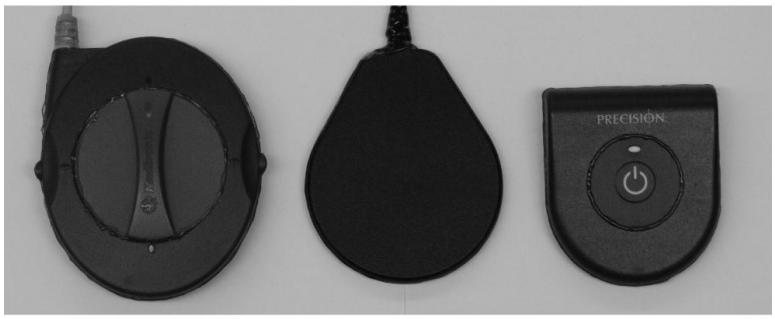

Restore Ultra (Medtronic) | Eon Mini (St. Jude Medical) | Precision Plus Boston Scientific

(b)

Figure 5.1: Photographs of (a) implants and (b) antennae that were evaluated.

The work to be described here makes use of an experimental facility which is a major improvement over that used in the experiments described in [5.6-5.7]. The new facility is capable of accommodating implants and antennae of different geometrical configurations

while providing detailed temperature information of high accuracy for all the investigated systems.

The experimental work is intended to provide highly accurate information about the rate at which heat is generated within the implant and, separately, within the antenna. These data will then be employed in conjunction with numerical simulation to predict the temperatures of the tissue layer between the implant and the skin surface as well as those of other tissue in the neighborhood of the implant.

5.1 The Experimental Facility

A pictorial side-view diagram of the experimental facility is displayed in Figure 5.2. As seen there, the facility is constructed from numerous components, prominent among which is a housing which is fabricated from extruded polystyrene. The housing has a recess to accommodate a calorimetric fluid whose function is to absorb heat that is generated within a test element situated within the fluid. The element may either be the neuromodulation implant or the antenna. Provision was built into the structure that enabled elements of different sizes and shapes to be accommodated in the recess. The element being evaluated was supported at a fixed distance from the floor of the recess by very thin pillars made of a low-conductivity foam. Situated below the main structure is an element which is the counterpart of that being evaluated in the calorimetric bath. Thus, if the implant was positioned in the calorimetric bath, the antenna was situated below, and vice versa. This setup enabled the magnetic interaction between the antenna and the implant to mimic with high fidelity that which is encountered in practice.

The distance between the top of the external element and the bottom of the internal element was fixed at 1 cm, reflecting medical practice. This separation distance consisted of a 4- mm-thick polystyrene wall and a 6- mm-water layer.

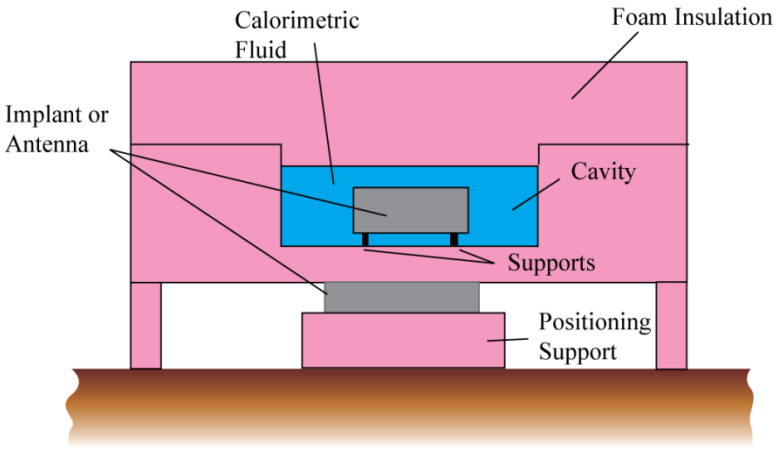

Figure 5.2: Schematic side view of the experimental facility.

The alignment of the internal and external elements was found to be a critical parameter with regard to the magnitude of the heat generation that was measured during the experiments. Great care was exercised to ensure near-perfect alignment. The need to obtain precise alignment was motivated by the requirement that all competing components be evaluated under identical conditions. When the alignment departed from perfection, it was found that the measured rates of heat generation were higher than those corresponding to perfect alignment.

Details of the inner structure of the test facility are presented in Figure 5.3. In diagram (a), the cavity which accommodates the calorimetric fluid is illustrated. Directly above the cavity in the exploded view is a square fence-like structure which serves as an anchor surface for thermocouples. Diagram (b) displays an embossment beneath the cap of the facility which serves as a thermocouple anchoring surface.

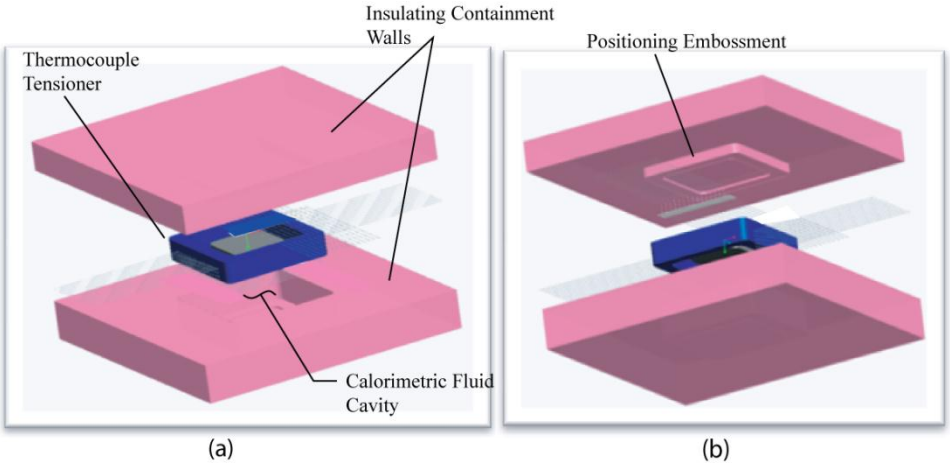

Figure 5.3: Exploded views of the facility exhibiting details of the inner structure.

In order to obtain detailed distributions of the water temperature within the cavity, a total of 30 thermocouples were deployed. The deployment was tailored so that each thermocouple was regarded as the center of a fluid volume. By this approach, a mass-weighted average of the thermocouple readings was conveniently obtained. Each thermocouple consisted of 0.127 mm (0.005 in.) diameter wires. The participating wires were chromel and constantan (type E). This wire pair was chosen because it generates the largest emf per degree temperature difference. A second attribute of this thermocouple pair is that its thermal conductivity is the lowest among any of the common thermocouple combinations.

Each thermocouple was a co-linear joining of the respective chromel and constantan wires. This configuration allowed for a precise positioning of each thermocouple junction and promoted a compactness of the thermocouple array as a whole.

Fifteen thermocouples were deployed in the calorimetric bath in a horizontal plane situated above the test specimen, and a second group of fifteen thermocouples was deployed in a horizontal plane below the specimen. The latter were anchored to the side walls of the bath with tape, and the former were anchored to the embossment.

The thermocouple voltages were read by a programmable data logger at a preset scan frequency. Since the experiments were run over a duration of at least one hour, the

temperature history was displayed by a computer to monitor progress. The computer also provided a tabular listing of the time wise variation of the output of each thermocouple. This information was subsequently post-processed as will be discussed shortly.

For each implant-antenna pair, three replicate data runs were performed. Additionally, for each product, three different implant-antenna pairs were utilized. Therefore, each product was represented by a total of eighteen data runs. That number of data runs includes separate runs for each component in the pair, either positioned within the calorimetric bath or beneath it.

5.2 Processing of the Experimental Data

With the goal of accounting for all of the thermal energy leaving the surface of the test element situated in the calorimetric fluid, it was deemed necessary to post-process the timewise temperature variations for each of the thermocouples situated in the fluid. For the post-processing, it was assumed that heat conduction was the only means of thermal transport occurring within the fluid and in the walls of the polystyrene which bounded the calorimetric bath. ANSYS finite element software was used to solve the heat conduction problem. The numerical solutions provided information about the rate of heat that was absorbed within the bounding walls of the bath. In general, the magnitude of that thermal energy was approximately 3% of that absorbed within the calorimetric fluid proper.

Representative experimental data is exhibited in Figure 5.4. The data display a consistent pattern at all thermocouple sites. There is an initial transient which gives way to a quasi-steady state represented by the straight parallel lines. The slopes of these lines provide the means by which the rate of heat transfer from the heat-generating element to the calorimetric fluid was deduced.

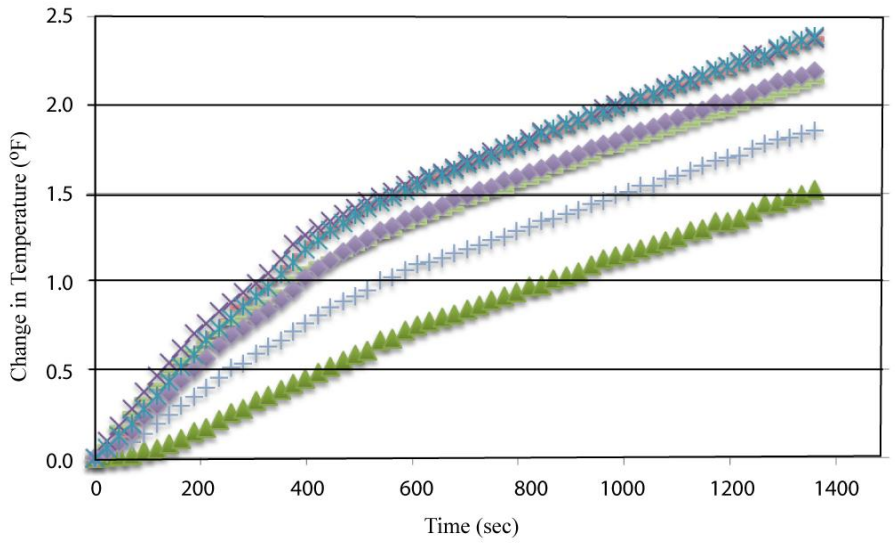

Figure 5.4: Representative experimental data.

The key features of the raw data from the experimental work are tabulated in the Appendix. A summary of those results is conveyed in Table 5.1. The table lists the rates of heat transfer that leave the surfaces of the respective devices, either the implant or the antenna. Inspection of the table reveals certain consistent trends. The heat flow from the implant is ordered with the Restore Ultra being the least-heating device, the Mini second least, and the Precision Plus the most-heating device. The corresponding rates of heat transfer are 0.26, 0.41, and 0.43 W. A similar ordering occurs for the antennae with the respective rates of heat transfer being 0.37, 0.55, and 0.70 W.

Table 5.1: Summary of calorimetry experiment results.

Device	**Heat Transfer Leaving Antenna**	**Heat Transfer Leaving Implant**
Restore Ultra	0.37 W	0.26 W
Eon Mini	0.55	0.41
Precision Plus	0.70	0.43

5.3 Numerical Simulations of Heat Flow in the Tissue Adjacent to the Implant and Antenna

5.3.1 Solution Domain and Material Properties:

Numerical simulations were performed with the goal of identifying the temperature ramifications of the heating rates that were extracted from the experimental data. The first step in the simulation was to select the domain in which the calculations are performed. That domain is displayed schematically in Figure 5.5. That figure shows a layered configuration, respectively skin, fat, fascia, and muscle. By virtue of the symmetry axis, it is evident that the simulation model is axisymmetric. The material properties of the respective layers and their thicknesses are listed in Table 5.2. The outer radius of the layered configuration was determined so that the lateral temperature gradients vanished there.

Table 5.2: Properties of the tissue layers.

Tissue	Layer thickness (mm)	Thermal conductivity (W/m-K)	Density (kg/m^3)	Specific heat (J/kg-K)	Median blood perfusion rate ($m^3/s/m^3$)	Metabolic heating (W/m^3)
Skin	2	0.45 [5.11]	1100 [5.13]	3500 [5.11]	0.0018 [5.15]	1300 [5.17]
Fat	30	0.2 [5.12]	960 [5.13]	2500 [5.16]	0.000425 [5.18]	250 [5.17]
Fascia	1	0.23 [5.13]	1000 [5.13]	3900 [5.13]	0.000425 [5.18]	250 [5.17]
Muscle	25	0.5 [5.14]	1040 [5.13]	3600 [5.16]	0.0005 [5.19]	500 [5.17]

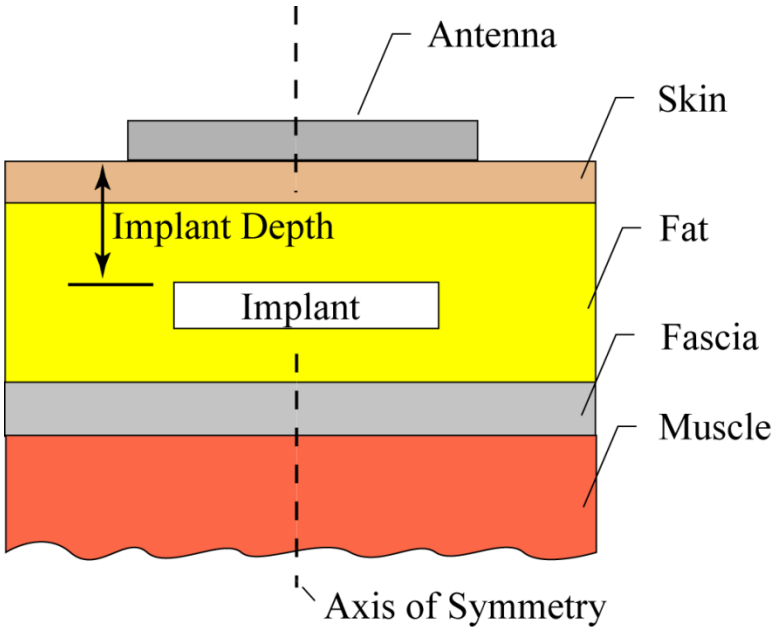

Figure 5.5: Schematic diagram of the system to be investigated, showing the four tissue layers, the skin-surface-mounted antenna, and the implant.

5.3.2 Governing Equations:

Many mathematical models have been proposed to describe bioheat transfer in living tissue [5.20-5.21]. Although many refinements have been made in the original Pennes model [5.22], those refinements are difficult to implement because the requisite material properties and geometrical configurations are either unknown or are not universal. The Pennes model requires only a single parameter, the blood perfusion rate ω. Values of this quantity are widely available but are often contradictory. However, it is possible to achieve a workable consensus. The values of the perfusion rates listed in Table 5.2 represent such a consensus.

The mathematical representation of the Pennes model is conveyed in Eq. (5.1), which is

$$(\rho c)_i \frac{\partial T_i}{\partial t} = k_i \frac{\partial^2 T_i}{\partial z^2} + \frac{k_i}{r}\frac{\partial}{\partial r}\left(r\frac{\partial T_i}{\partial r}\right) + (\rho c)_b \omega_i (T_a - T_i) + \dot{S}_{met,i}, \; i = 1\text{-}4 \tag{5.1}$$

The subscript *i* that is appended to certain quantities that appear in the equation identifies the layer to which the equation applies. It can be seen that the equation is appropriate for axisymmetric heat flow. The material properties of the layer includes the density, specific heat, and thermal conductivity, all related to tissue when subscripted with *i*. The

volumetric heat capacity $(\rho c)_b$ is that of blood. The blood perfusion rate, ω, is expressed in units of volumetric flow rate per unit volume of tissue ($m^3/s\text{-}m^3$).

A special feature of the numerical simulation is a precise modeling of the antenna which is positioned atop the layered configuration in Figure 5.5. An illustration of the complexity of the geometry of an antenna is provided in Figure 5.6. The table situated below the diagram indicates the presence of 10 individual components that were taken into account.

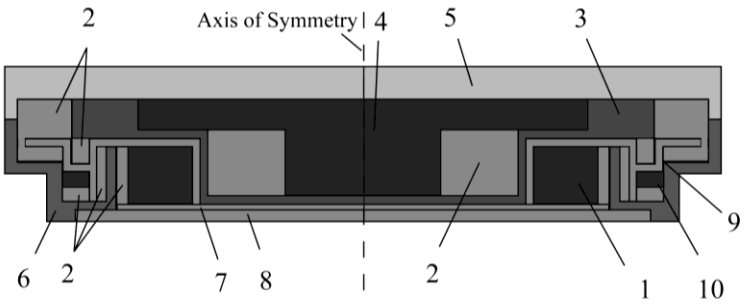

1 - Heating Coil	2 - Air Space
3 - Delrin	4 - Ferrite
5 - ABS and PC	6 - 10% Glass-Filled PC
7 - Thermal Pad	8 - Polypropylene
9 - Polyamide	10 - Passive Copper Coil

Figure 5.6: Vertical cut through an antenna illustrating the presence of numerous separate components.

The heat conduction in the antenna pictured in Figure 5.6 was modeled by making use of 10 interacting partial differential equations of the unsteady Poisson type. That is,

$$(\rho c)_j \frac{\partial T_j}{\partial t} = k_j \frac{\partial^2 T_j}{\partial z^2} + \frac{k_j}{r}\frac{\partial}{\partial r}\left(r\frac{\partial T_j}{\partial r}\right) + \dot{S}_j, \quad j = 1\text{-}10 \tag{5.2}$$

In this equation, the heat source, $\dot{S}$, was taken into account in those parts of the antenna where electric current is flowing.

5.3.3 Boundary and Continuity Conditions:

To complete the mathematical description of the model, it is necessary to specify the boundary and continuity conditions. The latter are relevant to the interfaces between contacting media. At each such interface, it is required that the temperature and the heat flux are continuous.

While the antenna was included in the model, the implant is not a part of the solution domain. At the interface between the surface of the implant and the surrounding fat layer, the heat flux was specified. Auxiliary measurements had been made to determine the distribution of the measured heat transfer rates between the upper and lower principle surfaces of the implant. The side walls of the implant were accorded a heat flux value equal to the average of those at the upper and lower surfaces.

At the very base of the solution domain, an insulated condition was assigned to provide an upper bound on tissue temperatures. It was found that the lower boundary was sufficiently far from the heated region that its presence did not affect the final results. The upper bounding surface of the solution domain was accorded one of two possible boundary conditions: (a) adiabatic or (b) convective heat transfer to the adjacent air environment. The adiabatic condition was intended to model the situation in which a patient is seated on an upholstered chair or lying on a bed. In the assignment of the heat transfer coefficients, account was taken of the insulating value of clothing, of the convection associated with buoyant motion, and radiation between the exposed surface and the surroundings.

5.4 Results and Discussion

5.4.1 Timewise Variations of the Maximum Tissue Temperatures:

The primary results of this study are the temperatures in the tissue adjacent to both the implant and the antenna. These results were obtained from the numerical simulations and are presented in Figures 5.7 and 5.8, respectively for the two boundary conditions of convective and radiative heat transfer to a 20 ^{o}C environment (Figure 5.7) and adiabatic (Figure 5.8).

An overview of these figures indicates a variety of trends, one of which is an oscillatory behavior. This behavior is attributed to the control system that governs the transfer of magnetic energy from the antenna to the implant. The most dramatic oscillations are those displayed for the Precision Plus device. A sensor which sends temperature information to the control circuit is situated near the interface of the antenna and the skin. The actual sensor is adhered to the inner wall of the antenna, coincident with the geometric center of the antenna. When that temperature exceeds a preset value, the magnetic field is suppressed and heating ceases. This action results in the cooling of both the antenna and the implant, causing a decreasing temperature in the tissue. When the temperature drops to the lower setpoint, the magnetic field is re-energized and the temperature rises.

Oscillations are also in evidence for the Restore Ultra for the case of the insulated surface. In that situation, the onset of corrective action occurs 84 minutes following the initiation of the recharge. That delay may, in many cases, exceed the time that is required for the attainment of full charge. No oscillations are in evidence for the Restore Ultra when there is heat loss from the outer surface. The results for the Eon Mini do not display oscillatory behavior. This is because the setpoint for the initiation of corrective behavior is set at a value so high that that temperature was never achieved.

For those cases in which the control system imposes limitations on the recharging period of the implant's battery, the time to achieve full charge may be considerably extended. It would appear that this possibility is greatest for the Precision Plus.

Further inspection of Figure 5.7 reveals a clear ordering of the tissue temperatures that are achieved during the charging period. The temperatures corresponding to the use of the Restore Ultra are clearly the lowest among those for the investigated devices. The other devices, the Eon Mini and the Precision Plus, achieve approximately the same maximum temperatures.

Attention may be directed to the horizontal reference line in orange color. That line, which corresponds to a temperature of 39°C, is an industry safety standard for active implantable medical devices. That temperature is regarded as the maximum allowable temperature for implantable devices [5.23]. With regard to that standard, it appears that only the Restore Ultra meets it. Another standard relates to the temperature at the interface between the antenna and the skin surface. That standard, shown by the green line in the figure, declares that a temperature of 41°C at that location is safe [5.24].

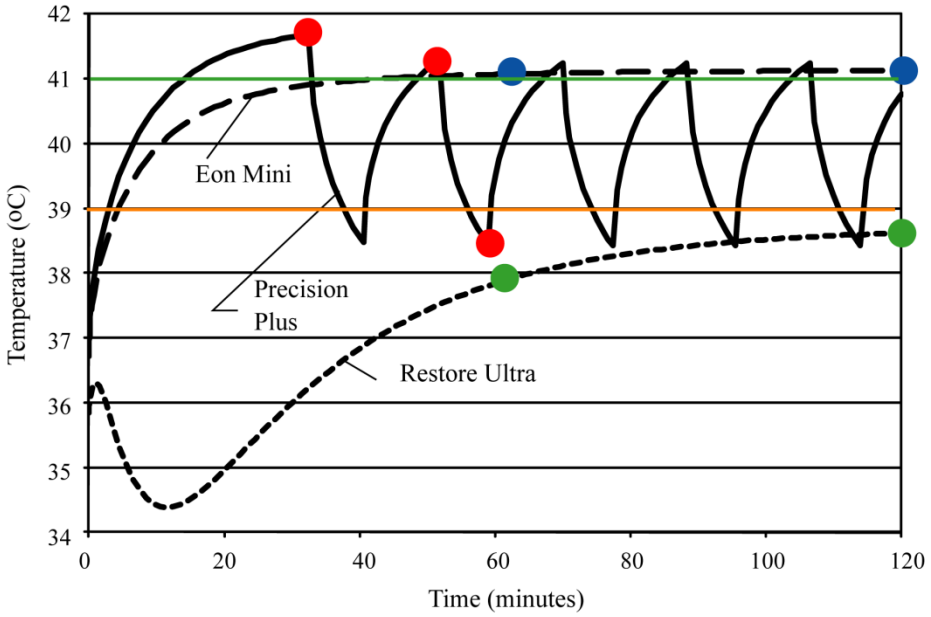

Figure 5.7: Timewise variations of the maximum tissue temperatures achieved during recharging for the three investigated neuromodulation devices in a convective environment. The colored dots indicate conditions for which temperature maps will be displayed in later diagrams.

Focus will now be directed to the results for a neuromodulation device operating in an adiabatic environment. Those results, displayed in Figure 5.8, show trends similar to those of the preceding figure, but there are very significant differences in detail. It might have been expected that in the presence of an adiabatic surface, all of the tissue temperatures would experience elevations compared with the results of Figure 5.7. From the results of Figure 5.8, those expectations were fulfilled for the Eon Mini and Restore Ultra devices. The reason why this trend was not followed for the Precision Plus is that

its control system was forced to initiate action more frequently compared to its operation in the convective environment.

The observed timewise behavior of the temperature results for the Eon Mini and the Precision Plus devices are independent of whether operation occurred in either a convective environment or an adiabatic environment. On the other hand, in the case of the Restore Ultra, the higher temperatures encountered in the presence of the adiabatic environment activated the control system, resulting in oscillations which were not in evidence in the convective environment. With regard to the 39°C standard, it is seen that all of the devices surpassed this value. On the other hand, the Precision Plus and the Eon Mini both exceeded the 41°C industry standard for skin-temperature elevations during the use of external antennas.

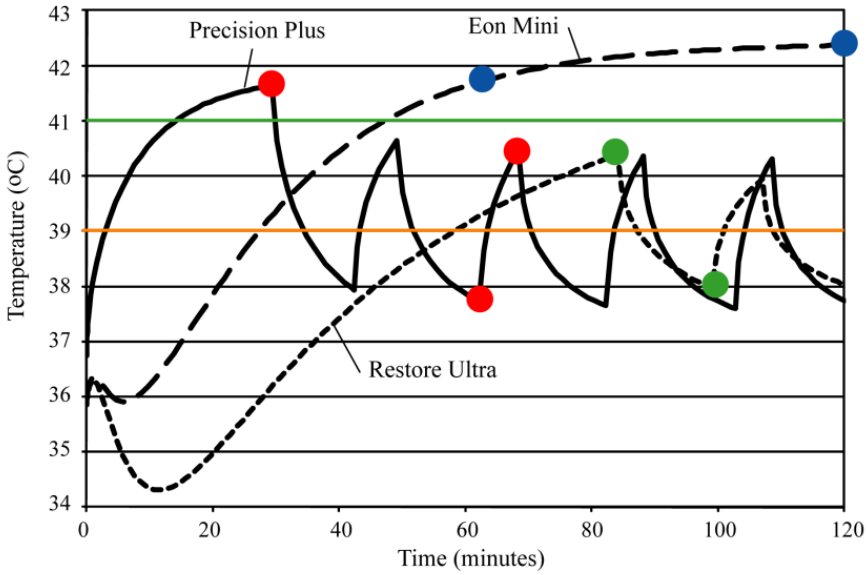

Figure 5.8. Timewise variations of the maximum tissue temperatures achieved during recharging for the three investigated neuromodulation devices in an adiabatic environment. The colored dots indicate conditions for which temperature maps will be displayed in later diagrams.

5.4.2 Tissue Temperature Maps:

Detailed temperature maps for a number of landmark instants of time are displayed in Figs. 5.9-5.11 for the Restore Ultra, the Eon Mini, and the Precision Plus, respectively. Each figure is subdivided into a number of sections, with each of the sections

corresponding to a specific instant of time. Those instants are related to various specific events in the timewise variations of temperature that are displayed in Figures 5.7 and 5.8. Appended to each figure is a color-legend in which the correlation of color and temperature is provided. The color-legends for all of the figures are the same. This selection of a common color legend was made to enable immediate comparisons of the temperature levels achieved by the various devices.

The (a) and (b) parts of Figure 5.9 correspond to instants of time equal to 60 and 120 minutes, respectively corresponding to the green circles in Figure 5.7. These figures indicate low tissue temperatures and no significant changes between the two instants. The (c) and (d) parts of the figure correspond to the green circles in Figure 5.8. Those instants correspond to first oscillatory maximum and the first oscillatory minimum. The trend of moderate temperatures that were in evidence in parts (a) and (b) continues to hold for parts (c) and (d), but with some difference in detail. The maximum, part (c), reflects a somewhat higher temperature while the minimum, part (d), exhibits a lower temperature.

Focus may next be directed to Figure 5.10. All of the time instants selected for exhibition of the temperature field are either 60 or 120 minutes. This selection is in recognition of the absence of oscillatory behavior which is occasioned by the high set-point value of the control circuit. The information displayed in the (a) and (b) parts relate to the blue circles in Figure 5.7 while parts (c) and (d) correspond to the blue circles in Figure 5.8. Inspection of the (a) and (b) parts, which correspond to convection heat transfer at the upper boundary, indicates that the higher temperatures are achieved just beneath the implant. These temperatures are slightly over 41^{o}C. The (c) and (d) parts provide information for the case of the adiabatic boundary and a clear increase in the temperature level is seen. It is noteworthy that the highest temperatures now occur within the antenna and those temperature levels are approximately 43^{o}C and 45^{o}C. On the other hand, the highest tissue temperatures are approximately 41.6^{o}C at 60 minutes and 42.4^{o}C at 120 minutes, both of which are in excess of the industry-standard specified temperatures of 39^{o}C and 41^{o}C.

The temperature field results for the Precision Plus are displayed in Figure 5.11 (a)-(f), and these results are keyed to the red circles of Figure 5.7 and 5.8. The reason that more diagrams are displayed for this case is that the oscillatory nature of the results require more resolution than was needed for the other devices. The information conveyed in (a)-(c) are related to red circles in Figure 5.7. Part (a) of Figure 5.11 relates to the highest temperature in the oscillatory train while the (b) part corresponds to what appears to be a recurring maximum; part (c) represents the recurring minimums. For these cases (a) and (b), the highest temperatures are seen to occur in the antenna while the maximum tissue temperatures are in the range 41.7^{o}C and 41.2^{o}C, respectively. At the minimum point, part (c), the maximum tissue temperature is 38.4^{o}C.

Finally, Figure 5.11 (d)-(f) display the results for the precision plus in the presence of the adiabatic boundary. As previously explained, the intuitive expectation of higher temperatures throughout is not necessarily fulfilled because of the action of the control system, as evidenced by the information conveyed in part (e). The maximum temperatures that correspond to the instants for the (a) and (f) parts of the figure are located in the antenna, respectively, about 47^{o}C and 45^{o}C. For these cases, the maximum tissue temperatures at 41.6^{o}C, 37.8^{o}C and 40.4^{o}C.

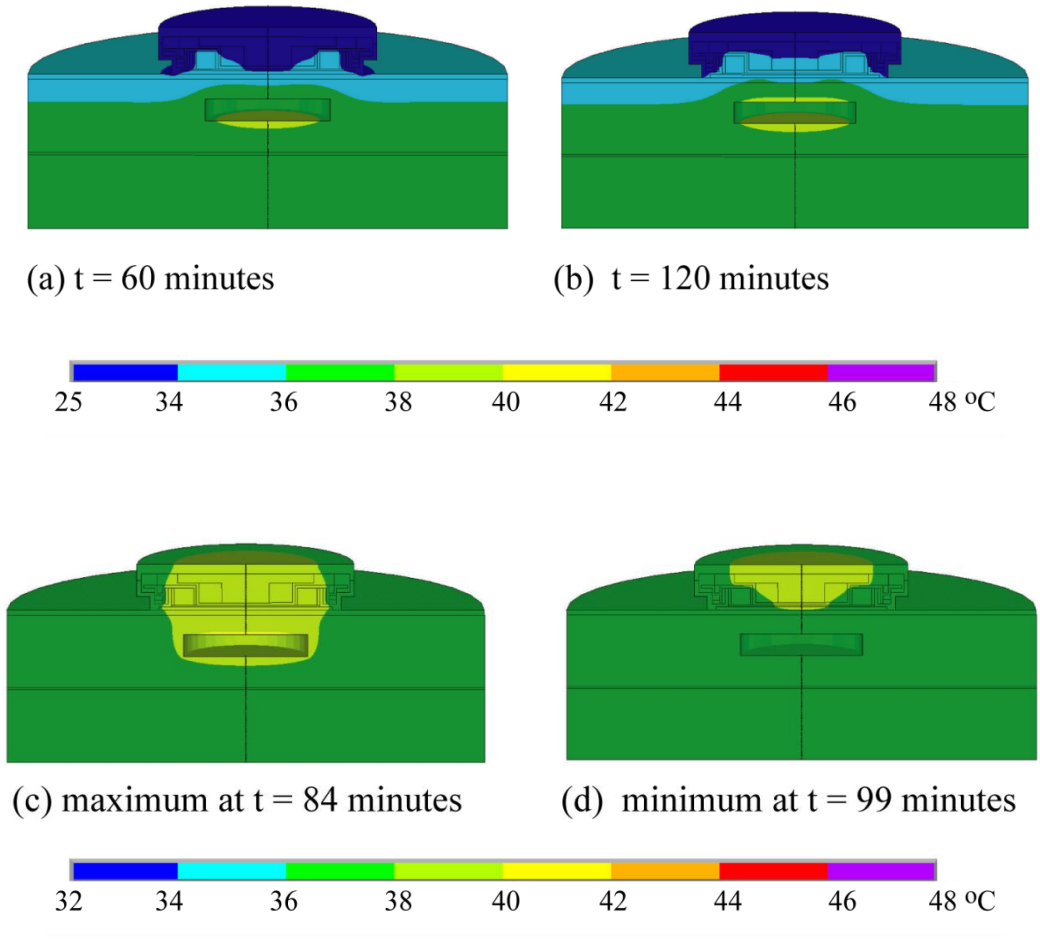

Figure 5.9: Temperature contour diagrams for neuromodulation by means of the Restore Ultra. Parts (a) and (b) are for convective boundary conditions. Parts (c) and (d) are for adiabatic conditions. Time instants refer to green circles in Figures 5.7 and 5.8.

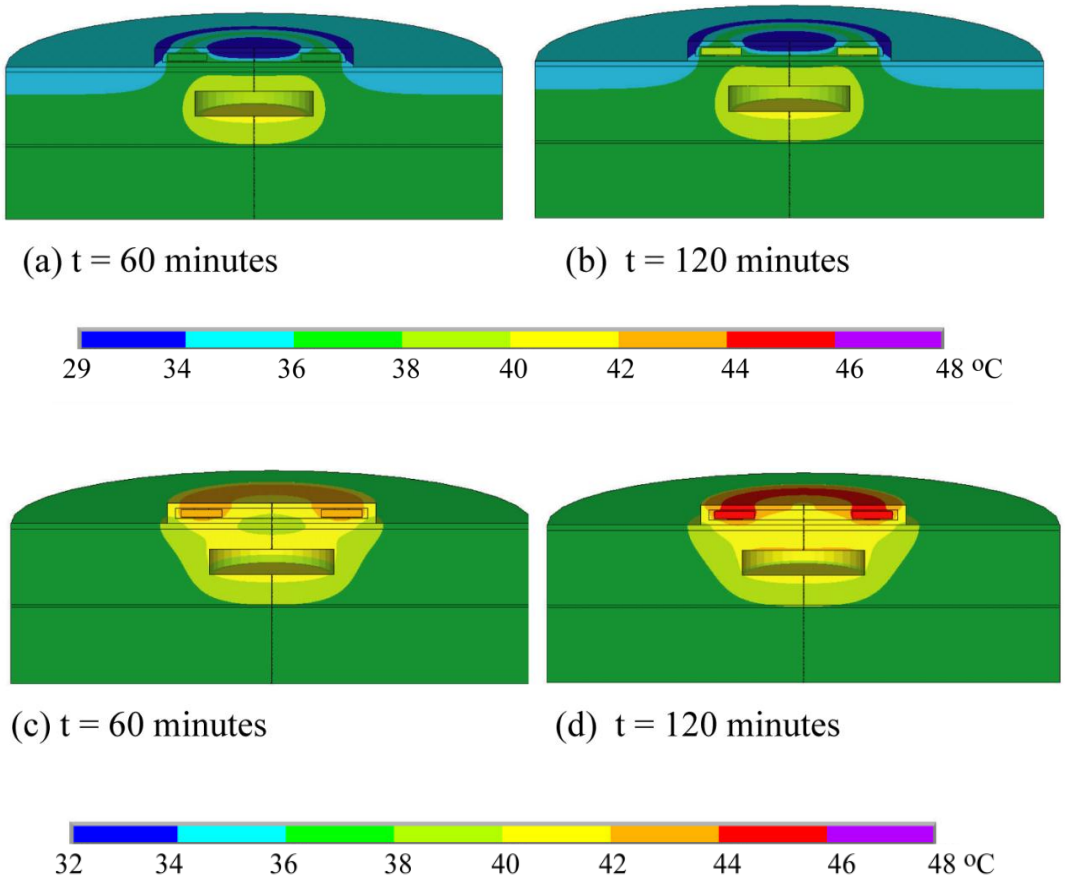

Figure 5.10: Temperature contour diagrams for neuromodulation by means of the Eon Mini. Parts (a) and (b) are for convective boundary conditions. Parts (c) and (d) are for adiabatic conditions. Time instants refer to blue circles in Figures 5.7 and 5.8.

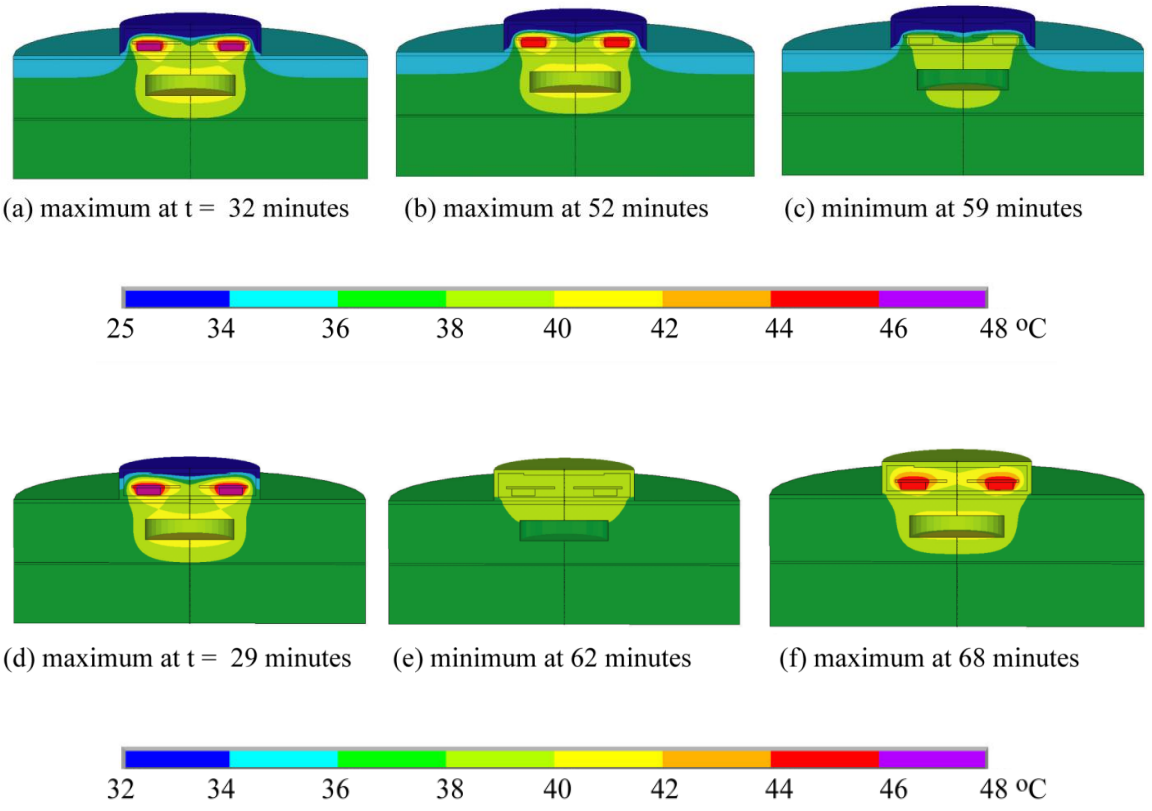

Figure 5.11: Temperature contour diagrams for neuromodulation by means of the Precision Plus. Parts (a)-(c) are for convective boundary conditions. Parts (d)-(f) are for adiabatic conditions. Time instants refer to red circles in Figures 5.7 and 5.8.

5.5 Concluding Remarks

The experimentation was focused on determining the rate at which the internally generated heat flowed from the implant and antenna into their respective surroundings. This information was obtained by a calorimetric investigation in which the components in question were immersed in a water bath which was heavily instrumented to enable the bath temperature to be determined as functions of both space and time. This information was numerically processed to extract the rates of heat flow. A number of replications and redundancies were built into the experimental procedure to provide sufficient statistical support for the accuracy of the results.

The experimental results were employed as input information to a numerical simulation of energy transfer in the tissue bed which extended from the skin into the deeper tissue below the implant. The simulation provided detailed timewise temperature distributions throughout the tissue bed. Special focus was directed to the location of the maximum temperature at each instant. These temperature maxima were displayed as a function of time and were appraised with regard to tissue thermal injury and to the mode of operation of the individual devices.

The timewise temperature variations were seen to depend upon the temperature control algorithms specific to the individual neuromodulation systems. Among the investigated devices, the Precision Plus was most responsive to its control system in that periodic fluctuations of the temperature occurred early in the recharge period and continued to occur for its duration. In the other extreme, the Eon Mini was totally unresponsive to its controls. The Restore Ultra displayed different responses depending on the nature of the environment in which it was used. In a convective and radiative environment, the control was not activated because the tissue temperatures never achieved values high enough to warrant its initiation. When used in an adiabatic environment, control was initiated only after a long duration of steady charging.

With regard to the magnitude of the tissue temperatures achieved during the recharging period, those corresponding to the use of the Restore Ultra were lowest, especially in the presence of a convective environment.

While in the work presented here, none of the three systems gave rise to tissue temperatures in excess of 43^{o}C (generally considered the temperature at which tissue injury commences), it was discovered that imprecise alignment of the antenna and implant led to notable increases in the heat generation. Since it is expected that in practice, perfect alignment of the devices will not be achieved, a study of the impact of alignment will be the focus of future investigations.

Appendix Chapter 5:

The tabulation of experimental results is subdivided into three sections, respectively conveying information for the Restore Ultra (part a), the Eon Mini (part b), and the Precision Plus (part c). The rates of heat flow are separately listed for the implants and the antennae. Each row of the table pertains to a given implant-antenna pair, and each entry is an average of three replicate runs. For both the implants and the antennae, three independent physical devices, designated as 1, 2, and 3, were employed during the course of the experiments. The grand average for each device appears in the last line in the table along with the standard deviation from the average.

Table 5.3: Rate of heat transfer leaving the surface of an implant or an antenna, standard deviation from the average in parenthesis.

(a) Restore Ultra

Device	Implant (W)	Antenna (W)
1	0.23	0.27
2	0.30	0.38
3	0.25	0.39
Average	0.26 (.035)	0.35(.064)

(b) (Eon Mini)

Device	Implant (W)	Antenna (W)
1	0.45	0.45
2	0.37	0.55
3	0.40	0.60
Average	0.41 (0.052)	0.53(0.075)

(c) (Precision Plus)

Device	Implant (W)	Antenna (W)
1	0.51	0.65
2	0.41	0.82
3	0.37	0.59
Average	0.43 (0.068)	0.69 (0.12)

References Chapter 5:

[5.1] J. Gimbel, J. Zarghami, C. Marchado, B. Wilkoff, Safe scanning, but frequent artifacts mimicking bradycardia and tachycardia during Magnetic Resonance Imaging (MRI) in patients with an Implantable Loop Recorder (ILR), Ann. Noninvasive Electrocardiology, 10 (2005) 404-408.

[5.2] F. Shellock, R. Crivelli, R. Venugopalan, Programmable infusion pump and catheter: Evaluation using 3-Tesla magnetic resonance imaging, Neuromodulation, 11 (2008) 163-170.

[5.3] M. Muhlenweg, G. Schaefers, S. Trattnig, Safety aspects in high-field magnetic resonance imaging, Radiologe, 48 (2008) 258-267.

[5.4] S. Pisa, G. Calcagnini, M. Cavagnaro, E. Piuzzi, E. Mattei, P. Bernardi, A study of the interaction between implanted pacemakers and the radio-frequency field produced by magnetic resonance imaging apparatus, IEEE Trans. Electromagnetic Compatibility, 50 (2008) 35-42.

[5.5] F. Shellock, L. Fischer, D. Fieno, Cardiac pacemakers and implantable cardioverter defibrillator: In vitro magnetic resonance imaging evaluation at 1.5-Tesla, J. Cardiovascular Magnetic Resonance, 9 (2007) 21-31.

[5.6] J. Weinmann and E. Sparrow, Heat flow from neuromodulation systems into surrounding media, Neuromodulation, 12 (2009) 114-121.

[5.7] R. Lovik, J. Abraham, E. Sparrow, Potential tissue damage from transcutaneous recharge of neuromodulation implants, Int. J. Heat Mass Transfer, 52 (2009) 3518-3524.

[5.8] J. Abraham, R. Lovik, E. Sparrow, Tissue temperature rises due to heat generation in neuromodulation implants, North American Neuromodulation Society 12th Annual Meeting, Las Vegas, NV, December 4-7, 2008.

[5.9] J. Abraham, E. Sparrow, R. Lovik, An investigation of tissue-temperature elevation caused by recharging of transcutaneous nueromodulation devices, 31st Annual International Conference of the IEEE Engineering in Medicine in Biology Society, Minneapolis, MN, September 2-7, 2009.

[5.10] J. Abraham, R. Lovik, D. Smith, E. Sparrow, K. Kelly, Heat generation measurements of revised neuromodeulation devices and calculations of tissue temperatures, North American Neuromodulation Society 13th Annual Meeting, Las Vegas, NV, December 4-6, 2009.

[5.11] S. Jiang, N. Ma, H. Li, X. Zhang, Effects of thermal properties and geometrical dimensions on skin burn injuries, Burns, 28 (2002) 713-717.

[5.12] M. Cohen, Measurement of the thermal properties of human skin. A review, J. Investigative Dermatology, 69 (1977) 333-338.

[5.13] F. Duck, Physical Properties of Tissue, A Comprehensive Reference Book, London: Academic Press, 1990.

[5.14] J. Valvano, J. Allen, H. Bowman, The simultaneous measurement of thermal conductivity, thermal diffusivity, and perfusion in small volumes of tissue, ASME 81-WA/HT-21, 1981.

[5.15] J. Johnson, G. Brengelmann, J. Hales, P. Vanhoutte, C. Wenger, Regulation of the cutaneous circulation, Federation Proceedings, 45 (1986) 2841-2850.

[5.16] T. Kobayash, T. Nemoto, A. Kamiya, T. Togawa, Improvement of deep body thermometer for man, Annals of Biomedical Engineering, 3 (1975) 181-188.

[5.17] D. Brajkovic and M. Ducharme, Confounding factors in the use of the zero-heat-flow method for non-invasive muscle temperature measurement, Euro. J. Applied Physiology, 94 (2005) 386-391.
[5.18] R. Fox A. Solman, A new technique for monitoring the deep body temperature in man from the intact skin surface, J. Physiology, 212 (1971) 8P-10P.
[5.19] R. Fox, A. Solomon, R. Isaacs, A. Fry, I. MacDonald, A new method for monitoring deep body temperatures from the skin surface, Clinical Science, 44 (1973) 81-86.
[5.20] Advances in Numerical Heat Transfer Vol. 3: Numerical Implementation of Bioheat Models and Equations, New York: Taylor and Francis, 2009.
[5.21] Handbook of Numerical Heat Transfer, 2nd Ed. Editors: Sparrow, Minkowycz, and Murthy, New York: John-Wiley & Sons, Inc., 2006.
[5.22] H. Pennes, Analysis of tissue and arterial blood temperatures in the resting human forearm, J. Applied Physiology, 85 (1948) 5-34.
[5.23] Active Implantable Medical Devices, BS EN 45501-1: 1998.
[5.24] Medical Electrical Equipment, BS EN 60601-1:2006

Chapter 6:
Impact of Misalignment of Antenna and Implant on Tissue Damage

6.0 Introduction

The use of implants to provide medical therapies has become a widespread procedure as a curative or a palliative approach. The first contemporary use of implants can be traced to the pacemaker. More recently, other functional needs have been fulfilled by implants of various types. The type of implant that is the focus of the present research serves as a neuromodulation device. Such a device sends electrical signals to the nervous system in order to moderate malfunctions such as chronic back pain.

Historically, neuromodulation implants were powered by non-rechargeable power sources. Surgical replacement of the implant is required when the battery becomes depleted. Within the past decade, rechargeable power sources have been introduced into neuromodulation. This new technology has provided the ability to significantly reduce implant size and has extended the useful life of the therapeutic device. The recharging of the implant's battery is achieved by the use of a magnetic field, which links the source of the field (situated on the surface of the skin) to the implant. The implant and the source are, respectively, the secondary and the primary of a transformer. The primary, often termed the *antenna*, is positioned on the surface of the skin with the implant situated approximately one centimeter beneath the skin surface.

The eddy currents that are created on the surface of the implant due to the magnetic field generate heat. Also, the windings that are contained within the antenna generate heat as well. As a consequence, the tissue situated between the skin surface and the implant experiences heating on both sides. It also may be expected that the deep tissue beneath the implant will be heated. The presence of a heat source within human tissue evokes a concern for the establishment of temperatures that are potentially unsafe.

Ideally, the primary and secondary of the transformer are lined up so that the magnetic lines of force are properly focused. Neuromodulation device rates of heat dispersion during recharging have been measured and their resulting effects on tissue temperature rise have been reported for this idealized aligned case [6.1]. However, the alignment of these components is normally the responsibility of the patient who is receiving the therapy. Patient information suggests that misalignment of the two components can give rise to higher rates of heat generation than is encountered in the aligned state. The concomitant temperature increases in the tissue that is in the neighborhood of the implant and the antenna may give rise to potential injury. The focus of the work to be reported here is a synergistic effort involving experimentation and numerical simulation, the ultimate goal of which is to assess the possible thermal injury associated with the heightened tissue temperatures attained when recharging with the devices misaligned.

The specific goal of the experimental work is the determination of the respective rates at which heat flows from the implant and the antenna to their respective surroundings. These experimentally determined rates of heat dispersion are used as input to a simulation model of thermal transport in the dermal and sub-dermal tissue that is situated in the neighborhood of the implant and the antenna.

The numerical simulation requires recognition of the special features that accompany the misalignment of the implant and the antenna. This misalignment violates the attractive but simplistic model of axisymmetric heat flow. As a consequence, the thermal transport model must be spatially three-dimensional and time dependent. The result of greatest significance from the numerical simulation is the comparison of the tissue temperatures that occur in the presence and in the absence of misalignment.

Three different neuromodulation devices were evaluated during the course of this investigation corresponding to those which are most frequently employed in therapeutic practice. They are: the Medtronic Restore Ultra, the Boston Scientific Precision Plus, and the St. Jude Eon Mini. Photographs of these devices are exhibited in Figures 6.1 and 6.2. The first of these shows the respective implants for each of the three therapeutic products

noted in the preceding sentence, while the second displays the corresponding antennas. The specifics of the magnetic field windings in each of these devices are responsible for the individual device's response to misalignment. Since the implant is a sealed unit, no comparison could be made of the different winding arrangements of each of those investigated.

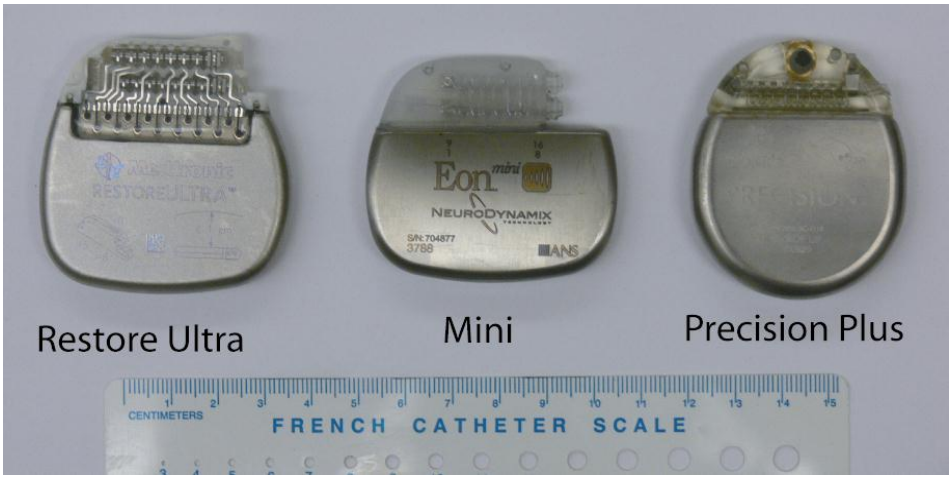

Figure 6.1: Photographs of the evaluated implants.

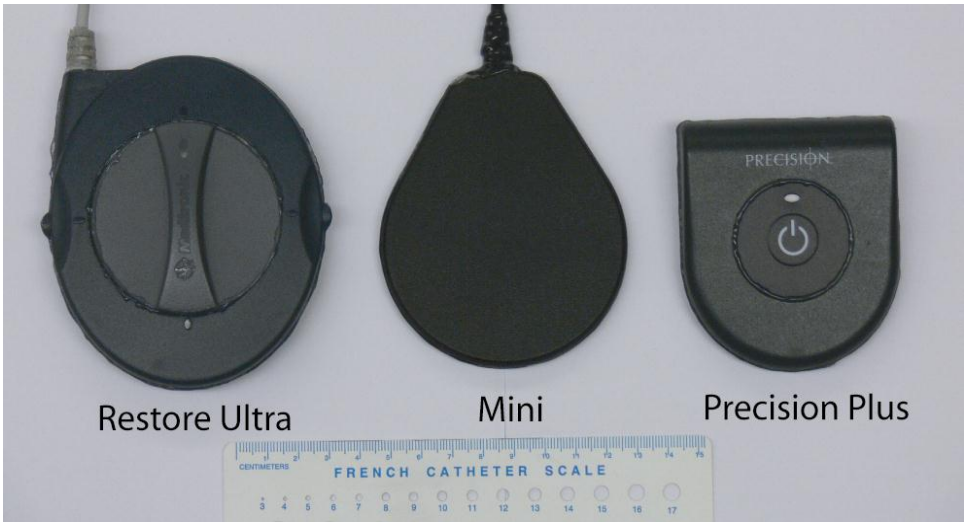

Figure 6.2: Photographs of the evaluated antennas.

6.1 The Experiments

6.1.1 Experimental Method:

The implementation of the experimental work is a two-step process. The first step is the design and fabrication of a suitable experimental facility. The next step is the collection

and processing of the experimental data to obtain the needed heat-generation information. With respect to the experimental facility, it was first necessary to decide on a method to measure heat generation. After due consideration, the calorimetric technique was selected. According to this method, the thermal energy produced by a heat source is measured in terms of the temperature rise of a heat-absorbing medium. The most convenient medium for this purpose is deionized water. This choice guided the design of the experimental facility. The details of that facility and its application will be presented in the succeeding section of this report.

6.1.2 Experimental Facility:

The experimental facility consists of an assemblage of several components, all of which were fabricated from extruded polystyrene. This material was chosen for four reasons: (a) lowest thermal conductivity of any rigid solid, (b) structural strength, (c) impermeable to water, and (d) excellent machinability. A major design requirement is that the facility be capable of being easily assembled and disassembled, so that it would always be identical in all data collection runs. Neither the polystyrene foam nor the deionized water alter the magnetic coupling of the implant and the antenna.

The experimental facility consists of a base which contains the calorimetric fluid in which one of the components of the neuromodulation device is immersed. This setup enables the heat generated and disseminated by the device component to be determined. The temperature of the calorimetric fluid is measured by an array of 30 fine-gauge thermocouples, half of which are systematically deployed beneath one of the device components and half of which are distributed above the component. It was found that this number of thermocouples was sufficiently large so that the average of the temperatures read by them was insensitive to the manner in which the temperatures were weighted. It is also believed, based qualitative experiments, that the thermocouples did not interfere with the magnetic field. To maintain the thermocouples in place, a means of maintaining tension is provided. Another feature is a fixture unique to each device component. This fixture is designed to hold the component in place so that the desired alignment is attained. The base is closed off by a lid. Another part of the experimental

facility is a structure which supports and positions the other component of the device. This component is exterior to the calorimetric bath. All portions of the experimental facility were fabricated from extruded polystyrene. The calorimeter base and the support structure for the exterior component are illustrated in Figure 6.3.

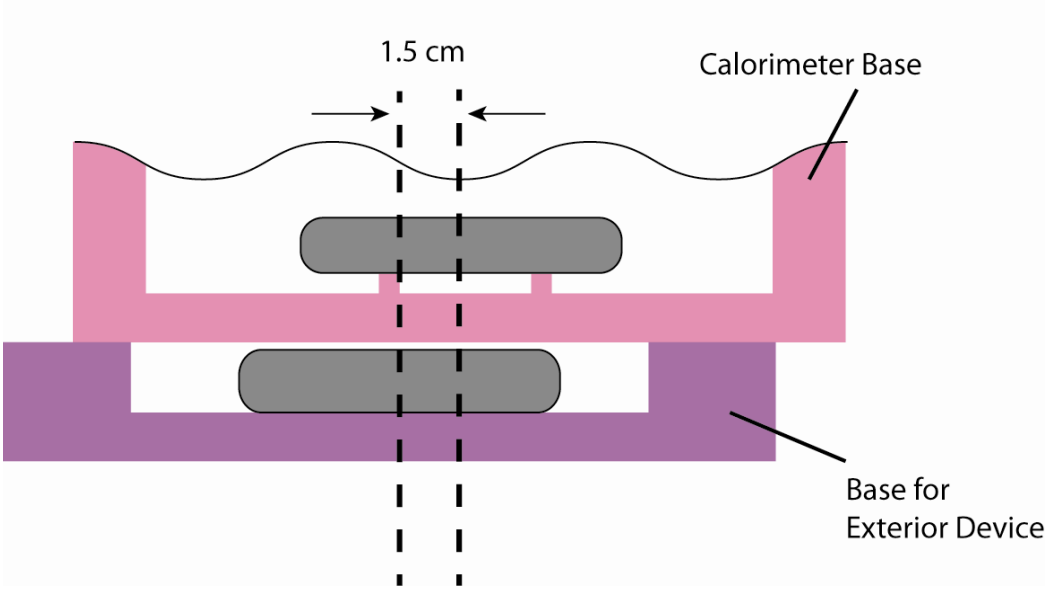

Figure 6.3: Schematic diagram of a generic neuromodulation device, with one component in the calorimetric bath and the other component situated beneath the bath container. The in-bath component and the exterior component are offset by 1.5cm.

The device component within the calorimetric bath may be either an implant or an antenna, and vice-versa for the component exterior to the bath. To properly evaluate the heat generation in the respective components, both must be positioned as they are in practice. The issue that is specifically addressed in this investigation is the effect of the offset pictured in Figure 6.3 on the temperature of the tissue in which the implant is situated. An offset distance of 1.5cm, a clinically realistic value, was selected for all of the experiments, as seen in Figure 6.3. The magnitude of this offset was found from preliminary experiments to cause a significant deviation of the heat generated from that of the aligned case, while remaining well within the recharging range of all investigated devices.

6.1.3 Instrumentation:

As described earlier, thermocouples were used to determine the instantaneous temperatures within the calorimetric bath. The number of temperature measurement sites provided a thorough assessment of the bath temperature distribution at any instant of time during the duration of the experiment. The thermocouples were fabricated from 0.005-in.-diameter chromel and constantan wire (Type E). The advantages of this thermocouple type are: (a) maximum emf per degree, (b) lowest thermal conductivity to minimize fin-like heat conduction, and (c) inert with respect to a humid environment.

During a data run, the time interval between successive readings of a given thermocouple was 30 seconds. The data were read by a multi-function data logger and transmitted to a personal computer for display and post-processing. In addition to the aforementioned thermocouple array that is situated within the calorimetric bath, a cluster of thermocouples was affixed to the lower surface of the calorimeter base. The function of this cluster was to indicate whether there was any heat flow from the exterior device through the base into the calorimetric fluid.

6.1.4 Experimental Procedure:

Prior to the setup of the data run, time is allowed to enable the experimental facility to come to thermal equilibrium with the surroundings. The preparation for a data run was initiated by the insertion of the test specimen in the calorimetric bath recess which, at the beginning of the run, was completely devoid of calorimetric fluid. The proper positioning of the test specimen was guaranteed by support pegs and a specimen holder. The calorimetric fluid, deionized water, was carefully introduced into the recess with the aid of a fine-tipped syringe. The lid was then put in place. Prior to its introduction into the recess, the deionized water had been stored in a closed container in the laboratory. Therefore, its temperature upon introduction into the recess was close to that of the rest of the facility. Notwithstanding this, at least three hours were allowed to enable total equilibration. This duration of the equilibrium period guaranteed that all parts of the experimental setup were at the same temperature. Subsequent to the equilibration period, the alignment was carefully checked to guarantee that the preselected misalignment,

1.5cm, was achieved. Data collection was started about five minutes prior to the initiation of voltage to the antenna, thereby establishing a baseline temperature. The duration of a data run was long enough to assure that quasi-steady operation was achieved.

6.2 Experimental Results

6.2.1 Data Post-Processing:

The most important information provided by each data run was the timewise variation of the temperature at each measurement site within the calorimetric bath. In general, after an initial transient, a quasi-steady state is established such that the increase of temperature with time takes a linear form at all of the sites. This state is encountered within 30 minutes of the initiation of operation of the system. As an example, the quasi-steady linear slopes for a particular data run are displayed in Figure 6.4. It can be shown from the theory of heat conduction that a heat conducting medium which is heated uniformly at one of its bounding surfaces and is adiabatic at its other bounding surfaces will, after an initial transient, display the same linear temperature increase at all points within the medium.

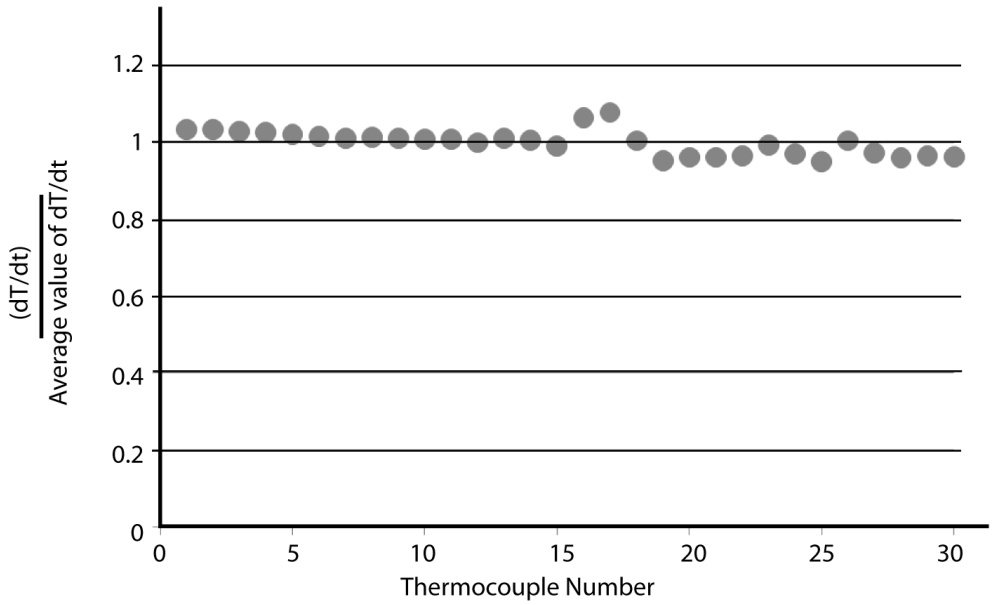

Figure 6.4: Quasi-steady temperature gradients at each of the measurement sites within the calorimetric bath.

The figure conveys the temperature gradient dT/dt at each of the measurement sites. The site-specific slopes are normalized by averaging the site-specific slopes over all of the 30 sites. This information is plotted as a function of the site identification number. Sites 1-15 are situated above the test specimen in the calorimetric bath, while sites 16-30 are below. Overall inspection of the figure reveals that the individual slopes do not deviate significantly from the average value. In particular, only two points show moderate deviations as great as approximately eight percent. It can be seen that the pattern of the slopes at sites above the test specimen is slightly different from that at the below sites. For one thing, the upper sites appear to have a generally uniform slope, while there is some scatter of the slopes at the lower sites. This finding can be attributed to the imbalance of the heights of the fluid-filled gaps above and below the specimen, the lower gap being about a third of the thickness of the upper gap. As a consequence, the thermocouples below the specimen may have been affected by the close proximity to both the specimen and the lower wall of the calorimetric recess.

Diagrams such as Figure 6.4 were prepared at the termination of each of the data runs, and the respective average values of dT/dt were calculated. When the average slope is multiplied by the mass and specific heat of the calorimetric fluid, the rate at which thermal energy is absorbed by the fluid is determined. To this value is added several heat losses from the fluid to its surroundings. These include the heat absorbed by the insulation, that conducted across the insulation by thermocouple leads, and that conducted through the insulation to the surrounding environment. These losses, determined by means of numerical simulations of the experiments, were found to be approximately five percent of the rate of energy absorption by the calorimetric fluid. This post-processing of the collected data yielded the rate at which energy leaves the surface of the test specimen and is transferred to its surroundings.

The foregoing determination of the rate at which energy leaves the surfaces of the respective components was regarded as a baseline for a sensitivity study that will be described shortly.

6.2.2 Rates at Which Heat is Transferred:

The results of the post-processing are conveyed in Tables 6.1, 6.2, and 6.3, respectfully for the Restore Ultra, Precision Plus, and Eon Mini. Each table is organized into two sections, with the leftmost section corresponding to the implant and the rightmost for the antenna. To assess repeatability of device heat generations, various combinations of individual implants and antennas, both corresponding to a given brand, were used in the experiments.

Each of the individual components is identified by a letter. For example, in the case of the Restore Ultra, two separate implants were tested and are respectfully designated as A and B while the two antennas are denoted by C and D.

Table 6.1: Restore Ultra heat transfer results.

Implant in Bath	Heat Transferred to Surroundings (W)	Antenna in Bath	Heat Transferred to Surroundings (W)
AC	0.3469	CA	0.4928
AD	0.3744	CB	0.3939
BC	0.3703	DA	0.4411
BD	0.3798	DB	0.5282
Average value	**0.3679**		**0.4640**

Implants = A, B; Antennas = C, D

Table 6.2: Precision Plus heat transfer results.

Implant in Bath	Heat Transferred to Surroundings (W)	Antenna in Bath	Heat Transferred to Surroundings (W)
EG	0.5990	GE	0.9802
EH	0.5955	GF	0.8793
FG	0.7195	HE	1.1406
FH	0.5511	HF	0.9178
Average value	**0.6163**		**0.9795**

Implants = E, F; Antennas = G, H

Table 6.3: Eon Mini heat transfer results.

Implant in Bath	Heat Transferred to Surroundings (W)	Antenna in Bath	Heat Transferred to Surroundings (W)
JL	0.7173	LJ	0.8702
JM	0.8449	LK	0.7318
KL	0.7770	MJ	1.0603
KM	1.0130	MK	0.6918
Average value	**0.8381**		**0.8385**

Implants = J, K; Antennas = L, M

An overall inspection of the three tables reveals considerable differences in the magnitudes of the rates at which heat is transferred from the respective components to their surroundings. In the case of the implants, the rate of transferred heat is a minimum for the Restore Ultra, followed by the Precision Plus and the Eon Mini, with respective values of 0.368, 0.616, and 0.838W. In judging these results, it may be noted that the lower the rate at which heat is transferred from the device, the safer is the device for a patient. Further observation of the tables shows that there is also considerable spread among the performance of the antennas. The heat transferred from the Restore Ultra is, once again, the lowest of the three. However, the highest rate of transfer is now that for the Precision Plus. The respective rates are 0.464, 0.980, and 0.839W for the Restore Ultra, Precision Plus, and Eon Mini.

As stated earlier, the overall goal of this investigation is to identify the effect of misalignment of the antenna and the implant. One definite impact of the misalignment is to increase the rate at which heat flows from the respective components into their surroundings. Comparisons between the rates of heat flow in the presence and in the absence of misalignment are exhibited in Table 6.4. The results for the aligned case are taken from [6.1].

Table 6.4: Comparison of rates of heat flows from the implants and the antennas to their respective surroundings for misalignment and perfect alignment.

Device	Average Rate of Heat Flow from the Implant with Misalignment	Percent Increase of Heat Flow over the Aligned Case	Average Rate of Heat flow from the Antenna with Misalignment	Percent Increase of Heat Flow over the Aligned Case
Restore Ultra	0.368 W	37.6%	0.464 W	15.7%
Precision Plus	0.616 W	40.6%	0.980 W	32.3%
Eon Mini	0.838 W	101.4%	0.839 W	47.5%

6.3 Numerical Simulation

6.3.1 Numerical Simulation Model:

The numerical simulation model was performed by means of the well established ANSYS finite element software. The solutions were carried out in the geometric space pictured in Figure 6.5. The (a) part of the figure is an isometric view of the solution domain showing the complexity of the geometry being considered. In particular, a simplifying assumption of axisymmetry is not appropriate due to the misalignment of the implant and the antenna. As a consequence, it is necessary to deal with a three-dimensional, time-dependent heat conduction problem.

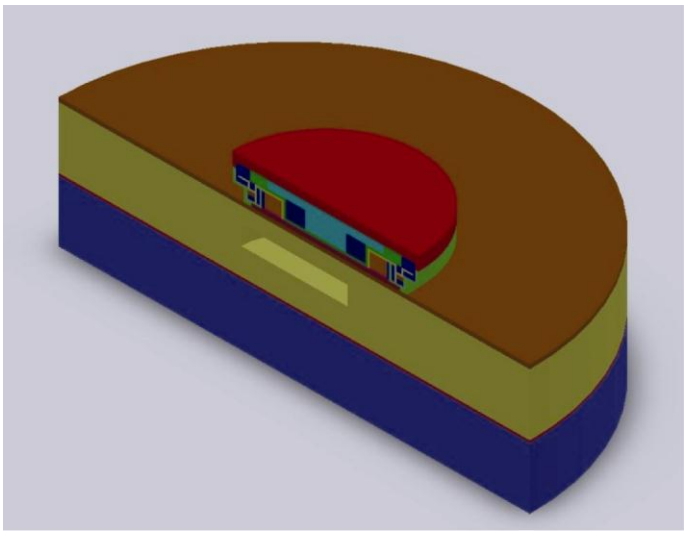

(a)

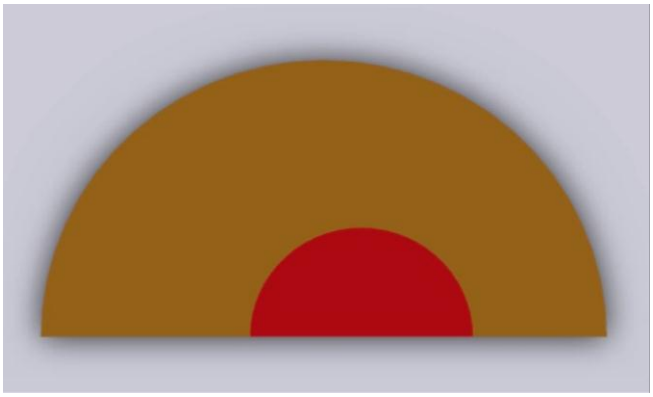

(b)

Figure 6.5: (a) Isometric view of the solution domain showing the implant, the antenna, and the multilayer tissue bed. (b) Top view of the solution domain.

A more detailed view of the solution domain is displayed in Figure 6.6 by a front view exposed by a cutting plane. That plane also defines the symmetric nature of the problem. Inspection of the figure reveals the presence of four individual tissue layers, respectively, skin, fat, fascia, and muscle. The implant is situated in the fat layer. The fat layer was purposefully made thick enough to fully encompass the implant as this was found to be the condition that causes the highest temperatures to be generated; additionally, it is within common human fat layer thickness. There are a few issues of particular note in the figure. The first is the one centimeter displacement between the bottom of the antenna and the upward-facing surface of the implant, this displacement was selected as it is a typical implant depth. The second is the offset between the axes of these

components. That offset, 1.5cm, was chosen because this was of sufficient magnitude to create a significant increase in device heat generation. Moreover, this distance is well within the recharging range of all the investigated devices. The interior of the implant is not detailed in the figure. This absence of detail stems from the reality that those details

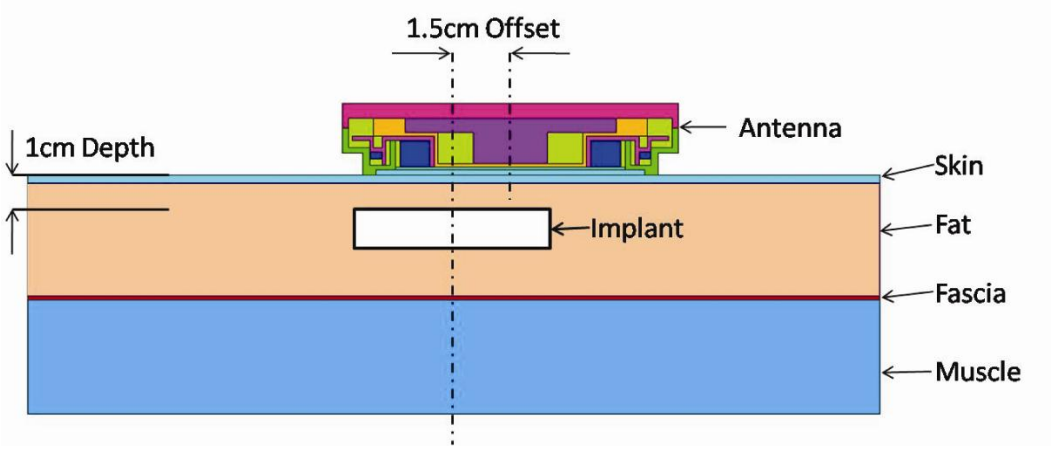

Figure 6.6: Numerical simulation model.

are not necessary for the simulation, since independent experiments were performed to establish the prorating of each implant's heat generation that passes through its respective surfaces. The other item that merits special attention is the complexity of the interior space of the antennas. That complexity is shown in greater detail in Figure 6.7. The pictured antenna is that of the Restore Ultra. Similar, but significantly different, features are found in the antennas of the Precision Plus and the Eon Mini. The details of the materials deployed within the antenna were taken into account in the numerical simulations.

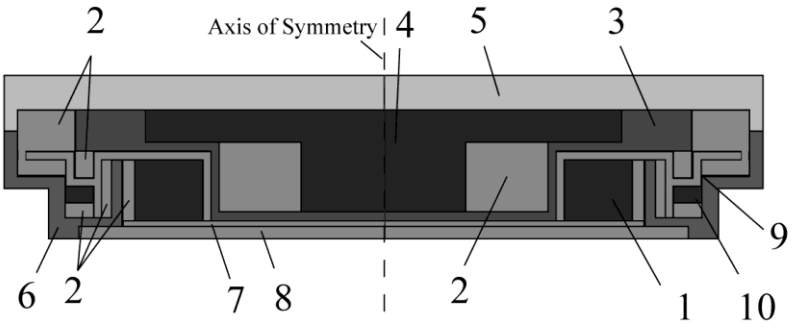

1 - Heating Coil
2 - Air Space
3 - Delrin
4 - Ferrite
5 - ABS and PC
6 - 10% Glass-Filled PC
7 - Thermal Pad
8 - Polypropylene
9 - Polyamide
10 - Passive Copper Coil

Figure 6.7: An example of the internal components of an antenna (Restore Ultra).

The two components of the neuromodulation device were respectively modeled as being axisymmetric. This characterization was motivated by prior successful axisymmetric implementations [6.1]. An additional benefit of the assumed axisymmetric geometry of the components is that a more regular numerical mesh could be created. The mesh employed in this study encompassed approximately 200 thousand nodes. This number of nodes were used as it provides mesh independent temperature results to within 0.1°C. As already stated, the overall solution domain is not axisymmetric.

6.3.2 Governing Equations:

The diversity of the media that make up the solution domain requires that specific forms of the heat equation be employed for each category of medium. For the tissue layers, thermal energy is transferred by both direct conduction and by blood perfusion. The equation that has been widely accepted for tissue heat transfer is that due to Pennes [6.2], which is

$$(\rho c)_t \frac{\partial T_t}{\partial t} = k_t \nabla^2 T_t + (\rho c)_b \omega (T_a - T_t) + \dot{Q}_{met} \tag{6.1}$$

In this equation, the subscripts *t* and *b* refer to tissue and blood, respectively. The quantity ω is the rate of blood perfusion in terms of volumetric flow rate per unit of volume of tissue, and T_a is the temperature of the arterial blood that passes through the tissue. $\dot{Q}_{met}$ is the metabolic heat generation. The participating thermophysical properties are the density ρ, the thermal conductivity k, and the specific heat c. This equation has to be separately applied at each of the four layers that constitute the tissue bed. As a consequence, the thermophysical properties, the perfusion rate, and the metabolic heat generation of each tissue layer have to be specified. This information is conveyed in Table 6.5. Note that the thermal conductivity k_t is a constant within each of the layers and, consequently, it is external to the differentiation operator ∇^2.

Table 6.5: Properties of the tissue layers.

Tissue	**Layer thickness (mm)**	**Thermal conductivity (W/m-K)**	**Density (kg/m^3)**
Skin	2	0.45 [6.3]	1100 [6.5]
Fat	30	0.2 [6.4]	960 [6.5]
Fascia	1	0.23 [6.5]	1000 [6.5]
Muscle	25	0.5 [6.6]	1040 [6.5]
Tissue	**Specific heat (J/kg-K)**	**Median blood perfusion rate (m^3/s/m^3)**	**Metabolic heating (W/m^3)**
Skin	3500 [6.3]	0.0018 [6.7]	1300 [6.9]
Fat	2500 [6.8]	0.000425 [6.10]	250 [6.9]
Fascia	3900 [6.5]	0.000425 [6.10]	250 [6.9]
Muscle	3600 [6.8]	0.0005 [6.11]	500 [6.9]

For the non-tissue media that are involved in the numerical simulation, there are two categories to be considered. In one of these, specifically the coils of the antenna, there is heat generation, while in the others, no heat generation occurs. The governing equations for these two types of media are, respectively,

$$(\rho c)\frac{\partial T}{\partial t} = k\nabla^2 \mathrm{T} + \dot{\mathrm{Q}}_{\mathrm{electric}} \tag{6.2}$$

$$(\rho c)\frac{\partial T}{\partial t} = k\nabla^2 T \tag{6.3}$$

The first of these applies to the heat generating media, and the second is for the non-generating media.

To complete the statement of the problem, boundary conditions have to be specified. By making reference to Figures 6.5 and 6.6, it can be seen that specification of boundary conditions is necessary on the bottommost surface of the muscle layer, on the cylindrical boundary of the assemblage of tissue layers, and at the surfaces of the antenna and the skin that are exposed to the environment. Since the implant is regarded as presenting a known heat source to the surrounding tissue, it is not included in the solution domain. Therefore, it is necessary to specify boundary conditions at the interfaces of the implant and the neighboring tissue. The specified boundary conditions are

(a) Bottom of the muscle layer: adiabatic
(b) Cylindrical boundary of the tissue layers: adiabatic
(c) Exposed surfaces of the antenna and the skin: (i) convective-radiative heat exchange with the environment, (ii) adiabatic
(d) Interfaces of implant and fat-layer tissue: prescribed heat flux at each interface segment
(e) Interfaces of contiguous tissue layers: continuity of temperature and heat flux
(f) Interface of the antenna and the skin surface: continuity of temperature and heat flux
(g) Interfaces of the contiguous volumes within the antenna: continuity of temperature and heat flux

Condition (a) serves as a closure of the space in which the solution is obtained. It is conservative in the sense that it leads to an upper bound for the temperatures in the solution space. Condition (c) encompasses two distinctly different physical situations. For the first of these conditions (i), $h = 6.5$ W/(m^2-°C), $T_{ambient} = 20$°C. This value of the heat transfer coefficient was calculated by means of heat transfer theory and, in particular, note was taken of the thermal resistance of clothing. The second of the conditions (ii), no heat transfer is permitted to occur at interface between the surrounding

environment and the exposed surfaces of the antenna and the skin. The heat flux values at the interfaces of the implant and tissue were obtained by taking the measured values of the wattage passing through the interface from Table 6.4, dividing by the surface area of the respective implant, and applying a proration factor obtained from separate measurements. The measured values of the heat dispersion from the antenna were used to obtain the $\dot{Q}_{electric}$ values in Eq. (6.2). Since the implant proper is not included in the solution space, its thermophysical properties are not relevant to the model.

The consideration of the two independent boundary conditions described in item (c) in the foregoing listing is motivated by corresponding physical situations. The (i) condition relates to situation where the location of the device is open to a room temperature ambient. On the other hand, the situation related to condition (ii) is that the location of the device is in contact with a bed or with upholstered furniture.

6.4 Numerical Simulation Results and Discussion

The focus of this work is to quantify the impact of misalignment of the implant and antenna on the maximum temperatures achieved in the tissue bed that is affected by these heat-generating components. The quantification is achieved by comparing the temperature for the misaligned case with a baseline which is defined as the aligned case. This information is conveyed in Tables 6.6(a) and (b) for the case in which the exposed surfaces of the antenna and skin exchange heat with the surroundings. The (a) and (b) parts of the table correspond respectively to the misaligned and aligned cases. Inspection of the tables confirms the expectation that misalignment does increase the maximum tissue temperatures. For the Restore Ultra, the effect of misalignment gives rise to temperature increases of between 0.4 and 1.5°C. The corresponding effect for the Precision Plus is 1.8°C. The increase of temperature rise for the Eon Mini is significantly higher, ranging from 3.9 to 4.2°C. Notwithstanding these increases, the Restore Ultra continues to give rise to the lowest tissue temperatures among the three devices investigated.

Table 6.6: (a) Maximum tissue temperatures reached for recharging in the convective-radiative environment with a misalignment of 1.5cm (temperatures in degrees Celsius).

Device	Maximum Temperature over the Time Period		
	0 – 30 min.	0 – 60 min.	0 – 120 min.
Restore Ultra	38.7	39.3	40.1
Precision Plus	43.5	43.5	43.5
Eon Mini	44.8	45.2	45.3

Table 6.6: (b) Maximum tissue temperatures reached for recharging in the convective-radiative environment with the devices aligned (temperatures in degrees Celsius).

Device	Maximum Temperature over the Time Period		
	0 – 30 min.	0 – 60 min.	0 – 120 min.
Restore Ultra	38.3	38.3	38.6
Precision Plus	41.7	41.7	41.7
Eon Mini	40.9	41.1	41.1

Tables 6.7(a) and (b) deal with the case in which the exposed surfaces of the antenna and skin are adiabatic. For the Restore Ultra and Precision Plus devices, the temperature increases due to misalignment are the same for the adiabatic case as was identified for the surface heat transfer case discussed with respect to Table 6.6. On the other hand, for the adiabatic case, the Eon Mini gives rise to higher temperature increases due to misalignment, ranging from 3.9 to 5.3°C. Once again, the lowest temperatures correspond to the Restore Ultra.

Table 6.7: (a) Maximum tissue temperatures reached for recharging without heat loss to the environment and with a 1.5cm misalignment (temperatures in degrees Celsius).

Device	Maximum Temperature over the Time Period		
	0 – 30 min.	0 – 60 min.	0 – 120 min.
Restore Ultra	38.8	40.8	41.6
Precision Plus	43.4	43.4	43.4
Eon Mini	44.8	46.9	47.7

Table 6.7: (b) Maximum tissue temperatures reached for recharging without heat loss to the environment and with the devices well aligned (temperatures in degrees Celsius).

Device	Maximum Temperature over the Time Period		
	0 – 30 min.	0 – 60 min.	0 – 120 min.
Restore Ultra	38.3	39.2	40.4
Precision Plus	41.6	41.6	41.6
Eon Mini	40.9	41.6	42.4

The variations of the hot-spot temperatures with time for the three devices and the two environmental thermal boundary conditions are conveyed in Figures 6.8 and 6.9. The location of the maximum tissue temperature varied with time. The *location of the hot spot* corresponds to that point in the tissue bed at which the highest of all tissue temperatures occurs. The first of these is for the case of heat exchange with a 20°C environment, and the second is for no heat transfer at the exposed surfaces, the adiabatic case. It can be seen from these figures that the presence or absence of a control system has a major effect on the timewise temperature variations. Both the Restore Ultra and the Precision Plus are equipped with control systems. These control systems consist of a temperature sensor in the external antenna which stops recharging when a preset temperature is reached; this is meant to prevent temperatures from reaching unsafe levels. In addition, the control system reinitiates recharging when the temperature sensor reduces in temperature to a lower preset temperature. A distinct sawtooth signature in the timewise variation of the hot-spot temperature can be seen in Figures 6.8 and 6.9, due to

the control system turning off or back on recharging. In contrast, the absence of an effective control system for the Eon Mini allows temperatures to rise monotonically and to exceed 47°C.

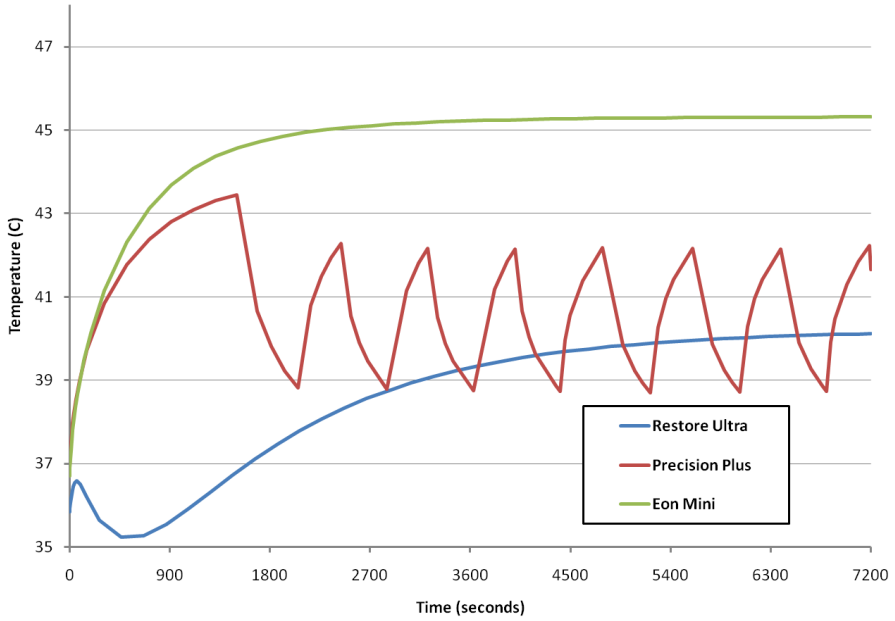

Figure 6.8: Hot-spot temperatures as a function of time for devices recharging at a 1.5cm misalignment in a 20°C room environment.

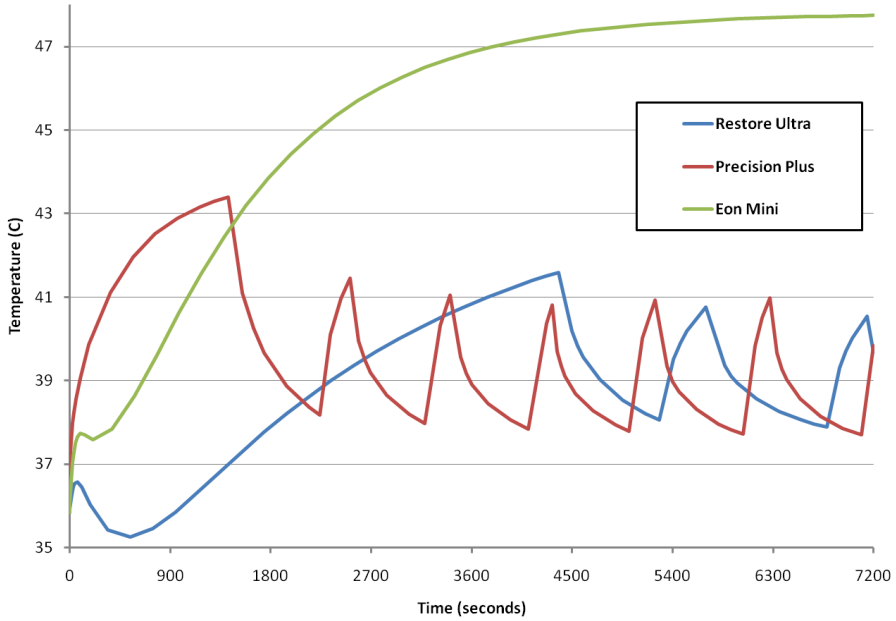

Figure 6. 9: Hot-spot temperature as a function of time for devices recharging at a 1.5cm misalignment without heat loss to the environment.

It is noteworthy to examine whether there exists the potential for tissue damage to occur when these devices are in use. There are a number of ways to predict tissue injury, the simplest is through the local tissue temperature. In the biothermal literature, 43°C is the commonly used threshold for onset of tissue damage [6.12-6.20]. When tissue temperatures are below 43°C, it is generally assumed that no injury is occurring. To assess the possibility of thermal tissue damage due to the temperatures attained during recharging of the neuromodulation devices, use was made of the Henriques-Moritz thermal injury integral [6.21], which is

$$\Omega(t) = A \int_0^t e^{-E_A/(RT)} d\tau \tag{6.4}$$

In this equation, A is the so-called pre-exponential constant, E_A is the activation energy, R is the universal gas constant, and τ is the variable of integration. The values of E_A and A are specific to each tissue layer. Values for skin were used for the evaluation of the integral, $E_A = 2.20*10^{124}$ s^{-1} and $A = 7.84*10^5$ J/mole [6.22]. The computed timewise temperatures for recharging at a 1.5cm offset were entered into the integrand and the integration was performed numerically. The cumulative thermal injury results can be seen in Table 6.8. Results are shown for device recharging durations of one and two hours. Separate results are listed for the two thermal boundary conditions, convective-radiative and adiabatic exposed surfaces, with the results for the latter delineated in parentheses.

Table 6.8: Cumulative thermal injury results of the maximum tissue temperature location for recharging the given device at a 1.5cm misalignment for the designated duration of time. Results are shown for recharging in a convective-radiative environment, and the results for the case of recharging in a well insulated environment are provided in parentheses.

Device	1 hour	2 hours
Restore Ultra	0.00018 (0.00062)	0.0012 (0.0019)
Precision Plus	0.0078 (0.0060)	0.011 (0.0065)
Eon Mini	0.088 (0.17)	0.26 (1.51)

The consensus is that cell necrosis occurs for values of Ω on the order of one. The results reported in Table 6.8 shows that neither the Restore Ultra or the Precision Plus device cause thermal tissue damage. This result is expected, as their temperature sensors keep the tissue temperature from rising to unsafe levels. However, the Eon Mini does not prevent high tissue temperatures from being attained. Moreover, the results of Table 6.8 exhibits that the Eon Mini device may be expected to cause thermal tissue damage for extended recharging durations. Specifically, for recharging in a 20ºC convective-radiative environment, a cumulative thermal injury value of 0.26 is reached at the maximum tissue temperature location for 2 hours of recharging. And, for recharging in a well insulated environment a cumulative thermal injury value of one is reached by 1.75 hours of recharging, which correlates to cell necrosis. Clearly, there is danger in recharging an Eon Mini neuromodulation device for an extended period of time.

6.5 Sensitivity Study

Temperature measurements made by means of a cluster of thermocouples attached to the lower surface of the calorimeter base indicated that heat was transferred from the exterior component to the calorimetric fluid. The measurements indicated that these rates of heat transfer were on the order of 15% or less of those determined by the post-processing method described in the body of the paper. This finding motivated a sensitivity study whose goal was to verify that the rank ordering of the respective devices was valid beyond any possible uncertainty. To this end, the heat transfer data that was used as input to the numerical simulation was decreased by 15% relative to that previously inputted. This approach was used simultaneously for both the heat transfer rates from the implant and the antenna to their respective surroundings.

The changes in the maximum tissue temperatures that resulted from the use of the decreased heat transfer inputs are conveyed in Table 6.9.

Table 6.9: (a) Decreases in maximum tissue temperature resulting from the sensitivity study with respect to those of Table 6.6(a) (convective-radiative environment with devices misaligned) (temperatures in degrees Celsius).

Device	Decrease in the Maximum Tissue Temperature over the Time Period		
	0 – 30 min.	0 – 60 min.	0 – 120 min.
Restore Ultra	0.2	0.7	0.8
Precision Plus	0.8	0.8	0.8
Eon Mini	1.1	1.2	1.2

Table 6.9: (b) Decrease in maximum tissue temperature resulting from the sensitivity study with respect to those of Table 6.7(a) (no heat loss to the environment and devices misaligned) (temperatures in degrees Celsius).

Device	Decrease in the Maximum Tissue Temperature over the Time Period		
	0 – 30 min.	0 – 60 min.	0 – 120 min.
Restore Ultra	0.2	0.8	0.8
Precision Plus	0.8	0.8	0.8
Eon Mini	1.1	1.5	1.5

Inspection of these tables reveals that the decreases in the maximum tissue temperature corresponding to 15% reductions in both the heat transfer from the antenna and the implant have only a moderate effect. In general, the decreases are of the order of 1˚C. These minor changes have no effect on the rank ordering of the devices as previously stated.

6.6 Conclusions

The outcomes of this investigation have led to several definitive conclusions, which are

(a) Misalignment of the implant and antenna of a neuromodulation device during recharging gives rise to higher tissue temperatures than are encountered when the components are aligned.

(b) For the case in which the exposed surfaces of the skin and the antenna exchange heat with the surroundings, the increases in tissue temperature, relative to those for the aligned case, range from 0.4 to 1.5°C for the Restore Ultra and from 3.9 to 4.2°C for the Eon Mini, while the temperature increases for the Precision Plus are approximately 1.8°C. When compared to the commonly used threshold for the onset of tissue damage, the Eon Mini exceeds 43°C within 15 minutes of the initiation of recharging and remains above 43°C for the remainder of the recharging period. The Precision Plus device exceeds 43°C for a brief duration, and the Restore Ultra remains well below 43°C.

(c) When the exposed surfaces are adiabatic, the temperature increases due to misalignment are about the same for the Restore Ultra and Precision Plus as they were for the case of heat exchange at the exposed surfaces. For the Eon Mini, misalignment in an adiabatic environment gives rise to larger increases in tissue temperature, ranging from 3.9 to 5.3°C. Moreover, these larger increases cause tissue temperatures to well exceed 43°C for an extended duration of time. Again, the Precision Plus exceeds 43°C for a brief duration, and the Restore Ultra remains below 43°C.

(d) For both of the investigated thermal boundary conditions, the Eon Mini gives rise to the highest tissue temperatures, exceeding 45°C in the heat exchange with the environment case and exceeding 47°C in a well insulated environment. The Precision Plus has a temperature sensor which maintains tissue temperatures below 44°C. The Restore Ultra has a temperature sensor which maintains tissue temperatures below 42°C.

(e) The cumulative thermal injury calculation results show that the Restore Ultra and Precision Plus devices are safe against causing thermal tissue damage to patients. However, for the Eon Mini there is danger of burning patients for recharging for extended time durations. In particular, for recharging in a well insulated environment cell necrosis has been predicted to occur within 1.75 hours of the initiation of recharging with a 1.5cm misalignment.

(f) A sensitivity study corresponding to 15% reductions in both the heat transfer from the antenna and implant did not change the rank ordering of the devices.

References Chapter 6:

[6.1] D. Smith, R. Lovik, E. Sparrow, J. Abraham, Human tissue temperatures achieved during recharging of new-generation neuromodulation devices, Int J Heat and Mass Transfer, 53 (2010) 3292-3299.

[6.2] H. Pennes, Analysis of tissue and arterial blood temperatures in the resting human forearm, J Appl Physiol, 85 (1948) 5-34.

[6.3] S. Jiang, N. Ma, H. Li, X. Zhang, Effects of thermal properties and geometrical dimensions on skin burn injuries, Burns, 28 (2002) 713-717.

[6.4] M. Cohen, Measurement of the thermal properties of human skin. A review, J Investigative Dermatology, 69 (1977) 333-338.

[6.5] F. Duck, Physical Properties of Tissue, A Comprehensive Reference Book. London: Academic Press, 1990.

[6.6] J. Valvano, J. Allen, H. Bowman, The simultaneous measurement of thermal conductivity, thermal diffusivity, and perfusion in small volumes of tissue, ASME 81-WA/HT-21, 1981.

[6.7] J. Johnson, G. Brengelmann, J. Hales, P. Vanhoutte, C. Wenger, Regulation of the cutaneous circulation, Federation Proceedings, 45 (1986) 2841-2850.

[6.8] T. Kobayash, T. Nemoto, A. Kamiya, T. Togawa, Improvement of deep body thermometer for man, Annals of Biomedical Engineering, 3 (1975) 181-188.

[6.9] D. Brajkovic, M. Ducharme, Confounding factors in the use of the zero-heat-flow method for non-invasive muscle temperature measurement, Euro J Applied Physiology, 94 (2005) 386-391.

[6.10] R. Fox, A. Solman, A new technique for monitoring the deep body temperature in man from the intact skin surface, J Physiology, 212 (1971) 8-10.

[6.11] R. Fox, A. Solomon, R. Isaacs, A. Fry, C. MacDonald, A new method for monitoring deep body temperatures from the skin surface, Clinical Science, 44 (1973) 81-86.

[6.12] M. Dewhirst, B. Viglianti, M. Lora-Michiels, M. Hanson, P. Hoopes, Basic principles of thermal dosimetry and thermal thresholds for tissue damage from hyperthermia, Int J Hyperthermia, 19 (2003) 267-294.

[6.13] Y. Feng, J. Oden, M. Rylander, A two-state cell damage model under hyperthermic conditions: theory and in vitro experiment, J Biomechanical Engineering, 130 (2008) paper 041016.

[6.14] W. Dewey, L. Hopwood, S. Sapareto, L. Gerweck, Cellular responses to combinations of hyperthermia and radiation, Radiology, 123 (1977) 463-474.

[6.15] M. Rylander, K. Diller, S. Wang, S. Aggarwal, Correlation of HSP70 expression and cell viability following thermal stimulation of bovine aortic endothelial cells, J Biomechanical Engineering, 127 (2005) 751-757.

[6.16] P. Hariharan, I. Chang, M. Myers, R. Banerjee, Radio-frequency ablation in a realistic reconstructed hepatic tissue, J Biomechanical Engineering, 129 (2007) 354-364.

[6.17] J. Lepock, Cellular effects of hyperthermia: relevance to the minimum dose for thermal damage, Int J Hyperthermia, 19 2003 252-266.

[6.18] R. Chopra, M. Bertnyk, M. Haider, M. Bronskill, Method for MRI-guided conformal thermal therapy of prostate with planar transurethral ultrasound heating applicators, Phys Med Biol, 50 (2005) 4957-4975.

[6.19] P. Bhowmick, J. Coad, S. Bhowmick, J. Pryor, T. Larson, J. Rosette, J. Bischof, In vitro assessment of the efficacy of thermal therapy in human benign prostatic hyperplasia, Int J Hyperthermia, 4 (2004) 421-439.
[6.20] X. Chen, G. Saidel, Mathematical modeling of thermal ablation in tissue surrounding a large vessel, J Biomechanical Engineering, 131 (2009) paper 011001.
[6.21] F. Henriques, A. Moritz, Studies of thermal injury I: the conduction of heat to and through the skin and the temperatures attained therein. A theoretical and experimental investigation, American J Pathology, 23 (1947) 531-549.
[6.22] J. Weaver, A. Stoll, Mathematical Model of Skin Exposed to Thermal Radiation. Aerospace Medicine, (1969) 24-30.

Chapter 7:
Concluding Remarks

The overarching theme of this thesis is the assessment of thermal and fluid flow processes which occur in certain organs of the human body. The work is, for the most part, a synergistic interaction between numerical modeling and experimentation. The specific foci of the research are the management of plaque that forms in human arteries and the thermal issues that relate to the implants that are heat generating.

With regard to plaque management, experimentation revealed that heating of blood (or its surrogates) might give rise to tissue necrosis. This fact motivated this segment of the thesis research. The work related to implants recognized that a class of implants is equipped with short-lived batteries that must be periodically recharged by means of an external magnetic field. The wiring incased in the implant serves as the secondary of a transformer and absorbs the magnetic lines of force which give rise to eddy currents. Those currents are heat producing and create a situation of potential overheating of tissue. A common theme of these components of the research is human safety. To the best knowledge of the author, there is no prior work in published literature that has dealt with this critical issue.

Fluid flow also was a major issue that was accounted for in the research. In particular, the pattern of fluid flow in arteries which are stenosed and subsequently debulked was investigated. A human cadaver was employed to facilitate this portion of the research. The outcome of this work gave rise to a metric by which the efficacy of the debulking operation could be judged. In connection with this work, ultrasound images of an artery prior to debulking and subsequent to debulking were taken. The reassembling of these images to create a solid structural model of the artery in its two states provided a real-world input to the numerical simulation.

A synopsis of the individual components of the research and its findings will now be set forth. A device used to successfully remove plaque from arteries operates as a rotating *in vivo* surface abrader. The underlying principle of this device is frictional interaction between the rotating abrader and the surface of the plaque. This interaction gives rise to heat generation. Although prior conjectures had proposed that local heating at the abrasion location could cause tissue damage, it was discovered that this is a fallacious hypothesis. Rather, the overwhelming heat source resulted from an upstream interaction of two of the components of the debulking device which gave rise to a preheating of the flowing fluid.

With this information from experiment, an encompassing numerical simulation model was constructed and implemented. The analysis predicted the spatial and temporal distribution of temperature throughout the artery wall and its contiguous tissue bed. This information was then used to assess the degree of possible tissue damage, the magnitude of which depends both on the temperature level and on the duration of the application of the temperature. The outcome of this assessment clearly indicated that no thermal tissue damage would occur, thereby leading to the firm conclusion that there are no safety hazards associated with the use of the investigated plaque debulking device.

The theme set forth in the preceding and penultimate paragraphs was implemented in connection with *in vitro* models. That theme was then generalized to *in vivo* models. In particular, a human cadaver was employed to implement this portion of the research. Fluid mechanic analysis was used to create and implement a metric to quantify the effectiveness of plaque removal (i.e., debulking) modalities in small arteries. The quantification is based on a three-dimensional, unsteady model of blood flow in complex tubular geometries which characterizes plaque-narrowed arteries. Blood flow unsteadiness is due to the heart-imposed temporal variations which occur during the cardiac cycle. The arterial geometries used for the analysis were determined by the reconstruction of ultrasonic images which were captured before and after debulking. Numerical simulation was used to implement the fluid mechanic model, and separate consideration is given to Newtonian and non-Newtonian constitutive equations. The

results of the analysis indicates that the removal of the plaque led to an increase in the rate of blood flow of approximately 2.5, both during the systole and diastole portions of the cardiac cycle. This increase corresponds to the application of the same time-varying, end-to-end pressure difference across the artery segments. The shear stress on the artery wall, a major determinant of the buildup of plaque, is found to be higher for a debulked artery than for a plaque-narrowed artery. This outcome is favorable in that the higher the wall shear, the lower the rate of plaque formation.

The second contribution to the overarching theme of this thesis deals with the issue of possible tissue necrosis associated with the presence of heat-generating implants. The magnetic-field-driven heat generation in neuromodulation systems consisting of implanted and skin-surface-mounted components gives rise to the potential of discomfort, cell damage, and possible necrosis. The skin-surface-mounted component, commonly termed the *antenna*, serves the function of the primary of a transformer, and the implant is the secondary. Heating occurs in both of these components during the recharging of a battery situated in the implant. Experimental data providing heat generation information was generalized and post-processed by a numerical simulation model. The key feature of the simulation model was the bio-heat transfer equation which yields both the spatial and temporal variations of the temperature field in tissue adjacent to both the implant and the antenna. It was found that during long-duration recharging periods, the temperature of the tissue rises in response to the heat generation. This information enabled the identification of the magnitude and location in the tissue of the hot-spot temperature. The temporal temperature variation at the hot spot was employed in conjunction with a tissue-damage integral to identify the possibility of cell damage and/or necrosis. It was found that two of the three investigated neuromodulation systems (Restore and Eon) did not give rise to temperature levels that may cause tissue damage. However, the third of the systems (Precision) caused temperatures of sufficient elevation so that for recharging periods on the order of two hours, necrosis was found to be likely in situations where heat transfer is suppressed at the surface of the skin.

The research studies summarized in the preceding paragraph were focused on industry devices that were current at the time. When these studies were concluded, a number of

redesigned and presumably enhanced neuromodulation devices became available. The thermal performance of these devices was a critical unknown and this criticality motivated new experiments and subsequent evaluation by means of numerical simulation. At this juncture, a totally new experimental facility was designed and fabricated. This facility embodied features which enabled results of much improved accuracy to be obtained. In addition to the enhanced accuracy, the new facility provided a flexibility which enabled a number of different geometrical configurations of both the implant and the antenna to be accommodated. The experiments utilizing the new facility measured the rates at which heat generated within the components flowed into their respective surroundings. This information was utilized as input information to the numerical simulations. The simulation model consisted of four tissue layers plus the skin-surface-mounted antenna. Two realistic external thermal environments were considered for the simulations. Both the experimentation and the simulations were performed for three leading neuromodulation devices: Precision Plus, Eon Mini, and Restore Ultra. In the presence of convective/radiative heat losses in a 20°C environment, the maximum tissue temperature during recharging never exceeded 39°C for the Restore Ultra, but exceeded 41°C for the Precision Plus and the Eon Mini. In an adiabatic environment, similar findings were observed; the temperatures associated with the Precision Plus and Eon Mini exceeded 41°C while the tissue temperatures near the Restore Ultra maintained values less than 41°C.

The safety issue with regard to implanted neuromodulation devices was assessed as reported in the preceding paragraphs for an ideal situation in which the axes of the antenna and the implant were perfectly aligned. In practice, there is high probability that this ideal alignment is not achieved, because the patient is required to carry out the alignment function rather than a medical professional. The alignment function is made difficult by the fact that the implanted device is beneath the skin and its location cannot be directly observed. The previous work performed here had indicated that misalignment could play a significant role in the heat generation of both the implant and the antenna. In particular, these preliminary experiments had demonstrated that the heat generation rates were increased by misalignment. In this light, the safety issue which had been

thoroughly investigated for the aligned case had to be reinvestigated for the misaligned case. The degree of misalignment was imposed taking account of the possible decoupling of the magnetic field of the antenna from the secondary coils in the implant. The Restore Ultra, Precision Plus, and Eon Mini were all subjected to a common degree of misalignment. Special fixtures were designed and fabricated to ensure that all of the devices experienced a common misalignment.

Measurements were made of the rate at which heat generated within the respective devices flowed to their environments. This information was used as input to a bioheat model with a modified geometry to account for the misalignment. The temporal and spatial temperature variations from the simulation model were employed to evaluate safety issues. It was found that misalignment increases tissue temperatures compared with those for the aligned case for all of the investigated devices. These increases ranged from 0.5 to 5.3°C.

The cumulative thermal injury calculation results show that the Restore Ultra and Precision Plus devices are safe with respect to causing thermal tissue damage to patients. However, for the Eon Mini, there is danger of burning patients for recharging for extended time durations. In particular, for recharging in a well-insulated environment cell necrosis has been predicted to occur within 1.75 hours from the initiation of recharging. A sensitivity study corresponding to 15% reductions in both the heat transfer from the antenna and implant did not change the rank ordering of the devices.

References:

[1.1] M. Cooperberg, J. Broering, P. Carroll, Time trends and local variation in primary treatment of localized prostate cancer, Journal of Clincal Oncology 28 (2010) 1117-1123.

[1.2] J. Wei, R. Dunn, H. Sandler, P. McLaughlin, J. Montie, M. Litwin, L. Nyquist, M. Sanda, Comprehensive Comparison of Health-Related Quality of Life After Contemporary Therapies for Localized Prostate Cancer, Journal of Clinical Oncology 20 (2002) 557-566.

[1.3] F. Burks, R. Santucci, Complicated urethroplasty: a guide for surgeons, Nature Reviews Urology 2010.

[1.4] A. Barqawi, E. Crawford, The current use and future trends of focal surgical therapy in the management of localized prostate cancer, Cancer Journal, 13 (2007) 313-317.

[1.5] R. Habash, R. Bansal, D. Krewski, H. Alhafid, Thermal therapy, Part III: Ablation techniques, Critical Reviews in Biomedical Engineering, 35 (2007) 37-121.

[1.6] S. Park, K. Kim, I. Oh, D. Shin, K. Park, M. Seo, J. Chung, K. Park, H. Lee, H. Kang, B. Koo, T. Youn, H. Kim, Comparison of plain balloon and cutting balloon angioplasty for the treatment of restenosis with drug-eluting stents vs bare metal stents, Circulation Journal 74 (2010) 1837-1845.

[1.7] L. Mauri, R. Bonan, B. Weiner, V. Legrand, J. Bassand, J. Popma, P. Niemyski, R. Kuntz, Cutting balloon angioplasty for the prevention of restenosis: Results of the Cutting Balloon Global Randomized Trial, American Journal of Cardiology, 90 (2002) 1079-1083.

[1.8] U. Baber, A. Kini, S. Sharma, Stenting of complex lesions: An overview, Nature Reviews Cardiology, 7 (2010) 485-496.

[1.9] J. Moses, M. Leon, J. Popma, P. Fitzgerald, D. Holmes, C. O'Shaughnessy, R. Caputo, R. Kuntz, Sirolimus-eluting stents versus standard stents in patients with stenosis in a native coronary artery, New England Journal of Medicine, 349 (2003) 1315-1323.

[1.10] D. Baldwin, J. Abbott, J. Trost, H. Vlachos, F. Selzer, R. Glaser, R. Wilensky, J. Slater, S. Doucet, S. Naidu, H. Aronow, D. Williams, Comparison of Drug-Eluting and Bare Metal Stents for Saphenous Vein Graft Lesions (from the National Heart, Lung, and Blood Institute Dynamic Registry), American Journal of Cardiology, 51 (2008) B23-B98.

[1.11] M. Adamian, A. Colombo, C. Briguori, T. Nishida, F. Marsico, C. Di Mario, R. Albiero, J. Moses, Cutting balloon angioplasty for the treatment of in-stent restenosis: A matched comparison with rotational atherectomy, additional stent implantation and balloon angioplasty, Journal of the American College of Cardiology, 38 (2001) 672-679.

[1.12] B. Vaquerizo, A. Serra, F. Miranda, J. Triano, G. Sierra, G. Delgado, A. Puentes, S. Mojal, J. Brugera, Aggressive plaque modification with rotational atherectomy and/or cutting balloon before drug-eluting stent implantation for the treatment of calcified coronary lesions, Journal of Interventional Cardiology 23 (2010) 240-248.

[1.13] I. Moussa, C. Di Mario, J. Moses, B. Reimers, L. Di Francesco, G. Martini, J. Tobis, A. Colombo, Coronary stenting after rotational atherectomy in calcified and complex lesions: Angiographic and clinical follow-up results, Circulation, 96 (1997) 128-136.
[1.14] R. Regine, O. Catalano, M. De Siero, G. Di Costanzo, A. Ragozzino, Endovascular treatment of femoropopliteal stenoses/occlusions with a SilverHawk directional atherectomy device: immediate results and 12-month follow-up, Radiologia Medica (in press).
[1.15] G. Shrikhande, J. McKinsey, Use and Abuse of Atherectomy: Where Should it be Used?, Seminars in Vascular Surgery, 21 (2008) 204-209.
[1.16] Y. Fu, H. Liu, W. Huang, S. Wang, Z. Liang, Steerable catheters in minimally invasive vascular surgery, International Journal of Medical Robotics and Computer Assisted Surgery, 5 (2009) 381-391.
[1.17] S. Greenberg, G. Murphy, J. Vender, Current use of the pulmonary artery catheter, Current Opinion in Critical Care, 15 (2009) 249-253.
[1.18] A. Gehani, M. Rees, Can rotational atherectomy cause thermal tissue damage? A study of the potential heating and thermal tissue effects of a rotational atherectomy device, CardioVascular and Interventional Radiology, 21 (1998) 481-486.
[1.19] R. Heuser, Treatment of lower extremity vascular disease: The Diamondback 360°™ Orbital Atherectomy System, Expert Review of Medical Devices 5 (2008) 279-286.
[1.20] S. Oh, A. Webb, T. Neuberger, B. Park, C. Collins, Experimental and numerical assessment of MRI-induced temperature change and SAR distributions in phantoms and in vivo, Magnetic Resonance in Medicine 63 (2010) 218-223.
[1.21] G. Calcagnini, M. Triventi, F. Censi, E. Mattei, P. Bartolini, W. Kainz, H. Bassen, In vitro investigation of pacemaker lead heating induced by magnetic resonance imaging: Role of implant geometry, Journal of Magnetic Resonance Imaging 28 (2008) 879-886.
[1.22] S. Mohsin, N. Sheikh, U. Saeed, MRI induced heating of deep brain stimulation leads: effect of the air-tissue interface, Progress in Electromagnetics Research, 83 (2008) 81-91.
[1.23] S. Park, R. Kamondetdacha, J. Nyenhuis, Calculation of MRI-induced heating of an implanted medical lead wire with an electric field transfer function, Journal of Magnetic Resonance Imaging 26 (2007) 1278-1285.
[1.24] K. Yassi, F. Ziane, E. Bardinet, M. Moinard, B. Veyret, J. Chateil, Evaluation of the risk of overheating and displacement of orthodontic devices in magnetic resonance imaging, Journal of Radiology 88 (2007) 263-268.
[1.25] H. Bassen, W. Kainz, G. Mendoza, T. Kellom, MRI-induced heating of selected thin wire metallic implants – laboratory and computational studies – findings and new questions raised, Minimally Invasive Therapy and Allied Technologies, 15 (2006) 76-84.
[1.26] E. Mattei, G. Calcagnini, M. Triventi, F. Censi, P. Bartolini, W. Kainz, H. Bassen, MRI induced heating of pacemaker leads: effect of temperature probe positioning and pacemaker placement on lead tip heating and local SAR, Annual International

Conference of the IEEE Engineering in Medicine and Biology Society 1 (2006) 1889-1892.
[1.27] J. Nyenhuis, P. Sung-Min, R. Kamondetdacha, A. Amjad, F. Shellock, A. Rezai, MRI and implanted medical devices: basic interactions with an emphasis on heating, IEEE Transactions on Device and Materials Reliability, 5 (2005) 467-479.
[1.28] U. Nguyen, J. Brown, I. Chang, J. Krycia, M. Mirotznik, Numerical evaluation of heating of the human head due to magnetic resonance imaging, IEEE Transactions on Biomedical Engineering 51 (2004) 1301-1309.
[1.29] W. Nitz, A. Oppelt, W. Renz, C. Manke, M. Lenhart, J. Link, On the heating of linear conductive structures as guide wires and catheters in interventional MRI, Journal of Magnetic Resonance Imaging 13 (2001) 105-114.
[1.30] M. Dempsey, B. Condon, D. Hadley, Investigation of the factors responsible for burns during MRI, Journal of Magnetic Resonance Imaging 13 (2001) 627-631.
[1.31] M. Nathan, Microbattery technologies for miniaturized implantable medical devices, Current Pharmaceutical Biotechnology 11 (2010) 404-410.
[1.32] T. Saraon, N. Gill-Saraon, A. Miller, R. Sinert, Pacemakers and Implantable Cardioverter Defibrillators. http://emedicine.medscape.com/article/780825-overview (Updated: Aug 30, 2010).
[1.33] H. Pennes, Analysis of tissue and arterial blood temperatures in the resting human forearm, Journal of Applied Physiology 1 (1948) 93-122.
[1.34] H. Arkin, L. Xu, K. Holmes, Recent developments in modeling heat transfer in blood perfused tissues, IEEE Transactions on Biomedical Engineering 41 (1994) 97-107.
[1.35] S. Weinbaum, L. Xu, L. Zhu, A. Ekpene, A New Fundamental Bioheat Equation for Muscle Tissue: Part I—Blood Perfusion Term, Journal of Biomechanical Engineering 119 (1997) 278-288.
[1.36] Y. Xuan, W. Roetzel, Bioheat Equation of the Human Thermal System, Chemical Engineering and Technology 20 (1997) 268-276.
[1.37] C. Charny, Mathematical models of bioheat transfer, Advances in Heat Transfer 22 (1992) 19-155.
[1.38] J. Chato, A view of the history of heat transfer in bioengineering, Advances in Heat Transfer 22 (1992) 1-18.
[1.39] H. Eugene, Pennes' 1948 paper revisited, Journal of Applied Physiology 85 (1998) 35-41.
[1.40] M. Chen, K. Holmes, Microvascular contributions in tissue heat transfer, Annals of the New York Academy of Sciences 335 (1980) 137-150.
[2.1] J. Valvano, J. Chitsabesan, Thermal Conductivity and Diffusivity of Arterial Wall and Atherosclerotic Plaque, Lasers Life Sciences 1 (1987) 219-229.
[2.2] F. Duck, Physical Properties of Tissue. London: Academic Press (1990) 9-42.
[2.3] H. Pennes, Analysis of tissue and arterial blood temperatures in the resting human forearm, *J. Appl. Physiol*. 85 (1948) 5-34.
[2.4] K. Diller, J. Valvano, J. Pearce, Bioheat Transfer. CRC Handbook of Thermal Engineering, Boca Raton: CRC Press, 2000.
[2.5] C. Keele, E. Neil, Applied Physiology, 12th ed., London: Oxford Press, (1971) 62.

[2.6] F. Henriques, A. Moritz, Studies of thermal injury I: the conduction of heat to and through the skin and the temperatures attained therein. A theoretical and experimental investigation, *Am. J. Pathol*, 23 (1947) 531-549.
[2.7] A. Han, J. Pearce, Kinetic Model for Thermal Damage in the Myocardium, In: Advances in Measuring Temperatures in Biomedicine; Thermal Tomography Techniques and Bioheat Transfer Models, New York: ASME, 1990.
[2.8] K. Diller, Modeling of Bioheat Transfer Processes at High and Low Temperatures, Advances in Heat Transfer, Bioengineering Heat Transfer, Boston: Academic Press, 22 (1992) 157-348.
[3.1] D. Ku, Blood flow in arteries, Ann. Rev. Fluid Mech. 29 (1997) 399-434.
[3.2] C. Taylor, T. Hughes, Z. Zarins, Finite element modeling of three dimensional pulsatile flow in the abdominal aorta: relevance to atherosclerosis, Ann. Biomed. Eng. 27 (2000) 975-987.
[3.3] P. Neofytou, D. Drikakis, Non-Newtonian flow instability in a channel with a sudden expansion, J. Non-Newtonian Fluid Mechanics 111 (2003), 127-150.
[3.4] S. O'Callaghan, M. Walsh, T. McGoughlin, Comparison of finite volume, finite element and theoretical predictions of blood flow through an idealized femoral artery, 2003 Summer Bioengineering Conference, June 25-29, 2003. Key Biscayne, Fl.
[3.5] J. LaDisa, I. Guler, L. Olson, D. Hetterick, J. Kersten, D. Warltier, P. Pagel, Three-dimensional computational fluid dynamics modeling of alterations in coronary wall shear stress produced by stent implantation, Ann. Biomed. Eng. 31 (2003) 972-980.
[3.6] M. Grigoni, C. Daniele, M. Umberto, C. Del Gaudio, G. D'Avenio, A. Balducci, and V. Barbaro, A mathematical description of blood spiral flow in vessels: application to a numerical study of flow in arterial bending, J. Biomech. Eng. 38 (2005) 1375-1386.
[3.7] F. Abraham, M. Behr, and M. Heinkenschloss, Shape optimization in steady blood flow: a numerical study of non-newtonian effects, Comp. Methods Biomech. 8 (2005) 127-137.
[3.8] Z. Ding, K. Wang, J. Li, and X. Cong, Flow field and oscillatory shear stress in a tuning-fork-shaped model of the average human carotid bifurcation, J. Biomech. Eng. 34 (2001) 1555-1562.
[3.9] A. Berhier, R. Bouzerar, and C. Legallais, Blood flow patters in an anatomically realistic coronary vessel: influence of three different reconstruction methods, J. Biomech. Eng. 35 (2002) 1347-1356.
[3.10] N. Shahcheraghi, H. Dwyer, A. Cheer, A. Barakat, and T. Rutaganira, Unsteady and three-dimensional simulation of blood flow in the human aortic arch, J. Biomech. Eng. 124 (2002) 378-386.
[3.11] M. Oshima, R. Torii, T. Kobayashi, N. Taniguchi, and K. Takagi, Finite element simulation of blood flow in the cerebral artery, Comp. Methods Appl. Mech. Eng. 191 (2001) 661-671.
[3.12] Q. Long, X. Xu, K. Ramnarine, and P. Hoskins, Numerical investigation of physiologically realistic pulsatile flow through stenosed arteries, J. Biomech. Eng. 34 (2001) 1229-1242.

[3.13] U. Krueger, J. Zanor, and H. Scholz, Computational fluid dynamics and vascular access, Artificial Organs, 26 (2002) 571-575.
[3.14] P. Marques, M. Oliviera, A. Franca, and M. Pinotti, Modeling and simulation of pulsatile blood flow with a physiologic wave pattern, Artificial Organs, 27 (2003), 478-485.
[3.15] I. Marshall, S. Zhao, P. Papathanasopoulou, P. Hoskins, and X. Xu, MRI and cfd studies of pulsatile flow in healthy and stenosed carotid bifurcation models, J. Biomech. Eng., 37 (2004) 679-687.
[3.16] J. Chen and X. Lu, Numerical investigation of the non-newtonian pulsatile blood flow in a bifurcation model with a non-planar branch, J. Biomech. Eng., 39 (2006) 818-832.
[3.17] F. Gijsen, F. van de Vosse, and J. Janssen, The influence of the non-newtonian properties of blood on the flow in large arteries: steady flow in a carotid bifurcation model, J. Biomech. Eng., 32 (1999) 601-608.
[3.18] Y. Cho and K. Kensey, Effects of the non-newtonian viscosity of blood on flows in a diseased arterial vessel. part 1: steady flows, Biorheology, 28 (1991) 241-261.
[3.19] B. Johnston, P. Johnston, S. Corney, and D. Kilpatrick, Non-Newtonian blood flow in human right coronary arteries: steady state simulations, J. Biomech. Eng., 37 (2004) 709-720.
[3.20] D. Tang, C. Yang, S. Kobayashi, and D. Ku, Steady flow and wall compression in stenotic arteries: a three-dimensional thick-wall model with fluid-wall interactions. J. Biomech. Eng., 123 (2001) 548-557.
[3.21] D. Tang, C. Yang, H. Walker, S. Kobayashi, and D. Ku, Simulating cyclic artery compression using a 3d unsteady model with fluid-structural interactions,Comp. and Struct., 80 (2002) 1651-1665.
[3.22] R. Bird, W. Steward, and E. Lightfoot, Transport Phenomena, John Wiley & Sons, New York, NY, 960.
[3.23] F. Walburn and D. Schneck, A constitutive Equation for Whole Human Blood, Biorheology, 13 (1976) 201-210.
[3.24] J. Abraham and E. Sparrow, Simulation of Fluid Flow Through a Trauma Fluid-Warming Device, Laboratory for Heat Transfer and Fluid Flow Practice, Report AZ-1, December, 2006.
[3.25] D. Liepsch and S. Moravec, Pulsatile flow of non-Newtonian fluids in distensible models of human arteries, Biorheology, 20 (1983) 745-754.
[3.26] A. Fronek, M. Coel, and E. Bernstein, Quantitative ultrasonographic studies of lower extremity flow velocities in health and disease, Circulation, 53 (1976) 957-960.
[3.27] B. Hutchinson and G. Raithby, A multigrid method based on the additive correction strategy. Num. Heat Transfer B, 9 (1986) 511-537.
[3.28] C. Rhie and W. Chow, A numerical study of the turbulent flow past an isolated airfoil with trailing edge separation, AIAA Paper no. 82-0998 (1982).
[3.29] S. Majumdar, Role of underrelaxation in momentum interpolation for calculation of flow with nonstaggered grids, Num. Heat Transfer B, 13 (1988) 125-132.
[3.30] T. Barth and D. Jesperson, The design and applications of upwind schemes on unstructured meshes. AIAA Paper no. 89-0366 (1989).

[4.1] G. Calcagnini et al, In vitro investigation of pacemaker lead heating induced by magnetic resonance imaging: role of implant geometry, Journal of Magnetic Resonance Imaging, 28 (2008) 879-886.
[4.2] S. A. Mohsin, N. M. Sheikh, U. Saeed, MRI induced heating of deep brain stimulation leads: effect of the air-tissue interface, Progress in Electromagnetics Research, 83 (2008) 81-91.
[4.3] S. Park, R. Kamondetdacha, J. Nyenhuis, Calculation of MRI-induced heating of an implanted medical lead wire with an electric field transfer function, Journal of Magnetic Resonance Imaging, 26 (2007) 1278-1285.
[4.4] K. Yassi et al, Evaluation of the risk of overheating and displacement of orthodontic devices in magnetic resonance imaging, Journal of Radiology, 88 (2007) 263-268.
[4.5] H. Bassen et al, MRI-induced heating of selected thin wire metallic implants – laboratory and computational studies – findings and new questions raised, Minimally Invasive Therapy and Allied Technologies, 15 (2006) 76-84.
[4.6] E. Mattei et al, MRI induced heating of pacemaker leads: effect of temperature probe positioning and pacemaker placement on lead tip heating and local SAR, Annual International Conference of the IEEE Engineering in Medicine and Biology Society, 1 (2006) 1889-1892.
[4.7] J. Nyenhuis et al, MRI and implanted medical devices: basic interactions with an emphasis on heating, IEEE Transactions on Device and Materials Reliability, 5 (2005) 467-479.
[4.8] U. Nguyen et al, Numerical evaluation of heating of the human head due to magnetic resonance imaging, IEEE Transactions on Biomedical Engineering, 51 (2004) 1301-1309.
[4.9] W. Nitz et al, On the heating of linear conductive structures as guide wires and catheters in interventional MRI, Journal of Magnetic Resonance Imaging, 13 (2001) 105-114.
[4.10] M. Dempsey, B. Condon, D. Hadley, Investigation of the factors responsible for burns during MRI, Journal of Magnetic Resonance Imaging, 13 (2001) 627-631.
[4.11] F. Shellock, Radiofrequency energy-induced heating during MR procedures: a review, Journal of Magnetic Resonance Imaging, 12 (2000) 30-36.
[4.12] J. Nyenhuis et al, Heating near implanted medical devices by the MRI RF-magnetic field, Digests of the Intermag Conference, (1999) BQ-12.
[4.13] O. Anfinsen et al, Implantable cardioverter defibrillator dysfunction during and after magnetic resonance imaging, Pacing and Clinical Electrophysiology, 25 (2002) 1400-1402.
[4.14] S. Pinski, R. Trohman, Interference in implanted cardiac devices, part II, Pacing and Clinical Electrophysiology, 25 (2002) 1496-1509.
[4.15] M. Niehus, J. Tebbenjohanns, Electromagnetic interference in patients with implanted pacemakers or cardioverter-defibrillators, Heart, 86 (2001) 246-248.
[4.16] S. Achenbach et al, Effects of MRI on cardiac pacemakers and electrodes, American Heart Journal, 134 (1997) 467-473.
[4.17] J. Weinmann, E. Sparrow, Heat flow from neuromodulation systems into surrounding media, Neuromodulation, 12 (2009).
[4.18] January 25, 2008. Meeting with Dr. Marie Clair Buckley

[4.19] S. Jiang et al, Effects of thermal properties and geometrical dimensions on skin burn injuries, Burns, 28 (2002) 713-717.
[4.20] M. Cohen, Measurement of the thermal properties of human skin. a review, Journal of Investigative Dermatology, 69 (1977) 333-338.
[4.21] F. Duck, Physical Properties of Tissue, A Comprehensive Reference Book, London: Academic Press, 1990.
[4.22] J. Valvano, J. Allen, H. Bowman, The simultaneous measurement of thermal conductivity, thermal diffusivity, and perfusion in small volumes of tissue, ASME 81-WA/HT-21, 1981.
[4.23] J. Johnson et al, Regulation of the cutaneous circulation, Federation Proceedings, 45 (1986) 2841-2850.
[4.24] T. Kobayashi et al, Improvement of deep body thermometer for man, Annals of Biomedical Engineering, 3 (1975) 181-188.
[4.25] D. Brajkovic, M. Ducharme, Confounding factors in the use of the zero-heat-flow method for non-invasive muscle temperature measurement, European Journal of Applied Physiology, 94 (2005) 386-391.
[4.26] R. Fox, A. Solman, A new technique for monitoring the deep body temperature in man from the intact skin surface, Journal of Physiology, 212 (1971) 8P-10P.
[4.27] R. Fox et al, A new method for monitoring deep body temperatures from the skin surface, Clinical Science, 44 (1973) 81-86.
[4.28] H. Pennes, Analysis of tissue and arterial blood temperatures in the resting human forearm, Journal of Applied Physiology, 85 (1948) 5-34.
[4.29] F. Henriques, A. Moritz. Studies of thermal injury I: the conduction of heat to and through the skin and the temperatures attained therein. A theoretical and experimental investigation, American Journal of Pathology, 23 (1947) 531-549.
[4.30] J. Weaver, A. Stoll, Mathematical model of skin exposed to thermal radiation, Aerospace Medicine, (1969) 24-30.
[5.1] J. Gimbel, J. Zarghami, C. Marchado, B. Wilkoff, Safe scanning, but frequent artifacts mimicking bradycardia and tachycardia during Magnetic Resonance Imaging (MRI) in patients with an Implantable Loop Recorder (ILR), Ann. Noninvasive Electrocardiology, 10 (2005) 404-408.
[5.2] F. Shellock, R. Crivelli, R. Venugopalan, Programmable infusion pump and catheter: Evaluation using 3-Tesla magnetic resonance imaging, Neuromodulation, 11 (2008) 163-170.
[5.3] M. Muhlenweg, G. Schaefers, S. Trattnig, Safety aspects in high-field magnetic resonance imaging, Radiologe, 48 (2008) 258-267.
[5.4] S. Pisa, G. Calcagnini, M. Cavagnaro, E. Piuzzi, E. Mattei, P. Bernardi, A study of the interaction between implanted pacemakers and the radio-frequency field produced by magnetic resonance imaging apparatus, IEEE Trans. Electromagnetic Compatibility, 50 (2008) 35-42.
[5.5] F. Shellock, L. Fischer, D. Fieno, Cardiac pacemakers and implantable cardioverter defibrillator: In vitro magnetic resonance imaging evaluation at 1.5-Tesla, J. Cardiovascular Magnetic Resonance, 9 (2007) 21-31.
[5.6] J. Weinmann and E. Sparrow, Heat flow from neuromodulation systems into surrounding media, Neuromodulation, 12 (2009) 114-121.

[5.7] R. Lovik, J. Abraham, E. Sparrow, Potential tissue damage from transcutaneous recharge of neuromodulation implants, Int. J. Heat Mass Transfer, 52 (2009) 3518-3524.
[5.8] J. Abraham, R. Lovik, E. Sparrow, Tissue temperature rises due to heat generation in neuromodulation implants, North American Neuromodulation Society 12th Annual Meeting, Las Vegas, NV, December 4-7, 2008.
[5.9] J. Abraham, E. Sparrow, R. Lovik, An investigation of tissue-temperature elevation caused by recharging of transcutaneous nueromodulation devices, 31st Annual International Conference of the IEEE Engineering in Medicine in Biology Society, Minneapolis, MN, September 2-7, 2009.
[5.10] J. Abraham, R. Lovik, D. Smith, E. Sparrow, K. Kelly, Heat generation measurements of revised neuromodeulation devices and calculations of tissue temperatures, North American Neuromodulation Society 13th Annual Meeting, Las Vegas, NV, December 4-6, 2009.
[5.11] S. Jiang, N. Ma, H. Li, X. Zhang, Effects of thermal properties and geometrical dimensions on skin burn injuries, Burns, 28 (2002) 713-717.
[5.12] M. Cohen, Measurement of the thermal properties of human skin. A review, J. Investigative Dermatology, 69 (1977) 333-338.
[5.13] F. Duck, Physical Properties of Tissue, A Comprehensive Reference Book, London: Academic Press, 1990.
[5.14] J. Valvano, J. Allen, H. Bowman, The simultaneous measurement of thermal conductivity, thermal diffusivity, and perfusion in small volumes of tissue, ASME 81-WA/HT-21, 1981.
[5.15] J. Johnson, G. Brengelmann, J. Hales, P. Vanhoutte, C. Wenger, Regulation of the cutaneous circulation, Federation Proceedings, 45 (1986) 2841-2850.
[5.16] T. Kobayash, T. Nemoto, A. Kamiya, T. Togawa, Improvement of deep body thermometer for man, Annals of Biomedical Engineering, 3 (1975) 181-188.
[5.17] D. Brajkovic and M. Ducharme, Confounding factors in the use of the zero-heat-flow method for non-invasive muscle temperature measurement, Euro. J. Applied Physiology, 94 (2005) 386-391.
[5.18] R. Fox A. Solman, A new technique for monitoring the deep body temperature in man from the intact skin surface, J. Physiology, 212 (1971) 8P-10P.
[5.19] R. Fox, A. Solomon, R. Isaacs, A. Fry, I. MacDonald, A new method for monitoring deep body temperatures from the skin surface, Clinical Science, 44 (1973) 81-86.
[5.20] Advances in Numerical Heat Transfer Vol. 3: Numerical Implementation of Bioheat Models and Equations, New York: Taylor and Francis, 2009.
[5.21] Handbook of Numerical Heat Transfer, 2nd Ed. Editors: Sparrow, Minkowycz, and Murthy, New York: John-Wiley & Sons, Inc., 2006.
[5.22] H. Pennes, Analysis of tissue and arterial blood temperatures in the resting human forearm, J. Applied Physiology, 85 (1948) 5-34.
[5.23] Active Implantable Medical Devices, BS EN 45501-1: 1998.
[5.24] Medical Electrical Equipment, BS EN 60601-1:2006
[6.1] D. Smith, R. Lovik, E. Sparrow, J. Abraham, Human tissue temperatures achieved during recharging of new-generation neuromodulation devices, Int J Heat and Mass Transfer, 53 (2010) 3292-3299.

[6.2] H. Pennes, Analysis of tissue and arterial blood temperatures in the resting human forearm, J Appl Physiol, 85 (1948) 5-34.
[6.3] S. Jiang, N. Ma, H. Li, X. Zhang, Effects of thermal properties and geometrical dimensions on skin burn injuries, Burns, 28 (2002) 713-717.
[6.4] M. Cohen, Measurement of the thermal properties of human skin. A review, J Investigative Dermatology, 69 (1977) 333-338.
[6.5] F. Duck, Physical Properties of Tissue, A Comprehensive Reference Book. London: Academic Press, 1990.
[6.6] J. Valvano, J. Allen, H. Bowman, The simultaneous measurement of thermal conductivity, thermal diffusivity, and perfusion in small volumes of tissue, ASME 81-WA/HT-21, 1981.
[6.7] J. Johnson, G. Brengelmann, J. Hales, P. Vanhoutte, C. Wenger, Regulation of the cutaneous circulation, Federation Proceedings, 45 (1986) 2841-2850.
[6.8] T. Kobayash, T. Nemoto, A. Kamiya, T. Togawa, Improvement of deep body thermometer for man, Annals of Biomedical Engineering, 3 (1975) 181-188.
[6.9] D. Brajkovic, M. Ducharme, Confounding factors in the use of the zero-heat-flow method for non-invasive muscle temperature measurement, Euro J Applied Physiology, 94 (2005) 386-391.
[6.10] R. Fox, A. Solman, A new technique for monitoring the deep body temperature in man from the intact skin surface, J Physiology, 212 (1971) 8-10.
[6.11] R. Fox, A. Solomon, R. Isaacs, A. Fry, C. MacDonald, A new method for monitoring deep body temperatures from the skin surface, Clinical Science, 44 (1973) 81-86.
[6.12] M. Dewhirst, B. Viglianti, M. Lora-Michiels, M. Hanson, P. Hoopes, Basic principles of thermal dosimetry and thermal thresholds for tissue damage from hyperthermia, Int J Hyperthermia, 19 (2003) 267-294.
[6.13] Y. Feng, J. Oden, M. Rylander, A two-state cell damage model under hyperthermic conditions: theory and in vitro experiment, J Biomechanical Engineering, 130 (2008) paper 041016.
[6.14] W. Dewey, L. Hopwood, S. Sapareto, L. Gerweck, Cellular responses to combinations of hyperthermia and radiation, Radiology, 123 (1977) 463-474.
[6.15] M. Rylander, K. Diller, S. Wang, S. Aggarwal, Correlation of HSP70 expression and cell viability following thermal stimulation of bovine aortic endothelial cells, J Biomechanical Engineering, 127 (2005) 751-757.
[6.16] P. Hariharan, I. Chang, M. Myers, R. Banerjee, Radio-frequency ablation in a realistic reconstructed hepatic tissue, J Biomechanical Engineering, 129 (2007) 354-364.
[6.17] J. Lepock, Cellular effects of hyperthermia: relevance to the minimum dose for thermal damage, Int J Hyperthermia, 19 2003 252-266.
[6.18] R. Chopra, M. Bertnyk, M. Haider, M. Bronskill, Method for MRI-guided conformal thermal therapy of prostate with planar transurethral ultrasound heating applicators, Phys Med Biol, 50 (2005) 4957-4975.
[6.19] P. Bhowmick, J. Coad, S. Bhowmick, J. Pryor, T. Larson, J. Rosette, J. Bischof, In vitro assessment of the efficacy of thermal therapy in human benign prostatic hyperplasia, Int J Hyperthermia, 4 (2004) 421-439.

[6.20] X. Chen, G. Saidel, Mathematical modeling of thermal ablation in tissue surrounding a large vessel, J Biomechanical Engineering, 131 (2009) paper 011001.
[6.21] F. Henriques, A. Moritz, Studies of thermal injury I: the conduction of heat to and through the skin and the temperatures attained therein. A theoretical and experimental investigation, American J Pathology, 23 (1947) 531-549.
[6.22] J. Weaver, A. Stoll, Mathematical Model of Skin Exposed to Thermal Radiation. Aerospace Medicine, (1969) 24-30.